Innovative fabrication, characterisation and real-world lifetime study of organic photovoltaic devices

Yiwei Zhang

Department of Physics and Astronomy

The University of Sheffield

Thesis submitted for the degree of
Doctor of Philosophy

December 2016

Innovative fabrication, characterisation and real-world lifetime study of organic photovoltaic devices

Yiwei Zhang

Department of Physics and Astronomy

The University of Sheffield

Thesis submitted for the degree of
Doctor of Philosophy

December 2016

Acknowledgements

Time flies by. My three years PhD career has come to the final stage. I feel really luck to stand here. Before finishing the thesis, I would like to express my gratitude to all who were with me on the road to where I am now.

Firstly, I would like to say a big thank you to my supervisor Prof. David G. Lidzey. Without his support, I could not have the chance to Sheffield to pursue the PhD degree. Throughout the 3 years research and life in Sheffield, I was convinced many times by his knowledge on the research work. He also always supports my ideas, allows me to try and realize my ideas. He made great effort to all my published papers and this thesis. Whist I also learnt a lot from his attitudes towards life as a good researcher. I could not expect a better supervisor. Thank you David!

Secondly, I would like to thank Prof. Tao Wang, I was so lucky to work with him in the lab, especially when I just arrived in a new country; he also gave me the initial training to most of the equipments in the lab. For me he is like a senior brother and best friend. I will remember the time we worked together.

I would also like to say thank you to Dr. Andy Parnell and Dr. Gabriel Bernardo. Our work in ISIS is interesting and fruitful. I did not expect to have the chance to play with neutrons, but it is really nice to work with you. Talking with you also helps me to understand better what a researcher should do.

To all my EPMM group mates and the staff from Ossila, both past and present; their altruistic help made my research much easier; they also made the life in Sheffield more memorable. A special shout to Kyriacos, sharing an apartment with you for months is fantastic experience.

Also thanks to members in Ahmed Iraqi's group in Chemistry department for their support

in various characterization methods on polymers. It is my honour to work with you, hope in the future we can work together again.

Finally but by no means least, I would like to thank my family, without their support and encouragement, I could not be where I am now.

Publications

1. Zhang, Y., Griffin, J., Scarratt, N.W., Wang, T. & Lidzey, D.G. High efficiency arrays of polymer solar cells fabricated by spray-coating in air. *Progress in Photovoltaics: Research and Applications* **24**, 275-282 (2016).
2. Zhang, Y. et al. PCDTBT based solar cells: one year of operation under real-world conditions. *Scientific Reports* **6**, 21632 (2016).
3. Zhang, Y., Scarratt, N.W., Wang, T. & Lidzey, D.G. Fabricating high performance conventional and inverted polymer solar cells by spray coating in air. *Vacuum* **139**,154.
4. Zhang, Y. et al. Understanding and controlling morphology evolution via DIO plasticization in PffBT4T-2OD/PC71BM devices. *Scientific Reports* **7**, 44269 (2017).
5. Alqurashy, B.A., Iraqi, A., Zhang, Y. & Lidzey, D.G. Preparation and photovoltaic properties of pyrene-thieno[3,4-c]pyrrole-4,6-dione-based donor-acceptor polymers. *European Polymer Journal* **85**, 225-235 (2016).
6. Wang, T., Zhang, Y., Yan, Y., Jones, C.G. & Lidzey, D.G. Polymer Light Emitting Diodes Powered via Paper-Mounted Electronics. *Journal of Display Technology* **12**, 583-588 (2016).
7. Masters, R.C. et al. Novel organic photovoltaic polymer blends: A rapid, 3-dimensional morphology analysis using backscattered electron imaging in the scanning electron microscope. *Solar Energy Materials and Solar Cells* **160**, 182-192 (2017).
8. Scarratt, N.W. et al. Polymer-based solar cells having an active area of 1.6 cm2 fabricated via spray coating. *APL Mater.* **3**, 126108 (2015).
9. Yan, Y. et al. Light-Soaking-Free Inverted Polymer Solar Cells with an Efficiency of 10.5% by Compositional and Surface Modifications to a Low-Temperature-Processed

TiO2 Electron-Transport Layer. *Advanced Materials*, accepted.

10. Alqurashy, B.A., Cartwright, L., Iraqi, A., Zhang, Y. & Lidzey, D.G. Pyrene–benzothiadiazole-based copolymers for application in photovoltaic devices. *Polymers for Advanced Technologies*, accepted.

11. Cartwright, L. et al. Triisopropylsilylacetylene-functionalised anthracene-alt-benzothiadiazole copolymers for application in bulk heterojunction solar cells. *RSC Advances* **5**, 101607-101615 (2015).

12. Wang, T. et al. Vertical stratification and its impact on device performance in a polycarbazole based copolymer solar cells. *Journal of Materials Chemistry C* **3**, 4007-4015 (2015).

13. Cartwright, L., Iraqi, A., Zhang, Y., Wang, T. & Lidzey, D.G. Impact of fluorine substitution upon the photovoltaic properties of benzothiadiazole-fluorene alternate copolymers. *RSC Advances* **5**, 46386-46394 (2015).

14. Zhang, Y. et al. Comparative indoor and outdoor stability measurements of polymer based solar cells. *Scientific Reports* Accepted.

Conference presentations

1. 12th Photovoltaic Science, Application and Technology Conference, Liverpool, UK 2016.03

2. UK Semiconductor 2015, Sheffield, UK 2015.07

Abstract

To commercialize organic photovoltaics, some challenges still need to overcome, mainly including developing cost-effective scalable fabrication techniques, investigating strategies to improve device efficiency, increasing lifetime.

In the thesis, three issues are investigated. First, the fabrication of organic solar cells via spray coating in air has been presented. High efficiency organic solar cell arrays based on PBDTTT-EFT: $PC_{71}BM$ were fabricated over large area substrate (5 cm × 5 cm) by spray coating in air. An efficiency of 8.06% was demonstrated in devices with both PEDOT:PSS hole transport layer and PBDTTT-EFT:$PC_{71}BM$ active layer spray coated. The spray coating was also used to fabricate zinc oxide electron transport layer and high crystalline polymer: fullerene blends. The devices fabricated with spray coating illustrate comparable efficiency to devices that fabricated by spin coating.

Using neutron techniques (neutron reflectivity and small angle neutron scattering), the effects of solvent additive (DIO) and thermal annealing on morphology within a PffBT4T-2OD:$PC_{71}BM$ bulk heterojunction film have been investigated. It has been found that the DIO act as plasticizer and can coarsen the domains within the bulk heterojunction during thermal annealing. This can significantly improve the device efficiency by 20%.

Finally, PCDTBT:$PC_{71}BM$ based organic solar cells operation was tracked in real-world condition for a period of one year. It is found the pixels near the edge have reduced stability due to the ingress of water and oxygen through the encapsulation edge. Pixels in the centre of a substrate have enhanced stability, with a Ts80 lifetime of up to 6000 hours. This result suggests with proper encapsulation, organic solar cells can hold pretty good stability under real-world conditions.

Contents

Chapter 1 Introduction 1

1.1 Thesis motivation and summary 4

Chapter 2 Theoretical Background 7

2.1 Introduction 7

2.2 Hybridisation of Carbon Bonds 7

2.3 Conjugated Polymers 9

2.4 Device Physics of OPV devices 9

2.4.1 Excitons in Organic Semiconductors 11

2.4.2 Exciton diffusion 15

2.4.3 Exciton dissociation and recombination 16

2.4.4 Architecture of OPV devices 17

2.4.5 Charge transport 20

2.4.6 Charge extraction 22

2.4.7 The characterisation of OPV devices 24

2.5 Scalable Fabrication Techniques of OPV devices 28

2.5.1 Spin coating 29

2.5.2 Spray coating 30

2.5.3 Blade coating 33

2.5.4 Slot die coating 34

2.6 Stability of OPV devices 35

2.6.1 Lifetime testing strategy 36

2.6.2 Stability of active layers 37

2.6.3 Stability of metal electrodes 38

2.6.4 Stability of hole/electron transport layers 39

2.6.5 Encapsulation 40

2.6.6 Degradation behaviour of organic solar cells 42

2.6.7 Indoor lifetime testing 43

2.6.8 Outdoor lifetime testing 44

2.7 Strategies to optimise active layer micro morphology and device performance 46

2.8 Summary 50

Chapter 3 Experimental Methods 52

3.1 Introduction 52

3.2 Device fabrication 52

3.2.1 Substrate cleaning 52

3.2.2 Solution preparation 52

3.2.3 Spin coating of thin films 54

3.2.4 Spray coating of thin films 55

3.2.4 Top electrode deposition 57

3.2.5 Encapsulation 58

3.3 Photovoltaic characterisation 58

3.4 UV-vis absorption 59

3.5 Photoluminescence (PL) spectroscopy 60

3.6 Atomic force microscopy 61

3.7 Spectroscopic Ellipsometry 63

3.8 Small angle neutron scattering 64

3.9 Neutron reflectivity 66

3.10 Outdoor lifetime testing 67

3.11 Summary 70

Chapter 4 Fabrication of PBDTTT-EFT:$PC_{71}BM$ based solar cell arrays via spray coating in air 72

4.1 Introduction 72

4.2 PEDOT:PSS hole transport layer 73

4.3 PBDTTT-EFT:$PC_{71}BM$ active layers 75

4.4 Device performance 77

4.5 Effect of light and air exposure 83

4.6 Conclusion 85

Chapter 5 Fabrication of high efficiency organic solar cells based on a highly crystalline polymer via spray coating 86

5.1 Introduction 86

5.2 Spin and spray coating ZnO 87

5.3 Optimising the PffBT4T-2OD:$PC_{70}BM$ solution deposition process 87

5.4 Device fabrication and characterisation 89

5.5 Conclusion 92

Chapter 6 The effect of DIO solvent additives and thermal annealing on the micro morphology of PffBT4T-2OD:$PC_{71}BM$ BHJ and OPV device performance 94

6.1 Introduction 94

6.2 Sample preparation and device fabrication 95

6.3 UV-vis absorption and photoluminescence spectra 99

6.4 Ellipsometry 100

6.5 Neutron Reflectivity 103

6.6 Small angle neutron scattering 105

6.7 Conclusion 110

Chapter 7 Real world lifetime study of PCDTBT:$PC_{71}BM$ based solar cells for over a year 112

7.1 Introduction 112

7.2 Testing protocols 112

7.3 Stability of “edge pixels” 115

7.4 Central pixels 118

7.5 Weather information over the testing period 121

7.6 Measurement in laboratory 123

7.7 Conclusion 125

Chapter 8 Conclusions and Outlook 126

8.1 Conclusions 126

8.2 Outlook and suggested future work 128

References 130

Chapter 1 Introduction

As the global economy and population keeps growing at a rapid speed, our energy demand keeps increasing. In 2014, the energy consumption of the whole world approached 151 billion MWh. [1,2] This figure is expected to increase by approximately 34% by 2035 due to the continuously rising economy and predicted increases in population. Currently, the majority of the energy used is supplied by fossil fuels, with coal, oil and natural gas accounting for more than 85% of the energy consumption in the whole world. However, as finite natural sources, the fossil fuels cannot be used indefinitely; alternative sustainable energy sources must be developed before the fossil fuels run out. Because increasing attention has been paid to reducing carbon emissions and suppressing the global warming,[3] the development of renewable energy sources is believed to increase in the following decades. Renewable energy, although still forming a small fraction of the overall energy consumption (about 6%), grew rapidly over the past decade. In 2014, renewable energy contributed to more than 40% of the growth in global energy generation. Nuclear energy provided around 10% electricity generation for the whole world; however, since the Chernobyl disaster in 1986 and Fukushima Daiichi disaster in 2011, the concern about the nuclear plants safety increases; thus more nuclear plants are not desirable for general public. In this case, the renewable energy including solar energy, wind power, hydroelectricity, geothermal energy and tidal energy attract considerable interest as potential energy source for future human society.

As renewable energy sources, wind power, hydroelectricity, geothermal energy and tidal energy are not universal available; while solar energy can be used in most of the area on the earth. Although the energy received by the earth is just a very tiny fraction of the total energy emitted by the sun, and considering the reflectivity and absorption of the atmosphere, the power received by the earth surface is approximately 1.7×10^{11} MW, a value much larger than

our demand.[4] In order to utilise solar energy, techniques are needed to convert it to the energy form that we use in daily life. Solar hot water system [5], which converts solar energy to heat, is one application of solar energy. However, electricity is the most commonly used energy form in modern society; as a result, solar thermal electricity [6] and photovoltaic technologies [7] attract a lot of interest as they convert solar energy to electricity.

Solar thermal electricity generation systems concentrate the sun light and generate heat, which is used to drive a heat engine to make electricity. The working fluid that is heated by the concentrated sunlight could be liquid or gas. Different working fluids include water, oil, salts solution, air, nitrogen, helium. Different engine types include steam engines, gas turbines, Stirling engines, etc.[8] While the photovoltaic techniques convert solar energy directly to electricity by photoelectric effect. PV techniques are highly dependent on the sun irradiance which is affected by weather, time of day and seasonal variation. Thus the effective storage methods are needed to provide electricity when the sunlight is limited or unavailable. Unfortunately, currently high capacity and efficient electricity storage techniques are still the bottleneck of PV application. However, the solar thermal power systems do not have the intermittent problem as the storage of thermal energy is much easier, heat can be stored during the clear days and converted into electricity whenever needed. On the other hand, the advantage of photovoltaic techniques over solar thermal electricity generation system is the relatively low cost and it can be installed in small scale such as on the rooftop of each family, while the solar thermal power plants are usually require large amount of land. Meanwhile, the maintenance cost of photovoltaic techniques, including economic and human resources, is lower than solar thermal power plants.[8] However, it is believed that with further development, these two techniques to convert solar energy to electricity can be complementary.

Here only the scenario of photovoltaic is discussed. To make a simple calculation, the total power generated in the UK in 2016 was around 1468 million MWh [9], a typical

commercial available 4 kWh solar panel system can generate around 3.4 MWh power in a year.[10] Assuming 10 million of such solar panels installed, it can provide 2.3% of the energy requirement of the whole country. Although the calculation is basic, it illustrates the potential to utilise solar energy replace some role of the fossil fuels.

Now silicon based solar cells still dominate the commercial photovoltaic market and have power conversion efficiency (PCE) above 25%. [11] Silicon wafer based solar cells, also known as first generation solar cells, have high efficiency, but the fabrication is relatively expensive and energy intensive. This limited the application of PV techniques, especially in some African countries where the irradiation time and level is suitable for solar cells. Second generation solar cells (thin-film solar cells) instead have a photovoltaic active layer having a thickness of a few micrometers. This makes their fabrication much easier. Amorphous silicon, cadmium telluride (CdTe), and copper indium gallium diselenide (CIGS) are the main three photo active materials in this category.[12-14] There are, however, still some concerns regarding second generation solar cells, including high cost, limited efficiency, stability issues and the toxicity of cadmium. Research effort now turns to third generation photovoltaics which are thin film devices compatible with high volume manufacture. [15] The objective of such research is to combine high performance solar cells with high volume manufacture process at low cost. This could result in photovoltaic devices being one of the main sources of electricity generation.

Currently, most third generation solar cells are still undergoing laboratory stage research and are not yet commercially available. Nevertheless some innovative companies have invested in related fields. Generally, a variety of new materials have been used in third generation solar cells, such as carbon nanotubes,[16] organic dyes,[17] nanowires,[18] and recently developed perovskite materials.[19] Among these materials, organic semiconductors are one type of the most important materials have been used in third generation solar cells, and have

the following advantages: [20]

(1). Manufacture on low weight, high flexibility plastic substrates.

(2). Ease of integration with other functional organic semiconductor devices, for instance, organic light emitting diodes (OLEDs) and organic thin film transistors (OTFTs).

(3). New concepts and market opportunities, such as new solar powered vehicles, wearable devices and building integrated organic photovoltaic installations (BIOPV).

The past decade has witnessed a steady growth in the efficiency of organic photovoltaics (OPVs), with power conversion efficiencies (PCEs) currently exceeding 10%; [11,21,22] a value regarded as a significant step in the so-called 10/10 target for organic photovoltaics (10% efficiency and 10 years lifetime). With the continuous effort from chemists, the highest efficiency for traditional single bulk heterojunction OPV devices based on newly developed organic semiconductor materials has reached over 12%.[23] The highest record for multi-junction cells is 13.2%, reported by a company, Heliatek. Although the performance is promising and can be considered for commercialization, there are still some challenges to overcome. From a practical perspective, innovative, cost effective fabrication techniques that are compatible with high volume solution based manufacture are still needed to develop. Furthermore, the efficiency of OPVs is still not competitive with silicon based solar cells and need to be improved further. New methods are also necessary to increase the lifetime of OPV devices. From a theoretical perspective, the understanding of the degradation mechanism and the morphology-performance relationships are still limited.

1.1 Thesis motivation and summary

The first main target of this thesis is to explore innovative processes for high-efficiency and high-volume OPV manufacture. A second theme of the work is to study the long-term

outdoor stability and the morphology-performance relationships in OPV devices. The structure and content of this thesis is as follows:

Chapter 2 presents a basic theoretical overview of organic semiconductor physics and its application in organic solar cells. A brief literature review of this research field is also provided.

Chapter 3 describes the experimental methods employed.

In Chapter 4, we discuss spray coating in air of organic photovoltaic devices based on a low band gap polymer, namely PBDTTT-EFT. This was used to create an array of 36 OPV pixels over an area of 5 cm x 5 cm having high efficiency and good uniformity. Processes that limited device efficiency were investigated and it was found that the combination of air and light was one of the key factors causing the degradation of spray-cast PBDTTT-EFT based OPV devices. The results indicate that spray coating is a promising thin film fabrication technique which can be used to fabricate high efficiency organic solar cell devices on large area substrates under well-controlled illumination conditions.

In Chapter 5, we also discuss the fabrication of organic solar cell devices based on a highly crystalline polymer PffBT4T-2OD via spray coating in air. In this work, a PEDOT:PSS hole transport layer and a zinc oxide (ZnO) electron transport layer were spray coated in air. In the device architectures explored, the PffBT4T-2OD:$PC_{71}BM$ photoactive layer was also spray coated in air. Critically, the photoactive ink was prepared at low concentration, in cold solution, but avoided obvious problems resulting from aggregation of this highly crystalline polymer material. This work further illustrates the feasibility of manufacturing high performance OPVs by spray coating in air.

In Chapter 6, it is shown that thermal annealing of PffBT4T-2OD:$PC_{71}BM$ bulk heterojunction (BHJ) films containing 3% of a DIO solvent additive at 100 ºC for 3 minutes

can improve the power conversion efficiency (PCE) of the solar cells based on this polymer: fullerene system by more than 20%, from 7.20% to above 8.70%. This effect was investigated using small angle neutron scattering (SANS) and neutron reflectivity (NR). The results demonstrate that the nano-morphology of the BHJs gradually coarsen during annealing with the presence of DIO. Further measurement using ellipsometry suggests thermal annealing processes likely removes any trapped DIO within the first 3 minutes, which leads to improved device performance. The results provide a better understand of the morphology-performance relationship in this particular type of OPV device.

Chapter 7 presents prolonged outdoor lifetime testing of PCDTBT:$PC_{71}BM$ based organic solar cells. The testing was performed continuously for a year in Sheffield, England. It is found that under real-world operational conditions, the devices underwent an initial burn-in degradation which ended after 450 hours followed by a Ts80 lifetime of up to 6200 hours. It is concluded that in PCDTBT:$PC_{71}BM$ based organic solar cells, the dominant degradation mechanism is the thermally-induced stress or break-down of the encapsulation cause by wide fluctuations in temperature that occur over the summer months. Our work further confirms that PCDTBT is a highly stable conjugated polymer, and that improved device lifetime can be expected through improvements in encapsulation techniques.

Finally, in Chapter 8, a summary and conclusion are presented along with suggestion for future work.

Chapter 2 Theoretical Background

2.1 Introduction

In this chapter, the physics of organic photovoltaic (OPV) devices is described. In Section 2.2 and 2.3, general concepts of organic semiconductors are introduced. Then in section 2.4, the device physics of OPV devices are presented in detail. Following this, various scalable OPV devices fabrication techniques are reviewed in section 2.5. This is followed by a discussion of stability of OPV devices in section 2.6. We finally discuss the influence of the BHJ nano-morphology on device performance in Figure 2.7.

2.2 Hybridisation of Carbon Bonds

In a carbon atom, there are 6 electrons which form the following ground state structure: $1s^2 2s^2 2p_x^1 2p_y^1$. In carbon based molecules, atoms are bound together through covalent bonds. [24] In a typical covalent bond, different atoms complete the electronic shell according to the octet rule by sharing electrons. However, in carbon atoms, the formation of a covalent bond is more complicated because of the presence of hybridisation. In a carbon atom, the inner electron shell is filled and can be ignored when discussing bond formation and hybridisation. On hybridisation of the outer shell, one electron from 2s is usually promoted to the p_z orbital which is empty, which results an electronic configuration of $1s^2 2s^1 2p_x^1 2p_y^1 2p_z^1$.[25] The remaining 2s electron can then hybridise with one, two or all the three 2p electrons to form hybridised sp, sp^2 or sp^3 orbitals.

As shown in Table 2.1, sp hybrid orbitals have two lobes along one axis, positioned at an angle of 180° to each other, along with two remaining 2p orbitals. In this situation carbon needs to form a bond with another sp hybrid carbon atom to create a stable molecule. To do this, one of the two lobes overlaps with another carbon sp hybrid orbital to form a σ bond. The remaining two 2p orbitals of each atom overlap to form two π bonds. This creates a so-called carbon triple bond, consisting of one σ bond and two π bonds. The other free sp orbitals can then form bonds with different atoms to create a stable molecule.

Carbon atoms forming sp^2 hybrid orbitals consist of 3 lobes in the same plane having an isotropic distribution with one 2p orbital which is positioned perpendicular to the plane. One of the 3 hybrid orbitals can overlap with sp^2 orbitals from another sp^2 hybrid carbon to create an σ bond with the remaining p orbital from each atom overlapping to form a π bond. Here the σ bond and the π bond constitute a carbon double bond.

In a sp^3 hybrid system, there are four lobes that are tetragonally spaced. Here the angle between each two lobes is 109°28'. In this situation, carbon can form four σ bonds by sharing electrons with atoms or other sp^3 orbitals.

As an σ bond is much stronger than a π bond; π bonds tend to be more delocalised than σ bonds. This feature will be discussed later.

Hybridisation type	Number of hybrid orbitals	Geometry
sp	2	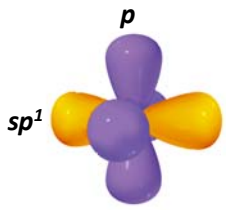
sp^2	3	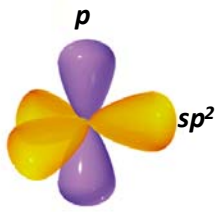
sp^3	4	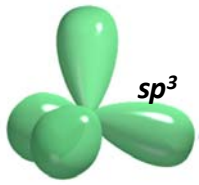

Table 2.1 The Carbon hybrid orbitals

2.3 Conjugated Polymers

Conjugated molecules are molecules in which there are alternating single and double (triple) carbon bonds. As a result, the π electrons can delocalise throughout the entire molecule. Benzene is a typical example of a conjugated molecule. Here the delocalisation of π electrons gives the molecule its semiconductor properties. To describe the physics of such materials, the concept of molecular orbitals (MO) has been introduced. In this picture, the molecule is treated as a whole, rather than as atoms bonded by various bonds. The molecule is then treated as nuclei having positive charge and electrons with negative charge. To form an electrically neutral molecule, the electrons need to fill the various molecular orbitals. The state with lowest energy is the actual state in which the molecule is found. We can then define the molecular orbital in which the last electron pair occupies the highest occupied molecular orbital (HOMO). With the HOMO filled, the molecule is then electrically neutral and complete. However, if one more electron is added to the molecule, the molecular orbital it occupies is defined as lowest unoccupied molecular orbital (LUMO). The concept of HOMO and LUMO are similar to the valence (VB) and conduction band (CB) found in inorganic semiconductors. Although the HOMO and LUMO levels do not form bands, the concept of bandgap is still used to refer the energy difference between the HOMO and LUMO level.

2.4 Device Physics of OPV devices

To generate electricity, the energy origin is the sun; this section is started with the introduction of the solar spectrum. The standard spectrum outside the Earth's atmosphere is known as AM0. This spectrum corresponds to sunlight without any absorption or scattering by the atmosphere and it is normally used to evaluate solar cells used in space industry.

The standard spectrum at the surface of the Earth is called AM1.5. Due to absorption and scattering by the atmosphere, the power density of AM1.5 spectrum is lower than that of the AM0 spectrum. The actual power density is approximately 970 W/m^2; however, the standard AM1.5 spectrum is always normalised in practice to 1000W/m^2 for convenience. The standard spectra of AM1.5 and AM0 are presented in Figure 2.1.

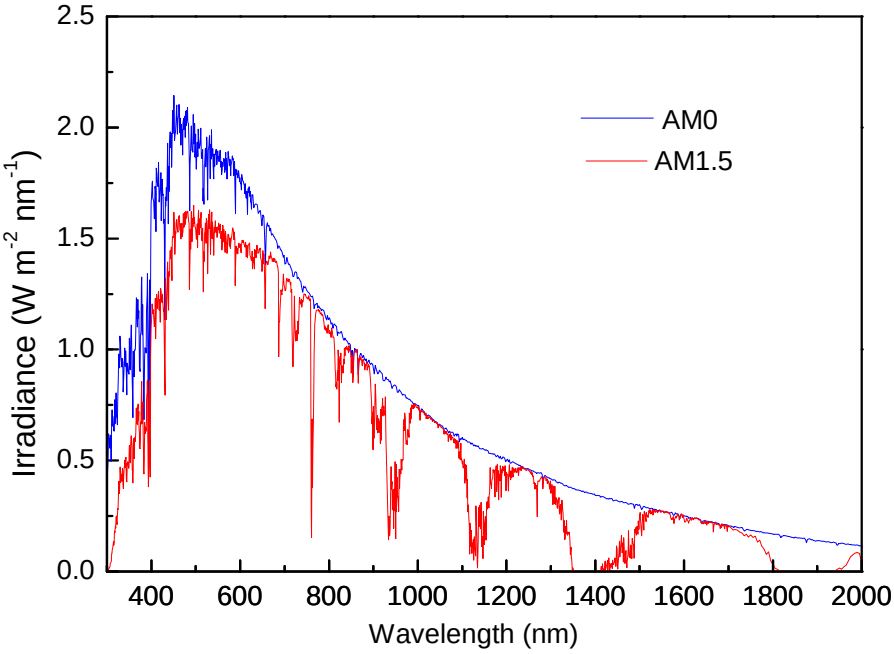

Figure 2.1 Solar spectra of outside the Earth atmosphere (AM0) and at the surface of the Earth (AM1. 5) [26]

In general (include but not limited to OPV), the maximum theoretical power convention efficiency of a single p-n junction solar cell is predicted by Shockley-Queisser Efficiency Limit, [27] which is calculated by examining the amount of electrical energy that is extracted per incident photon. The Shockley-Queisser maximum efficiency of a single junction solar cell is a function of the band gap energy. Under the AM1.5 solar spectrum, the highest Shockley-Queisser Efficiency Limit has been determined to be 33.7% with the optimum band gap to be 1.4 eV.[28] For silicon based solar cells, the favourable band gap is 1.1 eV and the maximum efficiency is determined to be 32%. For the case of OPV, the determination of the efficiency limit is complicated, the literatures presented different values ranging from 12% to 15%.[29,30] Now with the development of non-fullerene acceptor materials, efficiency of 12% has been realised.[23] Koster et al. [31]reported a new pathway to increase the efficiency limit of OPV devices: by increasing the dielectric constant of the absorber material. A larger dielectric constant results in a smaller exciton binding energy, thus a smaller LUMO-LUMO offset is sufficient for exciton dissociation. Their model indicates that by increasing relative dielectric

constant from 3 to 8, the efficiency would increase for 12% to about 20%.

In this section, the device physics of OPV device would be introduced. In an OPV device, the current generation process starts from the generation of an exciton, and then the excitons diffuse to an interface of donor and acceptor materials before recombination, and at the interface the excitons are dissociated into free electrons and holes. The electrons and holes then transport through hopping to the electrodes where the charge carriers are extracted and collected. In this part, these processes will be discussed.

2.4.1 Exciton in Organic Semiconductors

By absorbing a photon with energy greater than the energy gap between the HOMO and LUMO levels, an electron can be promoted from the HOMO to the LUMO level, leaving a hole in the HOMO level. For convenience, the hole is usually considered as a particle with an equal but opposite charge to that of the electron. Thus the molecule remains in an electrically neutral but excited state, with the excitation called an exciton. Here the electron and hole are bound by the Coulomb force and form an exciton. According to the Born-Oppenheimer approximation, the motion of the atomic nuclei and the outer electrons can be described by electronic and nuclear components because of the different effective mass between nuclei and the electrons.

For electronic transitions, the Franck-Condon principal is used to describe the intensity of each possible transition. Here an electronic transition from one vibrational mode to another is more likely to occur when overlap of wave functions is maximised. As shown in Figure 2.2, the excited singlet state has a number of vibrational modes (n). On absorption of a photon with energy larger than that of the band gap, an electron can be excited to one of the vibrational mode. This higher excited state can then relaxes to the lowest lying excited state (n = 0) through fast non-radiative processes. The energy is released in the form of phonon. The time scale for this non-radiative relaxation process is about 100 fs. Typically, singlet excitons have a lifetime of between 100-1000 ps before recombination occurs through emission of a photon; a process called fluorescence.[32]

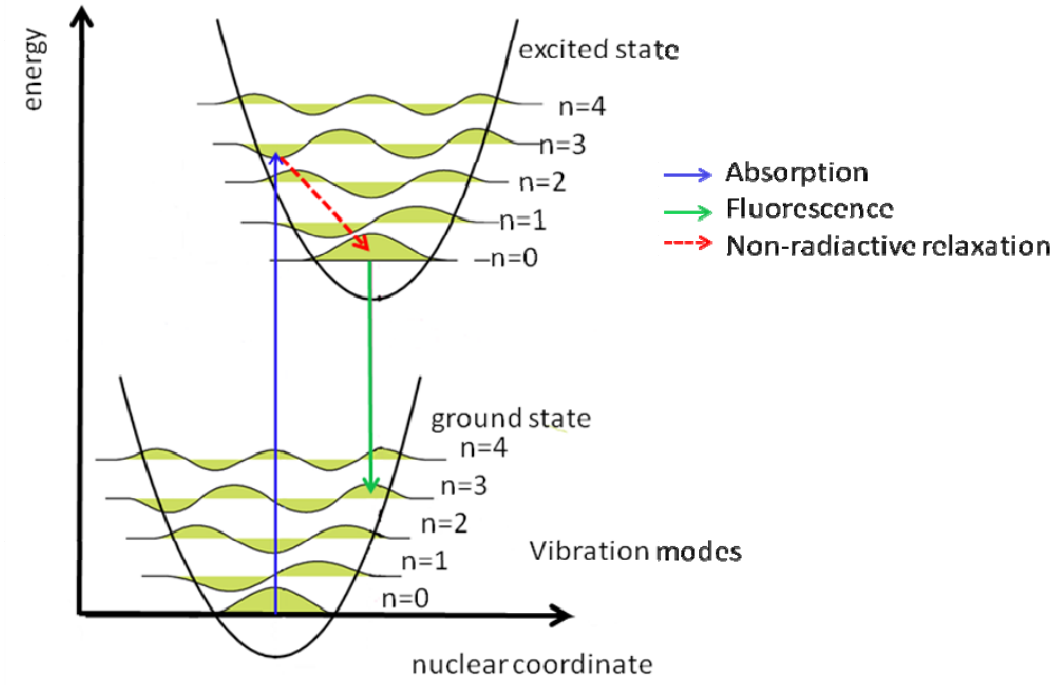

Figure 2.2 Energy level diagrams of the ground and first excited state of a harmonic oscillator.

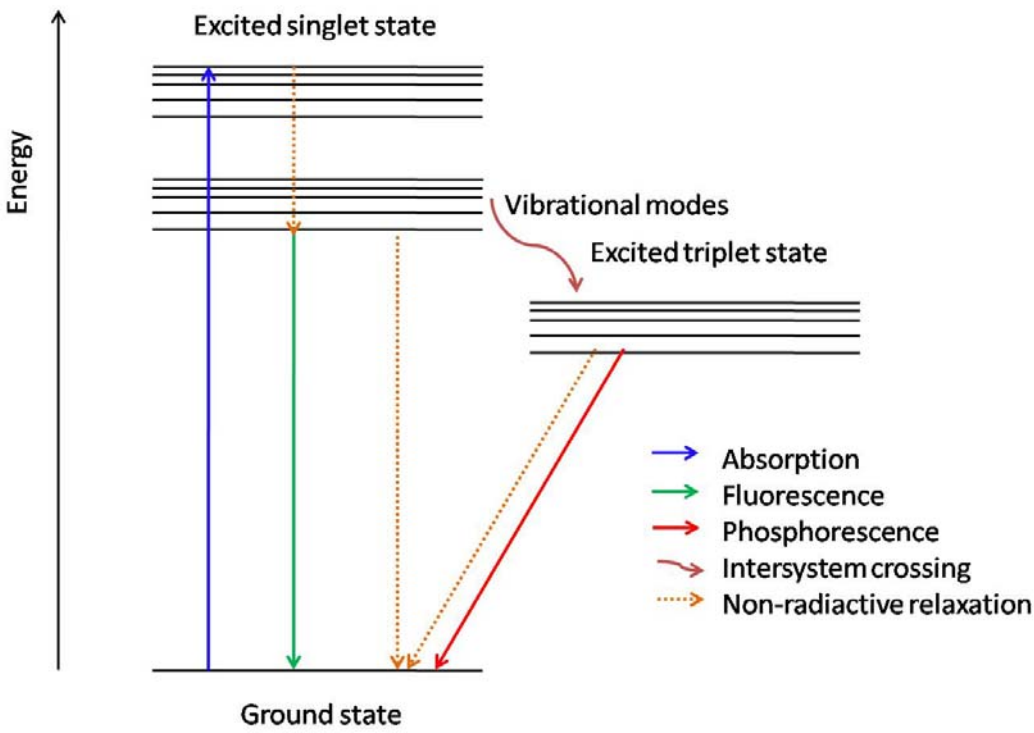

Figure 2.3 Diagram of the radiative and non-radiative processes from an excited state to the ground state.

To summarise the processes discussed in this section, a Jablonski diagram is shown in Figure 2.3. In the Jablonski diagram, the horizontal axis corresponds to states of different spin. It can be seen, the absorption and emission of a photon occurs only between ground states and singlet exited states, which can be interpreted by the so-called dipole selection rules.

In order to describe excited singlet and triplet states, we need to use quantum mechanics. Figure 2.4 shows the two different types of exciton: singlet and triplet. The different types of excitons originate from the fact that electrons and holes possess spin angular momentum of +1/2 or -1/2.

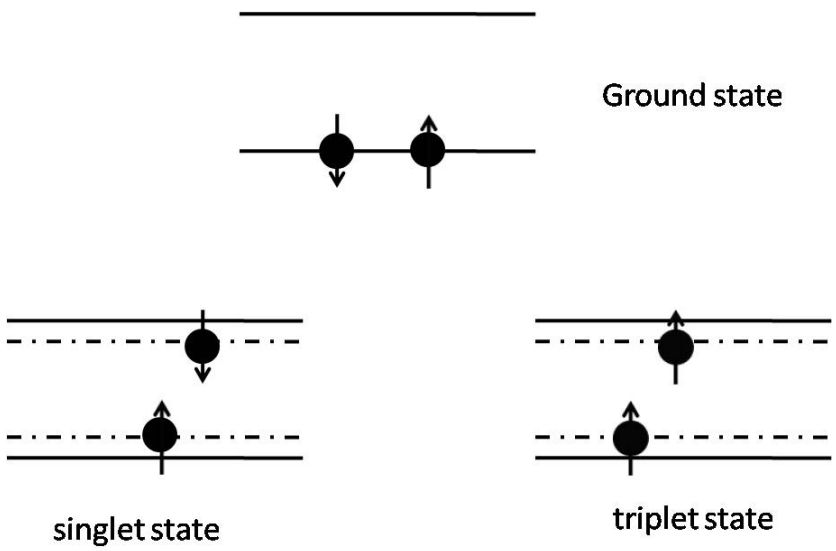

Figure 2.4 Diagram of the electronic ground state as well as excited singlet and triplet states.

The overall wave-function of an exciton can be written as the direct product of a spatial and spin wave-functions. The spin wave-function is a combination of the electron and the hole spins. As shown in Table 2.2, for a total spin S=1, there are three ways in which electron and hole spins can be combined and thus this kind of exciton is termed a triplet exciton. There is however only one way in which the electron and hole spins can be combined giving a total spin of S=0, and this state is known as a singlet state.

It can be seen that the spin wave-function of a triplet exciton is symmetric under particle exchange; however a singlet exciton is antisymmetric. In a Fermionic system (appropriate for electrons and holes), the overall wave function has to be antisymmetric as a result of the Pauli Exclusion Principle. For this reason, the triplet exciton requires an antisymmetric spatial wave

function, while the singlet exciton spatial wave function is symmetric.

According to the dipole selection rules, if a transition from ground state to an exciton state is allowed, the change in spatial angular momentum must be +1 or -1. For absorption and fluorescence, the photon absorbed or emitted can provide the necessary angular momentum to realise the transition. However for the transition from the triplet exciton to the ground state, the change of spatial angular momentum is zero, and thus this transition is forbidden.[33]

Spin wave function	S	S_z	Exciton type
$\lvert\uparrow\uparrow\rangle$	1	1	Triplet
$\lvert\downarrow\downarrow\rangle$	1	-1	Triplet
$\frac{1}{\sqrt{2}}(\lvert\uparrow\downarrow\rangle+\lvert\downarrow\uparrow\rangle)$	1	0	Triplet
$\frac{1}{\sqrt{2}}(\lvert\uparrow\downarrow\rangle-\lvert\downarrow\uparrow\rangle)$	0	0	Singlet

Table 2.2 The possible spin combinations of an electron and a hole

However, the transition from the triplet exciton to the ground state can occur when the very weak link between spin and spatial angular momentum is enhanced. This enhancement is usually realised by a magnetic field and the interaction between spin and spatial angular momentum. This process is called spin-orbit coupling. The light emitted in such a process is named phosphorescence. It is a much slower process than fluorescence, and has a timescale of μs to ms.[34] Processes involving triplet excitons are more important in organic light emitting diodes. However, some recent reports have indicated its importance in organic photovoltaic devices.[35-39]

Finally, to finish the discussion about excitons in organic semiconductor and start the next section, the concept of Frenkel excitons is introduced. Simply speaking, Frenkel excitons are localised excitons. There are two main reasons for such localisation: (1) strong coupling

between the exciton and the atomic lattice and (2) the relatively low relative dielectric constant (about 3-4 of most organic materials) [23]. The Coulomb force between electrons in the LUMO and holes in the HOMO results in an exciton binding energy of approximately 0.3 eV. [24] This value is much higher than thermal energy at room temperature (about 0.026 eV at 300K). In contrast, in inorganic materials, thermal energy at room temperature is sufficient to dissociate the excitons to free charge carriers. As a result, the concept of exciton is of limited importance in inorganic materials at room temperature. In organic materials, in order to dissociate excitons into free charges, excitons need to reach an interface where energy offset occurs which is larger than the exciton binding energy.

2.4.2 Exciton diffusion

Before the exciton arrives at an interface to be dissociated, it must undergo diffusion. The diffusion of excitons occurs via hopping from one localised state to another. This can occur both along and between molecular chains. There are two possible mechanisms by which this occurs: Förster resonance energy transfer (FRET) [40] and Dexter energy transfer (DET) [41], as shown in Figure 2.5.

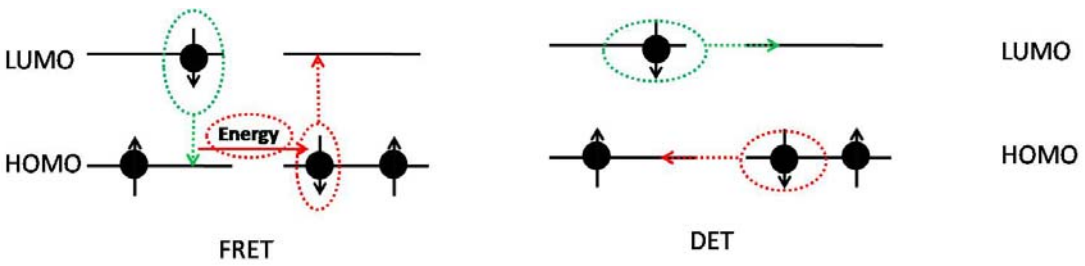

Figure 2.5 Diagram of the two exciton diffusion processes

In FRET, energy is transferred through coupling between neighbour molecules. In this case, the energy transfer efficiency is largely determined by the overlap between the emission spectrum of the donor molecule and the absorption spectrum of the acceptor molecule, as well as the donor-acceptor spatial separation. In the case of DET, energy is transferred via direct transfer of charge carriers. The most important parameter in DET is the extent of wave function overlap between donor and acceptor states.

The typical diffusion length of an exciton is about 10 nm. [42] If an exciton can reach an interface within its lifetime, it is able to undergo dissociation into free charge carriers.

2.4.3 Exciton dissociation and recombination

Once an exciton arrives at the interface which fulfils the energy offset requirement, dissociation can occur. In a typical bulk heterojunction (BHJ) organic photovoltaic device, the interface of the donor-acceptor material provides the thermodynamic driving force for this process. To achieve this, the LUMO level of the acceptor should be lower than that of the donor by an amount larger than the exciton binding energy. However, the acceptor HOMO level must be lower than that of the donor to prevent the hole transferring to the acceptor. If hole transfer occurs, the exciton is not actually dissociated but is transferred to the acceptor. If these requirements are fulfilled, exciton dissociation can occur as shown in Figure 2.6.

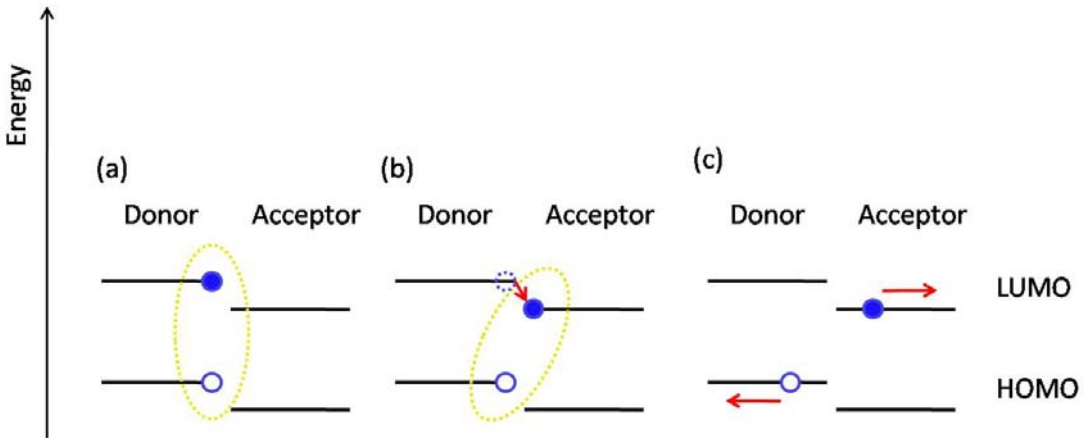

Figure 2.6 Diagram illustrating the dissociation of an exciton at a donor/acceptor interface

The state shown in Figure 2.6(b) is a so-called charge-transfer state. Here the electron and hole are still bound through the Coulomb force but are located on different materials. The electron and hole are only considered to have separated completely when the thermal energy exceeds the Coulomb potential. The critical distance between the electron and hole that satisfies this condition is expressed by the following equation:

$$r_c = \frac{e^2}{4\pi\varepsilon_r\varepsilon_0 k_B T} \tag{2.1}$$

Here, e is the elementary charge, ε_r and ε_0 are the relative and vacuum permittivity respectively and $k_B T$ is the thermal energy of the system.

Recombination of the electron and hole is the most important process that leads to the loss of generated charge carriers. The various recombination mechanisms are shown in Figure 2.7.

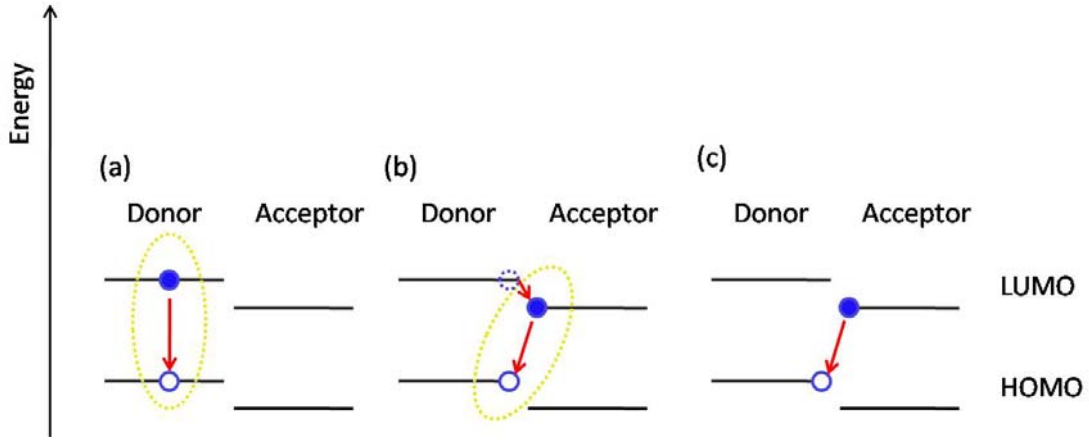

Figure 2.7 Different recombination mechanisms at a donor/acceptor interface: (a) geminate recombination occurs before separation; (b) geminate recombination occurs in charge transfer state; (c) non-geminate recombination

Geminate recombination occurs at two main locations: (a) recombination occurs before the exciton arrives at an interface and (b) recombination happens in the charge transfer state. Non-geminate recombination can also occur. In this process the electron and hole that recombine are generated in different dissociation events, as shown in Figure 2.7(c). Charge carrier recombination is a significant loss mechanism that needs to be minimised in order to achieve high photovoltaic efficiency.

2.4.4 Architecture of OPV devices

Before discussing the charge transport, we describe the two different architectures of OPV devices as in different architecture, the charge carriers transport to opposite directions.

The photovoltaic effect in organic semiconductors was first discovered in multi-layer

structures based on a low work function metal, an organic semiconductor and a high function metal.[43] However, exciton dissociation is limited in such devices and thus the power conversion efficiency was below 1%. A donor-acceptor bi-layer architecture was found to improve the efficiency greatly and was first reported in 1986 by Tang et al. [44] Using this architecture, a device was fabricated having a power conversion efficiency of ~1%.

By introducing a donor-acceptor interface, the dissociation of excitons becomes much easier with the selective transport property of donor/acceptor material helping transport of charge carriers to the electrodes. However, such devices also have drawbacks; as the donor and acceptor layers are deposited sequentially, the extent of the interface between the two materials is quite limited, and thus only excitons generated close to the interface can undergo dissociation. This significantly limits the current density.

To address this issue, a donor-acceptor bulk heterojunction (BHJ) structure was first explored in 1992.[45] By mixing the donor/acceptor materials together, a bicontinuous network of donor and acceptor materials can be obtained. This structure creates a much larger donor/acceptor interface, and makes the dissociation of excitons more efficient. Furthermore such a bicontinuous network can also provide the pathway for charge carriers transportation. However, the domain size of the donor/acceptor material is critical for efficient device performance as effective exciton dissociation requires close mixing between donor and acceptor materials. However, too fine-scale mixing is detrimental for charge transport. Careful control of the nano-morphology within a BHJ therefore is of great importance when fabricating high efficiency devices.

However, BHJ structure is not the ideal structure for OPV devices. For inorganic photovoltaic device, a p-i-n structure is preferred. Similarly, in OPV devices, a structure of Donor/BHJ/Acceptor is expected to helpful to improve the device efficiency. To prove this, Granstrom et al. [46] developed the so-called laminated fabrication technique, which is to spin-coat donor and acceptor materials on separated electrodes, and laminate the two films tightly, then a thermal annealing process is employed to assist inter diffusion of the donor and acceptor layers. The resulted Donor/BHJ/Acceptor structure improves exciton dissociation and charge transport dramatically and an efficiency of 1.9% was achieved. Study on P3HT:

PCBM based layered OPV devices determined comparable efficiency with BHJ devices. [47,48] In P3HT: PCBM layered devices, it is found that[49,50] after depositing PCBM on top of P3HT, inter diffusion of PCBM into P3HT layer occurs spontaneously. Such inter diffusion can be enhanced significantly by thermal annealing and a Donor/BHJ/Acceptor can be achieved. However, due to the relatively complicated fabrication processes, the OPV devices with layered structure are significantly less than that with BHJ structure.

As mentioned in a previous section, BHJ devices can be subdivided in to two types: conventional structure and inverted structure. As shown in Figure 2.8, in a conventional structure, the transparent electrode acts as anode and a high work function hole transport layer (HTL) is inserted between the transparent electrode and the photo active layer to assist the extraction of holes and block electrons. On top of the active layer and below the back metal electrode, a buffer layer also serves as an electron transport layer (ETL) and a hole blocking layer. If however, the position of HTL and ETL are swapped, the electrons and holes are collected at the opposite electrodes, forming an inverted device. In the case of inverted structure, the transparent electrode act as cathode and the top electrode is the anode. In chapter 4-7 involved conventional structure and inverted structure is used in chapter 5.

PEDOT:PSS is the most common HTL due to its good solubility in water and ease to process. [51] Besides, some metallic oxide has also been used as HTL in OPV devices and showed good performance, including molybdenum oxide[52], nickel oxide[53,54], vanadium oxide[55]. Recently, Li et al. [56] used solution processed graphene oxide as the HTL in P3HT:PCBM based OPV devices and a efficiency of 3.5% was determined, which is close to the devices employing PEDOT:PSS HTL.

One of the first ETL used in OPV devices was lithium fluoride[57,58], which has good energy alignment with most of the acceptors. Calcium, as a low work function metal, is also commonly used as ETL in an OPV device.[30,54] However, due to the low work function feature, calcium has the issue of instability against oxygen and moisture. Zinc oxide instead has been used as ETL, good device efficiency and stability has been determined.[59] It is notable that most of the recent reports about high efficiency OPV devices employ the zinc oxide ETL in an inverted structure.[21,60,61] Besides zinc oxide, titanium oxide is also a solution processable ETL material

that is widely used in OPV devices. [62 63]

There are several advantages in the use of inverted structures. These include higher device efficiency and longer lifetime.[64,65] Nevertheless conventional devices are still widely used due to their ease of fabrication.

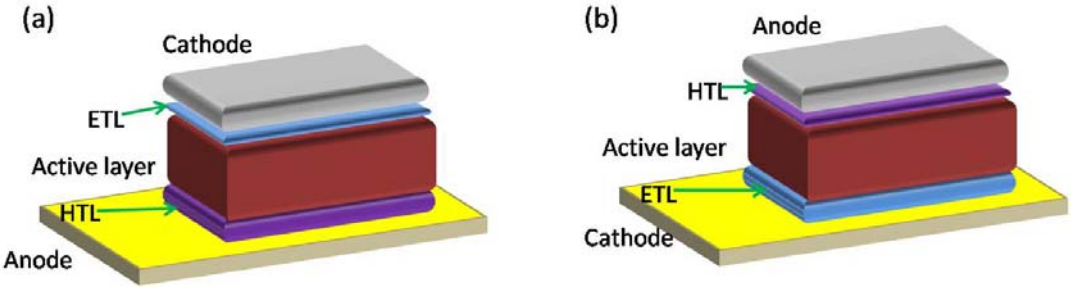

Figure 2.8 Schematic of conventional (a) and inverted (b) OPV devices.

2.4.5 Charge transport

After generating free charge carriers, the transport of charge carriers to the device contact is a necessary process to generate a photo current. As discussed in previous chapter, charge carriers in organic materials are highly localised compared with inorganic semiconductors. As a result the transport in an organic material cannot be described by band theory but instead a thermally assisted hopping process is involved.[66,67] To describe the process analytically, a Gaussian disorder model is employed. The distribution of energy states in a disordered system can be expressed as following: [66]

$$g(E) = \frac{1}{\sqrt{2\pi\sigma}} \exp(-\frac{E^2}{2\sigma^2}) \tag{2.2}$$

Here σ (the disorder parameter), determines the width of the density of states.

Without the presence of an external electric field, charge carriers are likely to diffuse towards energy states at lower energy through hopping. If a charge carrier hops from state i to state j, the hopping rate is given by Miller-Abrahams equation: [68]

$$v_{ij} = v_0 \exp\left(-2\gamma\Delta r_{ij}\right)\exp\left(-\frac{E_j - E_i}{k_B T}\right), E_j > E_i$$
$$v_{ij} = v_0 \exp\left(-2\gamma\Delta r_{ij}\right), \qquad E_j < E_i \tag{2.3}$$

Here v_0 is the frequency at which the charge carriers attempt to hop between different states, γ is the coupling matrix element between the two states and Δr_{ij} is the distance between the two states. It can be seen from Equation 2.3 that hopping most likely occurs from a state of high energy state to one of lower energy, although the reverse process is also possible, the rate is significantly lower.

In the presence of an external electric field, the concept of charge carrier mobility (μ) needs to be introduced. Physically, this is the speed of a charge carrier under per unit of electric field. In a disordered material, it is impossible to derive an analytical expression for μ, however, a phenomenological equation has been developed [66] in which μ is dependent on the electric field and temperature.

To measure the mobility in organic semiconductors, there are three main techniques used: organic field effect transistors (OFET), time of flight (TOF) measurement and space charge limited current (SCLC) conduction. In this thesis, mobility is determined by SCLC, and so the other two methods will not be discussed here.

In order to determine electron or hole mobility in a BHJ film, an electron or hole only device is used in which only one type of charge carrier is injected. When the applied electric field is sufficiently high and the injecting contact is ohmic, the current flow is space-charge limited, and the mobility can be derived from Mott–Gurney's law: [69,70]

$$J = \frac{9}{8}\varepsilon_0\varepsilon_r\mu\frac{V^2}{L^3} \tag{2.4}$$

Here J is the current density, ε_0 and ε_r are vacuum relative and permittivity, μ is the charge carrier mobility, L is the thickness of the active layer and V is the effective applied voltage.

In a BHJ OPV device, both the donor (conduct holes) and acceptor (conduct electrons)

phases contact with the electrodes, recombination at these interfaces becomes a potential loss mechanism due to the competition between drift (J_{drift}) and diffusion (J_{diff}) currents at the electrode interfaces. However, in a layered OPV device, the donor phase is only in contact with the anode, and it is true for acceptor and cathode; thus the diffusion induced loss in layered devices is not as significant as that in BHJ devices.

In an OPV device, the built-in electric field drive holes to the anode and electrons to the cathode. Under operation, the applied voltage works against the built-in field, when applied voltage increases, the effective electric field decreases. Therefore, for low applied voltages the electric field is relatively strong, the charge drift current predominates over the diffusion current, while the applied voltage is high, the effective field is small, the diffusion current predominates at the electrode interface. In this case, more charge carriers diffuse to the "wrong" electrode, which is also populated by holes, leading to recombination losses. [71] Such recombination losses can significantly reduce the shunt resistance and FF, this will be discussed in 2.4.7. From this point of view, in a BHJ OPV device, the HTL acts as the electron block layer simultaneously and ETL acts as hole block layer similarly.

In general, for organic semiconductor material, the diffusion length is given by $L_{diff} = \sqrt{D\tau}$, here D is the diffusion coefficient and τ is the lifetime of the charge carrier. According to Einstein relation, ($D = \mu k_B T / e$) D is determined by the charge mobility of the material. The drift length instead is given by $L_{drift} = \mu \tau E_{eff}$. For a certain material, the diffusion length and drift length can be estimated by the above equations.

2.4.6 Charge extraction

When a charge carrier arrives at an electrode, it must be extracted from the device. The efficiency of extraction is mainly determined by the nature of the electrodes and the contact made with the electrodes. The choice of suitable electrodes and optimisation of the structure of the BHJ is known to be critical in achieving efficient charge extraction.

To create an ohmic contact, the work function of the cathode should match the LUMO level of the acceptor material and the work function of the anode should match the HOMO

level of the donor material, as shown in Figure 2.9. In a metal-insulator-metal (MIM) structure, a built-in potential occurs because of the difference in the work function of the two metal electrodes. However, if an ohmic contact is achieved the built-in potential is instead determined by the donor HOMO level and acceptor LUMO level. [33-35]

In reality, hole/electron transport layers are usually employed between the photo-active layer and electrodes to optimise the contact. [36] Hole/electron transport buffer layers can improve the energy alignment between anode (cathode) and the donor (acceptor) materials, and are essential to create high performance organic solar cells. In addition, buffer layers can be used to change the architecture of organic solar cells from a standard structure to an inverted one. This idea will be present in a later section.

Hole/electron transport layers are generally chosen on the basis of their energy levels and transport properties. One of the most significant roles of the buffer is to transport and collect a single type of charge carrier and to block charges of the opposite polarity. It is worth emphasising that the charge selective property of buffer layers is critical in BHJ solar cells, in which the donor and the acceptor materials can both make direct contact with the anode and cathode.

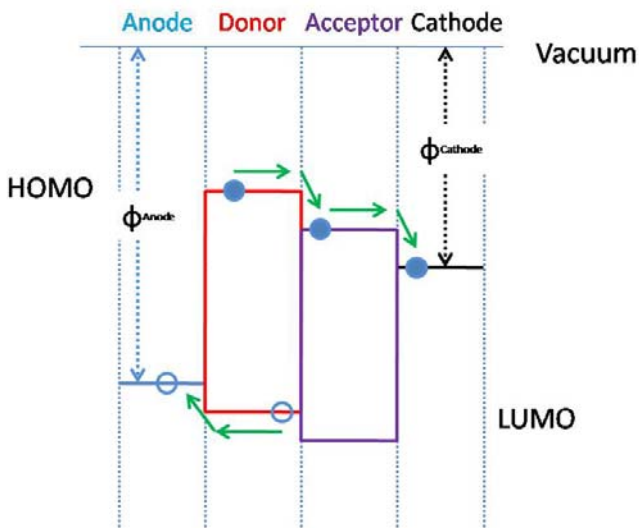

Figure 2.9 Diagram of energy levels of different parts in an organic solar cell

2.4.7 The characterisation of OPV devices

We now discuss the evaluation of the performance of an OPV device. This method is in fact applied generally to characterise solar cells, and involves measuring the photo current as a function of applied voltage whilst the device is illuminated with simulated sunlight. The equivalent circuit of an OPV device is shown in Figure 10.

The capacitor of the BHJ is only effective under dynamic stimulus. The electrical impedance spectroscopy (EIS) is a commonly used tool to investigate the internal process within the OPV devices. This is realized through fitting the EIS to equivalent circuits, or drift/diffusion models.[72,73] OPV devices convert light input to an electrical output; thus it is possible to use an alternative light-driven spectroscopy, namely intensity modulated spectroscopy (IMS), to study the dynamics internal processes.[74] Adhitya et al. developed a cost effective IMS system and it was used to investigate the degradation behavior of a polymer: fullerene OPV devices. [75]

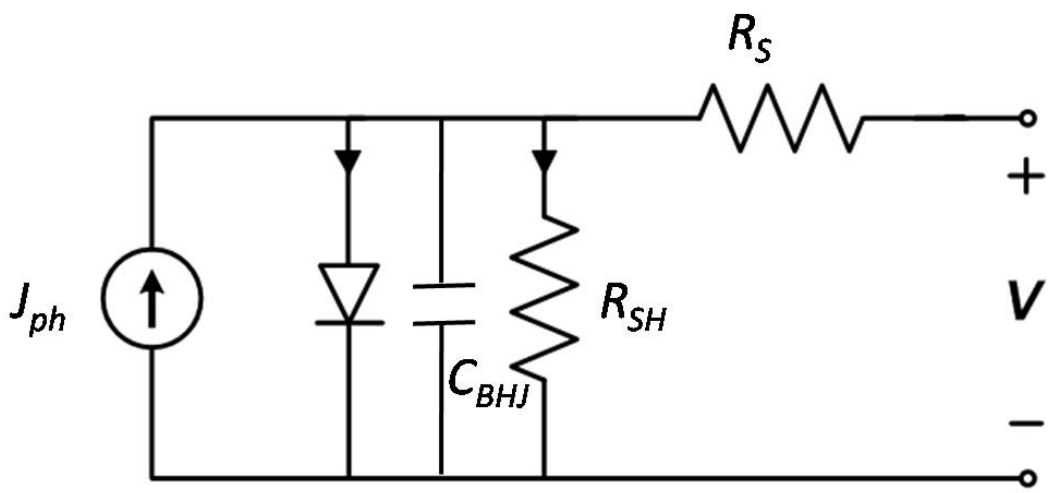

Figure 2.10 Equivalent circuit of an organic solar cell.

For a simpler situation where the OPV devices are characterised under DC electrical condition, the capacitor in Figure 2.10 can be ignored. To present a analytical expression of applied voltage and current density, the traditional inorganic solar cell models was often

employed. The JV characteristics of a solar cell can be simply expressed by a modified diode JV equation:[71]

$$J = J_0\left[\exp\left(\frac{e}{nk_BT}\left(V - JR_S\right)\right) - 1\right] + \frac{V - JR_S}{R_{SH}} - J_{ph} \tag{2.5}$$

Here, J_0 is the dark current density, n is a diode ideality factor with a value between 1 and 2, J_{ph} is the photo current density and R_S and R_{SH} are the series and shunt resistance of the device. To interpret the JV curve and working behaviour of OPV devices, a typical current density (J) vs applied voltage (V) curve of an organic solar cell under illumination is presented in Figure 2.11.

The corner of blue box denotes the maximum power point (P_{max}), the fill factor is extracted by comparing it with the theoretical maximum power output from the device. There are several important parameters that determine a solar cell's quality.

First, open circuit voltage (V_{OC}) is the voltage value at which there is no current through the device. Therefore, in Equation 2.5 J=0, and we ignore R_{SH} here for simplification, the following equation is obtained:

$$V_{oc} = \frac{nk_BT}{e}\ln\left(\frac{J_{ph}}{J_0} + 1\right) \tag{2.6}$$

It can be seen the V_{oc} is largely dependent on the J_{ph}, as J_{ph} is linearly correlated with irradiance level; therefore the V_{oc} is exponentially dependent on irradiance level. This has been confirmed by Cowan et al. [76] in PCDTBT:$PC_{71}BM$ based OPV devices. However, as reported by Rand et al. [77] when the irradiance is large, the shunt resistance in Equation 2.5 can be decreased and not be ignored anymore and it plays a significant role to decrease V_{oc}.

However, the dependence of V_{oc} on temperature in a BHJ OPV device is rather complicated and sometimes contradictory because the various recombination is also thermal related which cause the loss of V_{oc}. Riedel et al. [78] found in a BHJ solar cell based on OC_1C_{10} –PPV (poly[2-methoxy-5-(3,7-dimethyl octyloxy)-1,4-phenylene vinylene]): PCBM the V_{oc} increases gradually upon cooling the device down to 125K. In general, the dependence of V_{oc} on temperature can attribute to two terms: the tail states in HOMO and LUMO levels, the

recombination within the device. [79] The quantitative expression can be written as:[79]

$$V_{oc} = \frac{\Delta E_{DA}}{e} - \frac{\sigma^2}{ek_BT} - \frac{k_BT}{e}\ln\left(\frac{N_AN_D}{np}\right) \tag{2.7}$$

Here ΔE_{DA} is the difference between donor HOMO and acceptor LUMO, σ is the width of the tail state, $N_{A/D}$ is the total density of hole/electron states, p/n represents the concentration of hole/electron. From the angle of material, the V_{oc} is largely determined by the HOMO level of donor and LUMO level of acceptor. Therefore from Equation 2.7, it can be seen that the dependence of V_{oc} on temperature is determined by the dominant term between the second and third part. For P3HT:PCBM based OPV device, below 200K, it is the second term in Equation 2.7 dominates, with higher temperature, V_{oc} increases; while for temperature about 200K, a linear decrease is observed with temperature rises, this is because at higher temperature, the recombination term dominates.[79]

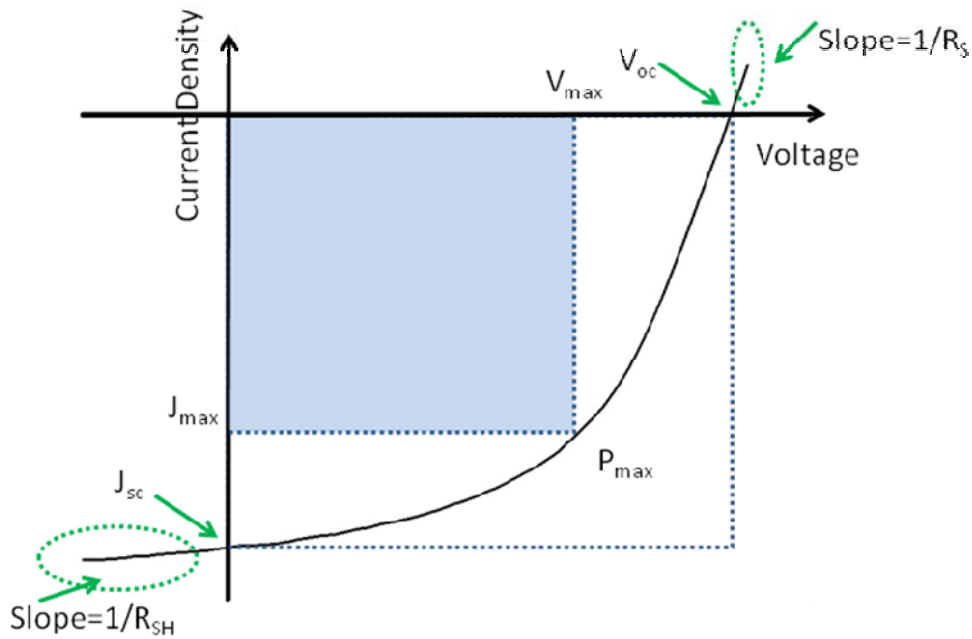

Figure 2.11. A typical JV curve of organic solar cells.

Secondly, the short circuit current density (J_{SC}) is the current density that flows when no external bias voltage is applied. It is positively related with irradiance level and temperature.

As the stronger irradiance can induce more photon absorption, higher temperature can improve the charge mobility and thus increase J_{SC}.

The fill factor (*FF*) can be determined using the following expression:

$$FF = \frac{P_{\max}}{V_{OC} \times J_{SC}} \tag{2.7}$$

Where P_{max} is given by the product $J_{\max} \times V_{\max}$. *FF* is shown in Figure 2.11 as the ratio between the areas of the blue and the white boxes.

The power conversion efficiency (PCE) is thus defined as

$$PCE = \frac{V_{OC} \times J_{SC} \times FF}{P_{in}} \tag{2.8}$$

where P_{in} is the light power incident on the device.

The series and shunt resistance are also reflected by the shape of the JV curve (Figure 2.11). These parameters significantly influence the FF of a device.

Another important characteristic parameter of an OPV device is the quantum efficiency which has a spectral dependence. The external quantum efficiency (EQE) is determined by the ratio between the number of charge carriers generated by a device and the number of photons with certain wavelength range that are incident on it. It can be written analytically as

$$EQE(\lambda) = \frac{Jhc}{P(\lambda)\lambda e} \tag{2.9}$$

where c is the speed of light, λ is the wavelength, $P(\lambda)$ is the incident optical power at certain wavelength λ.

If the absorption of light by the device is taken into consideration (rather than the incident light), it is possible to calculate the internal quantum efficiency (IQE). It can be seen that EQE is determined by absorption of the material and IQE.

It has been shown that geminate recombination reduces IQE (EQE as well) and causes reduced photocurrent (J_{ph}). [80-83] Ideally, the slope near the y-intercept should be zero, which is representative of the scenario in which all geminate pairs dissociate with 100% efficiency, (internal quantum efficiency is 100%) regardless of applied voltage. However as shown in

Figure 2.11, the non-zero slope indicates reduced quantum efficiencies and photocurrent. [80-83] The nonzero slope near the y-intercept is a traditional signature of a shunt current loss.[84,85] However, here we see another possible cause, which is less photo generated current at low applied voltage, thereby leading to reduced fill factor and J_{SC} performance relative to the ideal case.[83,86] We also observe some reduction in V_{oc} from this simple analysis. Experimentally, OPV devices with low donor–acceptor HOMO-LUMO energy offsets typically produce JV curves similar to the cases in Figure 2.11.[87,88]

Similarly, non-germinate recombination results from a variety of sources including trap, mobility and cell area effects [89-93] and can induce quite similar effects on illuminated device JV curve as shown in Figure 2.11.

To summarise this section, R_S is the combined effect of series resistance, contact resistance with the electrodes and the sheet resistance of the electrodes. The origin of series resistance relates to various mechanisms that causes a loss of current density. The parameter R_{SH} accounts for all the current leakage within the device including charge diffusion to the wrong electrode and pin-holes. Ideally, a large shunt and a small series resistance are needed to create an efficient device.

2.5 Scalable Fabrication Techniques of OPV devices

A key advantage of organic semiconductor materials is that they are soluble in many common organic solvents. This allows good quality, uniform thin films to be prepared over large areas using cheap solution processes. In order to transfer the fabrication of OPV devices from laboratory to factory, techniques appropriate for large scale coating have been developed. These include spray coating, blade coating, slot die coating and ink jet printing. In the following sections, some typical scalable solution based fabrication techniques will be introduced. We note that spin coating is not compatible with large volume manufacture, however it is discussed as it is the most commonly used film deposition technique.

2.5.1 Spin coating

Although spin coating is not suitable for high volume fabrication of OPV modules because it is a relatively slow technique and a lot of material is wasted during the spinning; it is still widely used in laboratory and research of OPVs as it can be used to create high uniformity films. The spin coating process can be divided into four stages as shown in Figure 2.12.

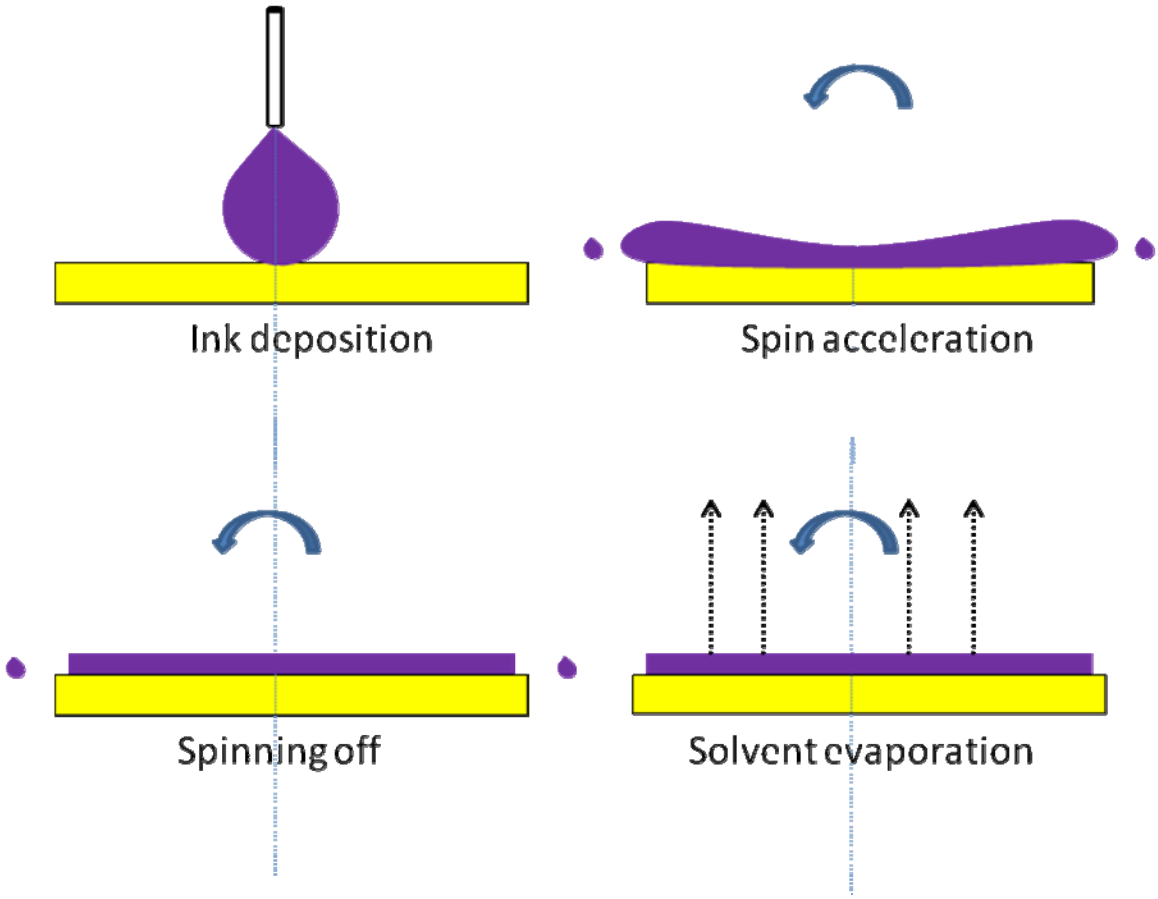

Figure 2.12 Four stages of a spin coating process.

First, the ink is dispensed onto the centre of the substrates. An excess quantity of ink is needed to prevent the ink drying before it reaches the edge of the substrates. The substrates are then accelerated to the desired rotation speed. During this stage, the ink flows across the substrate by centrifugal force. Most of the ink is spun off the substrate at in this stage, thus spin coating is a relatively wasteful film deposition method. Following this, the film becomes

thinner primarily by further mass loss and evaporation until most of the solvent has been removed and the viscosity is high enough to stop the liquid flow. Finally, any remaining solvent evaporates from the resultant film and the film vitrifies. Indeed, evaporation occurs throughout the whole spin coating process, but in the final stage, it is the dominant film formation mechanism

The thickness of the resultant film can be controlled by varying the ink concentration and solvent quality. However, the most convenient way to adjust the thickness is by changing the spin speed as film thickness is inversely proportional to the square root of the spin speed. This is expressed by the following equation:[94]

$$d \propto \frac{c\eta(c)}{\sqrt{\omega}} \tag{2.9}$$

Here, c is the concentration of the ink and $\eta(c)$ is a viscosity parameter that is related to the concentration. It is worth noting that the spin speed cannot be reduced to a very low rate as it must provide enough centrifugal force to allow the ink to spread over the whole substrate surface.

However, there are two main drawbacks of spin coating. First of all, spin coating is a slow fabrication process as spin coating cannot compatible with roll to roll fabrication processes. A second disadvantage is its low material use efficiency. In most cases spin coating utilises only a small fraction of the material dispensed onto the substrate, with most of the material spun off and wasted. This waste increases the cost of the process as many conjugated polymers are very expensive. To realise a commercial manufacture process for OPV devices, it is essential to develop a scalable fabrication technique.

2.5.2 Spray coating

Spray coating is one of the scalable fabrication techniques that are compatible with roll to roll (R2R) manufacture. [95-99]

To optimise a spray process, the properties of the solvent, such as surface tension, viscosity and boiling point must be taken into consideration. These properties of the solvent

can significantly affect the solution atomization, solvent evaporation and the spreading on the substrate. For low viscosity liquid, the breaking up of droplet is determined by the Weber number (W_e), which represents the ratio of the aerodynamic forces and the stabilising surface tension:[100]

$$W_e = \frac{\rho V^2 D}{\sigma} \tag{2.10}$$

Where ρ is the gas density, V is the initial relative velocity between the gas and the liquid, D is the initial diameter of the droplet and σ is the surface tension of the droplet. Larger Weber number correspond larger deforming external pressures forces which drive the breakup of the droplet.

The parameter of Ohnesorge number is used to characterise the ratio of drop viscous forces to surface tension forces, which is given by:[100]

$$O_h = \frac{\mu}{\sqrt{\rho D \sigma}} \tag{2.11}$$

Here, μ is the viscosity of the liquid, other parameters have the same meaning as in Equation 2.10. It is found by Faeth et al. [101] that for larger Ohnesorge number, the value of Weber number required to break up the droplets increases.

Besides the droplets breakup, the droplets impingement on the substrate to form a continuous film is also tightly related to the solvent properties. In addition to the parameters included in Weber and Ohnesorge numbers, the wettability of the solution on the substrate is also crucial to create a uniform and continuous solid film. [102]

The last step of the spray coating process is the drying of the solution on the substrate; this is determined by the solvent boiling point, substrate temperature, and the conditions of the surrounding air.[103]

The most commonly used type of spray coater is an airbrush spray coater as shown in Figure 2.13. Here, the spray deposition parameters are controlled by the nitrogen flow rate with the ink being sprayed out though a nozzle. The drawback of this technique is that the ink

droplet size is relatively large. This can affect the uniformity of such films as droplets merge on the substrate, with large droplets reducing film uniformity. Ultrasonic spray coating however is a nozzle-less system. Here the spray tip vibrates at ultrasonic frequency that generates a small, uniform droplet mist; a crucial element in the creation of high-quality, uniform films. [104]

The movement of the spray head is controlled by a computer-controlled gantry which ensures coating precision and high reproducibility. Substrates can be heated using a hotplate to control the drying time. The resultant thickness of a sprayed film can be controlled by changing solution concentration, air pressure, spray height and lateral spray speed. This opens a large parameter space to optimise the fabrication process.

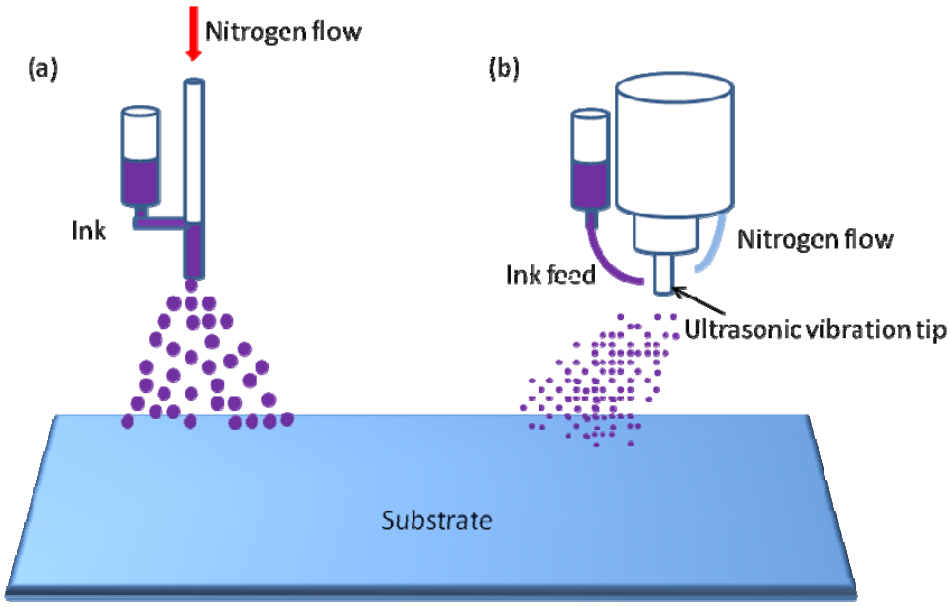

Figure 2.13 Schematic of (a) airbrush spray coating and (b) ultrasonic spray coating set-up.

Notably, most work on the development of spray cast organic solar cells have explored blend of the polymer poly (3-hexylthiophene) (P3HT) and (6, 6)-phenyl-C61 butyric acid methyl ester (PCBM). These materials are seen as being a prototypical OPV system, but are limited by relatively low PCE.[105] Girotto et al. [99] fabricated the HTL (PEDOT:PSS) and active layer (P3HT:PCBM), and a device efficiency of 3.75% was achieved. Vak et al. [106] reported the efficiency of 4.2%, which is the highest record for spray coated P3HT:PCBM based OPV

devices. More recent work has however explored spray-cast blends of amorphous donor-acceptor co-polymers with fullerene-derivative electron acceptors, with improved device performance demonstrated. [95,97,100,107] Wang et al. [97] optimized the solvent, solution concentration and other spray coating parameters, and obtained efficiencies of 4.3%, 4.5% and 4.6% for OPVs made from a blend of $PC_{71}BM$ with D-A copolymers Poly[N-9'-heptadecanyl-2,7-carbazole-alt-5,5-(4',7'-di-2-thienyl-2',1',3'-benzothiadiazole)] (PCDTBT), poly[9-(heptadecan-9-yl)-9H-carbazole-2,7-diyl-alt-(5,6-bis(octyloxy)-4,7-di(2,20-bithiophen -5-yl) benzo[c][1,2,5]thiadiazole)- 5,5-diyl] (P2) and poly[9-(heptadecan-9-yl)-9H-carbazole-2,7-diyl-alt-(5,6-bis-(octyloxy)-4,7-di(thiophen-2-yl) benzo[c][1,2,5]thiadiazole)-5,5-diyl] (P1). According to their study, the surface roughness of spray-coated films was almost the same as that of spin-coated films. In follow-up work, Scarratt et al. [108] enlarged the active area of an ultrasonic spray cast PCDTBT: $PC_{71}BM$ based solar cell to 165 mm^2 and obtained an efficiency of 3.7%. These reports indicated that spray coating is a promising technique to produce OPVs based on D-A copolymers having efficiency as high as comparable spin coated devices.

2.5.3 Blade coating

Blade coating is a one dimensional coating technique that can also be used in roll-to-roll fabrication. Figure 2.14 shows a schematic of a blade coating system. Here ink is directly dispensed onto the substrate which moves horizontally under a sharp blade that is fixed at a certain distance above the substrate. The gap size between the substrate and the blade controls the volume of material passing through the gap and thus the resultant film thickness. It is worth noting however that the thickness of the wet film is not equal to the gap size. The surface energy of the substrate, viscosity and surface tension of the ink also play an important role in determining the wet film thickness. Typically, the thickness of the final dried film (d) is given by the following empirical expression [109]

$$d = \frac{1}{2} g \frac{c}{\rho} \tag{2.10}$$

Here g is the gap width between the blade and substrate, c is the concentration of the ink

and ρ is the density of the dried film.

This technique has also been used in OPV device fabrication. [109,110] Chang et al. achieved an efficiency of 3.8% for P3HT: PCBM based solar cell using blade coating; a value comparable with spin coated devices. A significant advantage of blade coating is its economical efficiency. This is because most of the solution is used to form film with very limited material waste. However, blade coating is a slow process compared with spin coating. Because of this, blade coating is not suitable for materials that have tendency to crystallise or aggregate in solution.

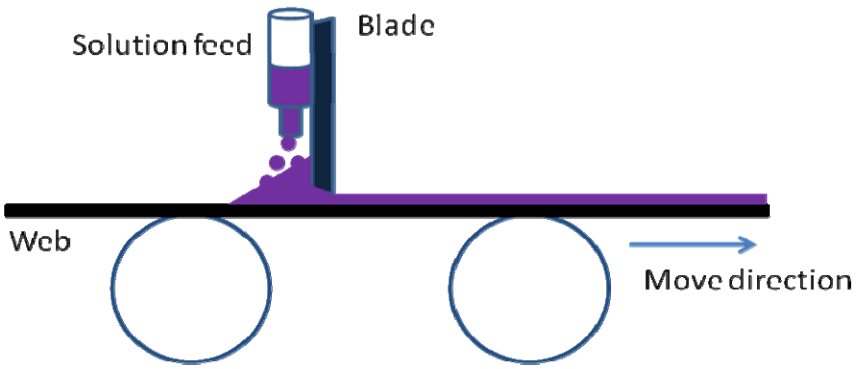

Figure 2.14 Schematic of a blade coating system

2.5.4 Slot die coating

Currently, the most commonly used high volume solution processed fabrication technique in OPV devices is slot die coating. This is a similar coating technique with blade coating; the core part of a slot die coater is the coating head, the width of the slot can be controlled through a mask allowing fabricating stripes of material, this is particularly suitable for manufacture of OPV devices consisting of several layers in vertical direction. Slot die coating is a cost-effective coating technique with all the solution supplied to the coating head is coated onto the moving web (see Figure 2.15). The solution feed to the coating head can be controlled by a pressure system.

In principle, the thickness of the resultant wet film is determined by the move speed of the web and the amount of solution feed to the coating head. For the thickness of the dry film,

it can be estimated as:[109]

$$d = \frac{fc}{Sw\rho} \tag{2.11}$$

Here where f is the solution feed rate, S is the move speed of the web, w is the width of the slot, c is the concentration of the solution and ρ is the density of the dried film.

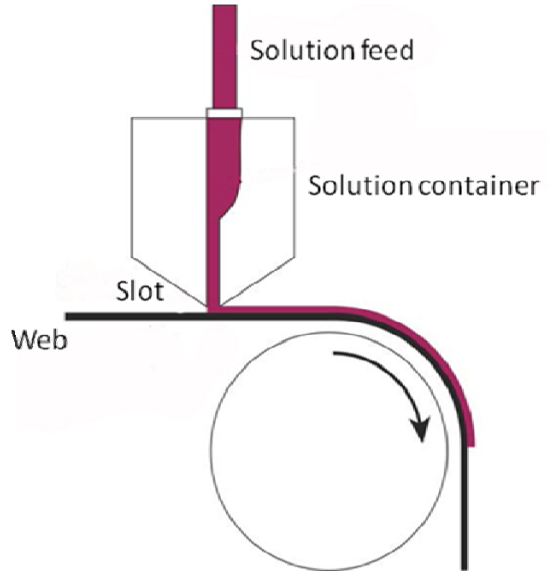

Figure 2.15 Schematic of a slot die coating system.

Slot die coating has been employed in the all solution roll-to-roll fabrication of OPV devices. Krebs [111] demonstrated a efficiency of 0.3% on OPV devices with the PEDOT:PSS, zinc oxide, silver grid and P3HT:PCBM layers all fabricated by slat die coating. Although the efficiency is still low, it is a pioneering attempt to realise roll-to-roll fabrication of OPV devices. Helgesen et al.[112] reported OPV devices fabricated with slot die coating having an efficiency of 3.5%. Lucera et al. [113] fabricated OPV devices on flexible substrates using slot die coating and efficiency of 4.25% was achieved. These results indicate that slot die coating is a promising coating technique to fabricate high efficiency OPV devices in high volume.

2.6 Stability of OPV devices

High efficiency is not the only requirement for the commercial application of OPV, as

stability is an important attribute that needs to be taken into consideration. Unfortunately, research on device stability properties is still at an early stage compared with research on efficiency enhancement. Recently, a number of research groups, including us, have begun to focus on investigating the source of instability of OPV and to use this information to extend device lifetime.

2.6.1 Lifetime testing strategy

A standard testing strategy for OPV lifetime is essential for the research community; otherwise different research groups come to different conclusions. The ISOS 1, 2 & 3 summits established some protocols for OPV lifetime measurement. These protocols include dark storage, outdoor testing, indoor accelerated testing, thermal cycling tests etc. The details of outdoor lifetime tests, which will be used in this thesis, are summarised in Table 2.3.

Three Levels	**Description**					
Basic (1)	**Manual measurements using simple equipments and few conditions.**					
Intermediate (2)	**Fixed conditions and protocols suit for most laboratories.**					
Advanced (3)	**Standardized tests applied in certified laboratories. Extended range of parameters to be monitored.**					
Test Type	**Test ID**	**Light source (stress)**	**Tempt.[1)]**	**R.H. [2)]**	**Environ.[3)]**	**Light source (test)**
Outdoor	ISOS-O-1 Outdoor	Sunlight	Ambient	Ambient	Outdoor	Simulator
	ISOS-O-2 Outdoor	Sunlight	Ambient	Ambient	Outdoor	Sunlight
	ISOS-O-3 Outdoor	Sunlight	Ambient	Ambient	Outdoor	Simulator and sunlight

[1)] Temperature; [2)] Relative Humidity [3)] Environment

Table 2.3 Summary of outdoor lifetime testing methods. This table is adapted from Ref. 52 [52].

2.6.2 Stability of active layers

It is believed that the aromatic ring and the side chains of organic semiconductor materials are vulnerable to attacks by oxygen and water under ambient atmosphere, with chemical reactions changing the chemical structure and electrical properties. When organic semiconductor materials are exposed to illumination, photolytic and photochemical reactions occur. For many materials, these reactions require the participation of light, water and oxygen. Chemical reactions are believed to be one of the main causes of OPV degradation. [64]

A further degradation process results from changes in the morphology of the polymer/fullerene blend. Here the fullerene forms nano-scale domains which usually grow in size with time. [114] This growth increases the length scale of phase separation between donor and acceptor, and reduces the efficiency of charge separation. One possible way to solve this problem is through chemically engineering by covalently, connecting the donor and acceptor parts, creating more stable bi-continuous networks.[115,116]

Indeed, thermal effect can significantly drive the evolution of nano-scale morphology. Recently, it is found that[117] light exposure of devices based on PCDTBT/$PC_{61}BM$ under irradiance of about 10 mW cm^{-2}, followed by thermal annealing under moderate temperature was able to increase the thermal stability of a device. It was found that the increased stability resulted from the dimerization or oligomerization of $PC_{61}BM$. However other work[118] on PDTSTzTz/$PC_{61}BM$ based OPV devices demonstrated that charge carrier mobility reduced significantly under similar light exposure. These seemingly contradictory results suggest that for systems comprising different materials, similar treatments can produce different effects. Here the complexity of the BHJ OPV devices is clearly at the heart of this problem and more work is required to determine the underlying physics.

One of the recent inspiring developments of OPV is the gradual increase of device efficiency; the design and synthesis of new donor-acceptor polymer is the main impetus. Devices based on poly (benzodithiophene-co-thieno[3,4-b]thiophene) (PBDTTT)-based material have realised over 10% efficiency. [119] Among these polymers, poly[(4,8-bis-(2-ethylhexyloxy)-benzo(1,2-b:4,5-b')dithiophene)-2,6-diyl-alt-(4-(2-ethylhexyl)-3-fluorothieno[3,4-b]thiophene-)-2-carboxylate-2–6-diyl)] (PTB7) emerged since 2010 [120] and

attract great research concentration. [121-125] Poly[4,8-bis(5-(2-ethylhexyl)thiophen-2-yl)benzo[1,2-b;4,5-b']dithiophene-2,6-diyl-alt-(4-(2-ethylhexyl)-3-fluorothieno[3,4-b] thiophene-)-2-carboxylate -2-6-diyl)] (PBDTTT-EFT) is another commercial available PBDTTT-based polymer, OPV devices based on it have achieved efficiencies of over 10%.[60,119,126] Despite of high device efficiency, PBDTTT-based polymers suffer from the relatively bad stability. [127-129] It has been found by Kettle et al.[130] that the degradation of PTB7:$PC_{71}BM$ based OPV devices is caused by the change in PTB7 chemical structure. They also found that the degradation of PTB7 is a 2-step process and is particularly susceptible to the presence of oxygen and illumination simultaneously. The instability mainly comes from the alkoxy side chains. Pearson et al. [131] found in PBDTTT-EFT:$PC_{71}BM$ based OPV devices, after the degradation, active layer nanostructure and kinetics of free charge generation is not proved to change, thus the degradation of device efficiency was attributed to generation of charge trapping states and suppressed charge carrier dissociation. As the chemical structures of PBDTTT-based polymer are similar, the degradation of this family of polymers is supposed to be similar as well.

Recent research has shown that PCDTBT based OPV devices have pretty good chemical stability with an extrapolated working lifetime as long as 7 years claimed. [132] However, the OPV devices based on PCDTBT:$PC_{71}BM$ undergoes fast initial efficiency loss, which is characterised as burn-in process.[133] The fast efficiency loss was attributed to the photochemical reaction occurring in the polymer.

2.6.3 Stability of metal electrodes

Aluminium (Al) and calcium (Ca) metal films are often used as the cathode material in OPVs because of their low work function, which also makes these metals highly reactive with water and oxygen. After reaction, a layer of metal oxide forms between the active layer and the electrode. As the metal oxide is insulating, a barrier is built for the charge extraction, which eventually results in device degradation. Glatthaar et al.[134] found a thin-current limiting layer near the electrode is responsible for the low fill factor of OPV devices. This result suggests a corroded metal contact can significantly reduce the fill factor and create a S-shaped

JV curve instead of the exponential diode JV curve. The formation of an interface layer between aluminium and the active layer has also been reported by Paci et al. [135] Their X-ray reflectometry studied in MDMO-PPV: PCBM based OPV devices indicates the presence of the interlayer in degraded devices.

Inverted device structure can avoid using of low work function metals; instead metals with good stability, such as silver, can be employed. Due to the less reactive nature, the stability of OPV devices with silver electrode is better under the exposure of moisture and oxygen. [136]

2.6.4 Stability of hole/electron transport layers

PEDOT: PSS is frequently used as a hole transport layer, however it is a highly acidic material whose pH is about 1-3. [136]As this layer is usually deposited from aqueous solution; the water present can also contribute to corrosion especially if low work function metal electrodes are used. Voroshazi et al. [137] attribute the efficiency degradation to the hygroscopic nature of PEDOT:PSS layer, the ingress of water into the PEDOT:PSS layer through the edge of the devices results in the progressive degradation of active layer and electrodes. Kim et al. found the acidity of a PEDOT:PSS solution can be modified by adding NaOH; a strategy that can increase device lifetime by 25%.[138] Several researchers have focused on the replacement of PEDOT: PSS with other materials. [139,140] Yun et al. [141] prepared reduced graphene oxide via solution process and used this material as hole transport layer in conventional structure OPV devices based on P3HT:PCBM, comparable device efficiency and better stability has been demonstrated.

Here metal oxides such as molybdenum oxide have been widely used as alternative to PEDOT:PSS. The most common fabrication of MoO_x is through thermal evaporation. [142] However, recently more reports about solution processed preparation of MoO_x have emerged. Hammond et al.[52] developed a low-temperature, solution-processed molybdenum oxide (MoO_x) fabrication technique which is compatible with high-volume roll-to-roll manufacture; replacing PEDOT:PSS with the MoO_x in conventional P3HT:PCBM based OPV devices, similar efficiency was achieved. Lee et al. [143] reported the use of solution processed MoO_x

nano-particle as hole transport layer in OPV devices, the device performance is at the same level with devices having evaporated MoO_x and PEDOT:PSS hole transport layers; and the air stability is better.

Recently, Bovill et al. found that PCDTBT: $PC_{71}BM$ based OPV devices with conventional structure using a PEDOT: PSS hole transport layers had better stability than devices utilising MoO_x or V_2O_5 as hole transport layers. This result was in contradiction to other work on P3HT: PCBM based devices in which devices employing PEDOT: PSS hole transport layer had worse stability. The difference between the two systems was attributed to the insensitivity of PCDTBT to moisture trapped in the PEDOT: PSS layer. [144]

Several materials have been utilised as the ETL in organic solar cells to replace the active metal Ca, and their influence on device stability was investigated. Jin et al. [145] found that a thin cadmium selenide (CdSe) interlayer (5 nm) can retard the degradation of OPV devices. Zinc oxide (ZnO) has also been used as an ETL because of its high electron mobility. The impact of ZnO on the shelf-life of organic solar cells has been reported by Ferreira et al.[80] It was found that using a ZnO ETL dramatically improves shelf lifetime of unencapsulated P3HT: PCBM OPV devices.

2.6.5 Encapsulation

Because organic materials are rather sensitive to oxygen and water, the encapsulation of OPV devices is a natural strategy to extend the device lifetime.

To evaluate the quality of an encapsulation, the concept of water vapour transmission rate (WVTR) was introduced. It is a measure of the amount of water vapour through a layered material over a certain time period with the unit of $g/m^2/day$. [146] It has been shown that the WVTR should be smaller than 10^{-6} $g/m^2/day$ for OLEDs to achieve adequate lifetime.[147] The global standard for OPV devices has not established yet. However, Cros et al. [148] found in OPV devices, with more stable electrode employed, the requirement of WVTR to obtain several years lifetime is expected to be about 10^{-3} $g/m^2/day$. This lower requirement for WVTR is favourable to develop low cost encapsulating solutions.

Ideally, OPV devices should be completely sealed in a chamber containing an inert atmosphere; however this significantly increases their cost. A more economical encapsulation technique is to use a top glass slide that is fixed onto the substrate using glue. This technique however sacrifices the flexibility of the devices and so it cannot be easily scaled up to create large area and flexible devices. A more practical approach is to use plastic films which are laminated on top of the device. This technique is easy to realise on industrial scale as lamination is a very mature technique. The use of polyethylene terephthalate (PET) foil is the earliest encapsulation method for large area OPC devices. [149] But it is not proved to be effective enough.

Madakasira et al. [150] explored the use of multiple layers of parylene and aluminium oxide for solar cells encapsulation and it is found that this type of multilayer barriers are effective to protect P3HT:PCBM based OPV devices from degradation. Exposing the devices under AM1.5 illumination for 8 hours did not cause serious degradation in the device efficiency. Sarkar et al.[151] reported the use of atomic layer deposited ultrathin barrier layers of Al_2O_3, the most stable devices retained 80% of the initial efficiency after storing in ambient for over 500 hours.

It has been found that [152] for roll-to-roll fabricated OPV device modules, the edge or the connections is the most vulnerable part as the moisture and oxygen can ingress through the edge. With proper seal of the edge, the stability of the devices is greatly improved; however, this approach loses the adaptability of integration with other functional devices.[152]

Roll-to-roll fabrication of OPV modules requires a barrier material having sufficient low WVTR and is compatible with a separate roll-to-roll step. In some researches, the PET[153] and ethylene vinyl acetate (EVA)[154] are used to laminate the OPV modules.

Currently, large series or parallel connected Si-based PV modules can be laminated to increase the outdoor lifetime and with the development of material and laminating techniques, we believe that the technique barriers of encapsulation of OPV modules should be overcome in the coming years.

2.6.6 Degradation behaviour of organic solar cells

Figure 2.16 presents a typical degradation curve for a PCDTBT: $PC_{71}BM$ based OPV device. It can be seen that the device undergoes a rapid loss of PCE in the initial operation stage; a process known as burn-in process.[133]

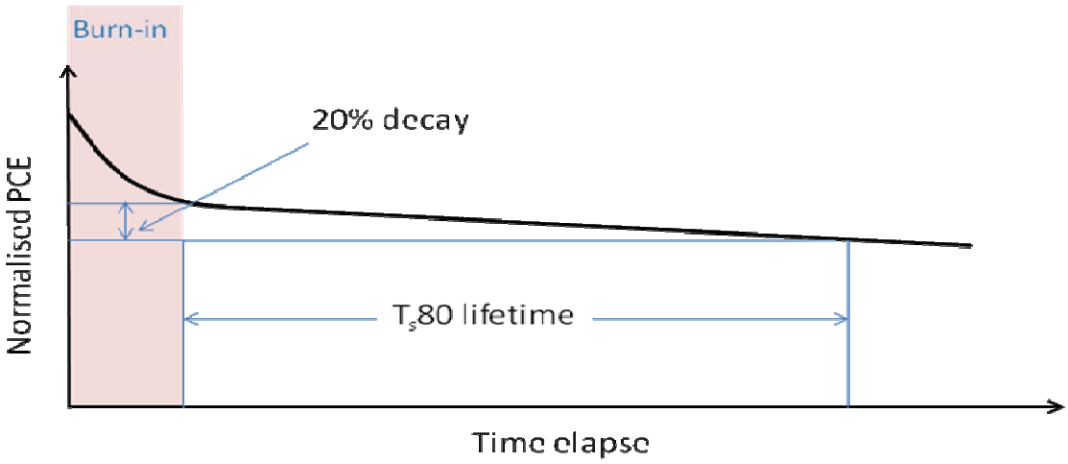

Figure 2.16 Typical degrading behaviour of an organic solar cell.

The mechanism of burn-in, as mentioned previously, has been attributed to photo-induced reactions in the active layer and the formation of sub-band gap states. These states can act as traps and enhance the recombination of charge carriers. Furthermore they increase the energetic disorder within the active layer and make the extraction of charge becomes rather difficult. An important feature of the burn-in process is that it is initially fast but then slows and finally stops, suggesting that the amount of reactive species is limited and can be depleted.

After burn-in, linear decay behaviour is often observed. The lifetime of OPV devices is characterised by the parameter T_s80 lifetime. This is extracted from the time point when the efficiency drops to 80% of its value at the end point of burn-in. The end of the burn-in process is defined as the end of the initial fast exponential decrease of the efficiency or the start point of the linear degradation of efficiency. Admittedly, in some cases the accurate determination of this point is not easy; however, in long-term lifetime study, the inaccuracy induced by this can be ignored. Sometimes the parameter T80 is quoted, which is defined as the time over which the efficiency decays to 80% of its initial value (i.e. before burn-in). Clearly, T_s80 is

longer than T80 and sometimes more than 20% efficiency is lost during the burn-in period. For this reason, the T80 lifetime can be short, but not necessarily result in a small T_s80.

Finally, it worth to note that the burn-in process is not necessarily occurs in OPV devices, it depends on the active layer material. [132] For carbazole-based donor-acceptor polymers like PCDTBT, the burn-in process is one of the most important features.

2.6.7 Indoor lifetime testing

Like Si-based PV techniques, the OPV devices are desired to work for years efficiently. The 10/10 target for organic photovoltaics (10% efficiency and 10 years lifetime) requires not only high efficiency but also good stability. The International Symposium on OPV Stability (ISOS) has published a consensus on the stability testing protocols recommended for OPV research that provides a set of guidelines for researchers involved in OPV stability studies. [155] Such protocols have since improved the comparability of OPV stability studies conducted by different researchers.

However under real working conditions for PV devices, we can expect parameters such as temperature, humidity and irradiance level to change, which will clearly affect device degradation; which makes the degradation behaviour is rather complicated. However, the collection of real-world lifetime data is usually time-consuming, and to collect data in a more efficient way, accelerated testing is essential. It is clear that the majority of OPV stability studies have been performed under well-controlled laboratory conditions. [136,156-158] Haillant et al. [159] reviewed techniques used in accelerated weathering tests of OPV devices. There are three methods to accelerate degradation: increasing irradiance level and exposure time, increasing the temperature and increasing the humidity.

It is known that all organic semiconductors degrade under concentrated illumination exposure and thermal stress. The acceleration factor (AF) caused by increased temperature and irradiance can be expressed analytically as follows:[160]

$$AF = \left(\frac{I_1}{I_2}\right)\exp[\frac{E_a}{k_B}(\frac{1}{T_2}-\frac{1}{T_1})] \tag{2.12}$$

Here E_a is the activation energy of the degradation process, k_B is a Boltzmann constant with T_1 (I_1) and T_2 (I_2) being temperature (irradiance) under testing conditions 1 and 2 respectively.

This model is simplistic with the assumptions as follows: 1) the activation energy E_a value over the considered temperature range is constant. 2) the linear dependency of the rate with irradiance is true in the range of sunlight in day time. This may not be the case at high irradiances such as several times the standard AM1.5 spectrum. 3) the component of the light is not considered as the UV light is determined to be detrimental to the device lifetime.

Because different materials undergo different reactions with water, there is no general rule for humidity related accelerated degradation. Hauch et al. found very limited influence of 65% RH on the lifetime for a large number flexible OPV modules.[161]

Most of the indoor lifetime studies were conducted under constant irradiance, by calculating the energy dose received by the devices, the lifetime in real-world conditions can be extrapolated.[132] However, this assumption just takes the energy dose into consideration and ignored the complexity in real-world conditions.

2.6.8 Outdoor lifetime testing

Stability studies recorded in a laboratory can simulate the seasonal temperature variation, the periodic illumination between day and night, even the seasonal humidity fluctuation. However it is difficult to simulate the combination of all these factors in a realistic way. In the absence of such a protocol, testing the device lifetime in the outdoors under real world conditions allows us to characterise degradation and understand underlying physical mechanisms.

F. C. Krebs and his colleagues undertook pioneering work on outdoor lifetime testing on OPV devices. In 2006, [162] they reported the operational stability of OPVs based on three materials: MEH-PPV: PCBM, P3HT:PCBM and P3CT:C60. Although the devices degraded rapidly with their test lasting less than 2 months, it is still of great importance as it was the first attempt to test the stability in real world conditions. In 2008, researchers from Konarka

Inc. [163] investigated the lifetime of flexible P3HT:PCBM based OPV modules both under laboratory conditions and in an outdoor environment. They found the flexible modules had good light stability after 1000 hours continuous light soaking in laboratory with the outdoor testing results being very promising; after over 1 year's outdoor exposure the modules survived without serious performance losses. In 2011, a consensus stability testing protocol for OPVs was established and this provided a standard process under which to conduct outdoor stability research. Since then, Krebs and partners undertook several inter-laboratory outdoor stability studies on OPVs. [164-166] These works demonstrated that the climate in different locations can induce different degradation behaviours. Following an inter-laboratory long-term outdoor lifetime test on R2R coated P3HT: PCBM devices, [164] it was found that the temperature of the devices at the different locations was the main reason for different degree of stability observed. The importance of encapsulation was also demonstrated; good or bad encapsulation can vary the operation lifetime of an OPV device from a few hundred hours to more than 10000 hours.

Using a packaged lifetime testing suitcase, outdoor device characterisation was conducted in 45 different laboratories worldwide, and an 8% deviation of device performance was determined in the different locations.[166] This was found to be a rather small variation considering the various impact factors.

In another study, [165] Krebs and his colleagues found that ITO-free OPV modules retained 95% of their initial performance after 1 year of outdoor operation and they predicted that following improvement of the electrical contacting system, device lifetime could be extended to between 3 and 5 years.

Krebs et al. [167] then described and analysed the performance, practicality, installation speed and energy payback time of an organic solar farm. The installation rate is of great important because after fabricating in an efficient roll-to-roll process hundreds of meters of deployable OPV foil need to be installed in an efficient, safe and cheap manner. They found that a high voltage installation based on OPV devices connected in series can result in an installation rate of several Watts per minute, a value that far exceeds any other existing PV technology. Furthermore, the payback time in different locations is always predicted to be

shorter than a year. This is promising result for the practical application of OPVs. It was also highlighted that more effort is needed to make grid electricity from organic solar farm a reality.

Some other studies also involved the real world lifetime study for a short period. Teran-Escobar et al. [168] test the P3HT:PCBM based solar cells and found the devices having a $V_2O_5 \cdot H_2O$ HTL have good stability and the UV filter is beneficial to improve the stability for OPV devices. Josey et al. [169] tested the real-world stability of some fullerene free OPV devices for around a week and conclude the chemical structure of acceptor molecular has significant impact on the device stability. Some other studies also focus on the diurnal performance under real-world conditions of OPV devices. The dependence of device performance on temperature and light intensity is established.[170,171]

For large volume of OPV modules, there should be two ways to connect each individual pixel: serial for high voltage and parallel for high current. In practise, [172] the serial connection of large amount of individual solar cells is realised by printing an ITO-free solar cell stack. By carefully design the pattern, a total voltage of 8.2 kV was achieved with 16000 pixels connected properly. By connecting individual solar cell pixels serially it makes the energy extraction easier: contacting at opposite ends of the series. This allows long lengths of solar cell modules. The high voltage also avoids the issue of high current densities and enables a light-weight system using only thin cables. [167]

Theoretically, different connection strategies should have some impact on the device stability. However the serial connection is the case in practical and should draw more attention.

2.7 Strategies to optimise active layer micro morphology and device performance

As discussed previously, the micro morphology of the active layer in an OPV device can significantly influence its performance. For BHJ OPV devices, the morphology of the BHJ films is largely dependent on the late film drying process, which is dominated by the slowest evaporating solvent. Thus several strategies have been developed to modify the morphology

of a BHJ film to harvest the device efficiency.

Thermal annealing is a post film-deposition technique that can modify the morphology of a P3HT/fullerene blend thin film and thus impact upon its photovoltaic properties, including PCE.[173] Such benefits come from the increased crystalline of P3HT. Here enhanced crystallinity improves the mobility of the photo-generated charge carriers.

In contrast in most D-A copolymer /Fullerene blend systems, thermal annealing has a negative impact on OPV device performance. For example, in PCDTBT/$PC_{70}BM$ devices, the PCE can be only slightly improved by thermal annealing below 80°C, [97] however annealing above this temperature reduces device efficiency. In devices based on many other low band gap copolymers (such as PBDTTPD[174]), thermal annealing even at relatively moderate temperatures will reduce photovoltaic performance dramatically. The reason for this is that many D-A polymers are relatively amorphous compared to P3HT, and thus thermal annealing cannot effectively improve the degree of the crystalline of such materials. The slight improvement produced by thermal annealing under moderate temperatures most probably comes from the removal of any residual casting solvent. [175]

Another method used to improve OPV device performance is through solvent processing to control the phase separation and the nano-scale morphology of the active layers and interfaces. As different polymers have different solubility in different solvents, the use of different solvents/solvent mixtures has been used to control the morphology of the film and consequently improve the device performance. For PCDTBT a based OPV device, chlorobenzene (CB) is the most popular casting solvent, giving devices with efficiency around 5%. [176]

The addition of a small amount of solvent additive to the main casting solvent has been proven to be efficient means to improve the efficiency of organic solar cells.[177] For instance, 4-bromoanisole (BrAni) is an effective and versatile solvent additive for P3HT: PCBM-based OPVs. [178] Because of its low volatility compared with the principal solvent, the crystallinity of P3HT can be increased greatly during solution processing. The selective solubility of the additive is believed to be a significant factor in improving device performance.

Hoven et al. [179] explored a narrow band-gap polymer named poly[(4,4-didodecyldithieno[3,2-b:2′,3′-d]silole)-2,6-diyl-alt-(2,1,3-benzoxadiazole)-4,7-diyl] (P1) which has a high tendency to aggregate. However when mixed with $PC_{70}BM$ the films spin coated from pure chlorobenzene solution showed highly complex surface features; when a small amount (2%, vol%) of 1-chloronaphthalene (CN) (a high boiling point solvent additive), was added to the solution, the heterogeneity was successfully reduced and as a result the device efficiency improved from 1.6% to 4.9%.

In this films based on the high efficiency OPV polymer PTB7, the addition of 1,8-diiodooctane (DIO), can improve mixing between PTB7 and $PC_{70}BM$ and thereby improve device efficiency. Here, it is believed that the DIO can dissolve $PC_{70}BM$ aggregates and allow the acceptor material to intercalate into PTB7 domains. This significantly reduced the domain size from 100 nm to approximately 20 nm. [120] Yao et al. [180] have also employed impedance spectroscopy to detect effect of the DIO additive on PBDTTT-C:$PC_{70}BM$ based OPV devices. Again it was shown that DIO can facilitate mixing between donor and acceptor and create smaller domain sizes. Huang et al. [181] investigated the impact of the DIO additive on the nano morphology and structure of PBDTTT-EFT:$PC_{70}BM$ blend films. Their GIWAX studies established that the addition of DIO can enhance the crystallisation of the polymer; with atomic force microscopy and transmission electron microscopy results indicating that DIO can largely reduce the formation of large domains, a feature that permits efficient charge dissociation and reduces device efficiency.

Solvent vapour annealing (SVA) is another popular method to optimize the morphology and performance of OPVs. SVA has been demonstrated to be an effective tool to improve the performance of PCDTBT/fullerene blend OPVs.[182,183] Expose to tetrahydrofuran (THF) and carbon disulfide (CS_2) mixed vapours have been proved to be a powerful method to improve the crystallinity of PCDTBT in the active layer of an OPV, consequently optimising device performance. [182] Furthermore, the aggregation of $PC_{70}BM$ is also enhanced by this process, creating a continuous path for electron transport. It was shown that after annealing in a THF and CS_2 (1:1) mixed solvent vapour for 5 min, the efficiency of the devices increased from 4.54% to 6.60%.

It has also been demonstrated that controlled exposure to chloroform is another effective way to engineer the nano-scale morphology of PCDTBT/ fullerene thin films and improve their performance. [183] This process has been used to improve efficiency in such devices from 4.2% to 5.5% after chloroform SVA. It was also shown that this improvement came from a large enhancement of J_{sc}. The J_{sc} of SVA treated devices was about 15% higher than those of devices without SVA treatment. In general, it appears that SVA is a promising technique to modify the nano-scale morphology and enhance the charge carrier mobility and also increase optical absorption, thereby optimising device performance.

Recently, a D-A copolymer, poly[(5,6-difluoro-2,1,3-benzothiadiazol-4,7-diyl)-alt-(3,3'''-di(2-octyldodecyl) 2,2';5',2'';5'',2'''-quaterthiophen-5,5'''-diyl)] (PffBT4T-2OD), has emerged. [21,184] OPV devices based on this material have been reported having a PCE up to 10.8%.[21,184]

Ma et al [185] studied the influence of processing parameters such as solution temperature, concentration, spin-rate and solvent quality, as well as the influence of polymer molecular weight on the morphology and properties of PffBT4T-2OD:$PC_{70}BM$ solar cells. Here, it was found that the molecular orientation and molecular packing can be tuned by adjusting the spin rate during spin-coating and the solution temperature for blend films, with a low spinning rate and low solution temperature inducing highly ordered face-on polymer packing, and a high spinning rate and high solution temperature producing poorly ordered edge-on polymer packing. The best OPV performance was achieved using films spun-cast at 800 rpm from a solution at 100ºC, creating a smooth film containing sufficient aggregates to yield a favourable morphology.

A detailed study of the processing methodologies to optimise the morphology of PffBT4T-2OD based OPV devices has however not yet been reported in the literature.

Experimentally, many different techniques have been used to study the morphology of polymer: fullerene BHJ systems, however difficulties remain in precisely determining the composition and size of the blend phases, the structure of the interfaces between phases and film morphology as a result of limited contrast between the materials in the blend. Despite the

fact that it is possible to distinguish between semi-crystalline conjugated polymers and fullerenes using electron and X-ray based techniques, determining the structure associated with amorphous materials is still challenging. Furthermore, techniques such as AFM only allow the morphology of the solid-air interface to be determined. However, as discussed in Chapter 2, film structure at this interface is often very different from that in the underlying bulk. One technique that can be used to probe such systems is neutron scattering. Neutron scattering has been highly effective in probing the structure of polymer: fullerene BHJs as contrast between these materials originates from differences in the scattering length density (SLD) of fullerenes compared to protonated conjugated polymers. For this reason, neutron scattering techniques such as Small Angle Neutron Scattering (SANS) [186-191] and Neutron Reflectivity [191-196] have provided new insight into the nano-morphology and vertical layer structure of bulk heterojunctions [197].

2.8 Summary

In summary, in Chapter 2.2 and 2.3, the origin of semiconducting properties of organic semiconductor materials are introduced as all the later chapters are based on this kind of material. In Chapter 2.4, I have discussed some of the key physics underlying the operation of organic photovoltaic devices, as well as an introduction of the characterisation of OPV devices. This information is relevant to all the following chapters in this thesis.

The scalable film fabrication techniques used in OPV is discussed in Chapter 2.5. A detail review on application of spray coating on OPV fabrication is presented here as well. This information is relevant to Chapter 4 and 5. In Chapter 4, spray coating is utilised to fabricate high efficiency OPV arrays over large area substrates. In Chapter 5, conventional and inverted OPV devices based on a high crystalline polymer is fabricated via spray coating in air.

The stability issue of OPV devices has been introduced in Chapter 2.6. The testing protocols as well as current status of stability research on OPV has been reviewed. This information is correlated to Chapter 7, where the real-world stability of PCDTBT:$PC_{71}BM$

based OPV devices is investigated.

The strategies to modify the morphology within a BHJ film are discussed in Chapter 2.7. This information is relevant to Chapter 6, in which the morphological engineering of OPV films using solvent additive and thermal annealing will be discussed. And the characterisation of PffBT4T-2OD:$PC_{71}BM$ BHJ film confirms the effect of solvent additive and thermal annealing on improving device efficiency.

Chapter 3 Experimental Methods

3.1 Introduction

In this chapter, the fabrication of OPV devices and various characterisation techniques employed in this thesis are introduced. Device fabrication involves substrate cleaning, solution preparation, thin film preparation via spin/spray coating, metal electrode deposition and device encapsulation. The characterisation methods used in this thesis include UV-vis absorption, photoluminescence spectroscopy, atomic force microscopy, spectroscopic ellipsometry, small angle neutron scattering and neutron reflectivity.

3.2 Device fabrication

3.2.1 Substrate cleaning

The glass substrates with pre-patterned ITO electrodes used in this thesis were purchased from Ossila Ltd. The thickness of ITO layer was 100 nm and had a square resistance of 20 Ω/square.

Without thorough cleaning, dust on the ITO surface will cause films to be created having poor uniformity. Residue on the ITO can also change the surface energy of the substrates thus influence their wetting properties. To clean the substrates, an ultrasonic bath filled with hot water was employed. The substrates were successively sonicated with Hellmanex solution, 2-isoproponal (IPA) and deionised (DI) water for 5 minutes for each step. The substrates were then blown dry using a nitrogen gas jet. Finally, the cleaning process ended with a 5 minute thermal anneal at 100 °C to completely remove any moisture.

3.2.2 Solution preparation

As mentioned in chapter 2, one of the advantages of OPV devices is that they can be processed from solution. In a BHJ OPV device, the donor and acceptor materials are mixed

together in the same solution. On deposition, the morphology of the BHJ film is a critical part of device performance and thus solution preparation is a key procedure.

The details of the materials used in solution preparation are listed in Table 3.1.

Material	Source	Product code	M_w	PDI
PEDOT:PSS	Ossila Ltd.	M121 (Al4083)	-	-
Zinc acetate dihydrate	Sigma-Aldrich	379786 (CAS:5970-45-6)	-	-
PCDTBT	Department of Chemistry, University of Sheffield	-	34000	2.21
$PC_{71}BM$	Ossila Ltd.	M113 (95% purity)	1031	-
PBDTTT-EFT	Solarmer Inc.	PCE10	>40000	1.8-2.0
PffBT4T-2OD	California Organic Semiconductor Inc.	DP0101	117,800	2.15

Table 3.1 Details of materials used in this thesis.

All solvents were purchased from Sigma-Aldrich.

The solution of PEDOT:PSS HTL used as the anode contact is used as received and was then filtered through a 0.45 μm PVDF filter. For spray coating, the filtered PEDOT:PSS solution was diluted by IPA and Ethyl Glycol (EG) at a volume ratio of 1:8:1.

The precursor gel used to prepare the ZnO ETL was made by dissolving 110 mg zinc acetate dihydrate in a mixture of 1 ml of 2-methoxyethanol and 30 μl of ethanolamine. The solution was stirred overnight in air to form a transparent gel. After this, it was ready for spin coating. For spray coating, the resultant gel was then diluted with methanol at a volume ratio of 1:8.

The preparation of active layer solution was dependent on the specific polymer. In general, donor and acceptor materials were weighted out at certain weight ratios after which they were transferred to a nitrogen-filled glove-box. Here the solvent was added to the dry material. The solution was then stirred with a magnetic stirrer and then heated to ensure all

materials dissolved. The details of the weight ratios of donor/acceptor, the solvents used, and the temperature at which the solution was heated are all listed in Table 3.2.

Donor/ Acceptor	Deposit technique	Solvent	Total concentration	Blend ratio	Heat temperature	Heat time
PCDTBT/ $PC_{70}BM$	spin	CB	20 mg/ml	1:4	70 °C	5 hours
PCDTBT/ $PC_{70}BM$	spin	CF	18 mg/ml	1:4	50 °C	5 hours
PCDTBT/ $PC_{70}BM$	spin	CS_2/ Acetone [a)]	18 mg/ml	1:4	50 °C	5 hours
PBDTTT-EFT/$PC_{70}BM$	spin	CB/DIO [b)]	30 mg/ml	1:1.5	80 °C	10 hours
PBDTTT-EFT/$PC_{70}BM$	spray	CB/DIO [b)]	5 mg/ml	1:1.5	80 °C	10 hours
PffBT4T-2OD/$PC_{70}BM$	spin	CB/DCB/ DIO [c)]	20 mg/ml	1:1.2	110 °C	10 hours
PffBT4T-2OD/$PC_{70}BM$	spray	CB/DCB/ DIO [c)]	5 mg/ml	1:1.2	110 °C	10 hours

[a)]At a volume ratio of 1:4. [b)]At a volume ratio of 97:3. [c)]At a volume ratio of 48.5:48.5:3. CB=Chlorobenzene (b.p.=131°C), DCB=Di-chlorobenzene (b.p.=180.5^{o}C) CF=Chloroform (b.p.=61.2^{o}C), CS_2=Carbon disulfide (b.p.=46.3^{o}C).

Table 3.2 Details of active layer solution preparation

3.2.3 Spin coating of thin films

The PEDOT: PSS HTL and ZnO ETL were both prepared via spin and spray coating. All these deposition was conducted in air. The parameters used in spin coating are listed in Table 3.3.

The active layers were also deposited by spin and spray coating. The spin coating was conducted in nitrogen-filled glove box. The fabrication details of the spin coating processes

are also listed in Table 3.3.

Material	Solvent	Environ.	Spin rate	Spin time	Substrate temperature	Post treatment
PEDOT:PSS	Water (DI)	Air	5000 rpm	30 s	R.T. [a)]	TA [b)] at 120°C for 5minutes
ZnO precursor	2-Methoxyethanol	Air	5000 rpm	30 s	R.T. [a)]	TA [b)] at 275°C for 10minutes
PCDTBT/ $PC_{71}BM$	CB	Glove box	1000 rpm	35 s	R.T. [a)]	No
PCDTBT/ $PC_{71}BM$	CF	Glove box	2000 rpm	30 s	R.T. [a)]	No
PCDTBT/ $PC_{71}BM$	CS_2/Acetone	Glove box	2000 rpm	30 s	R.T. [a)]	No
PBDTTT-EFT/$PC_{71}BM$	CB/DIO	Glove box	1800 rpm	30 s	R.T. [a)]	No
PffBT4T-2OD/$PC_{71}BM$	CB/DCB/DIO	Glove box	1000 rpm	30 s	110 °C	TA [b)] at 100°C for 5 minutes

[a)] R.T.= Room Temperature. [b)] TA=Thermal annealing

Table 3.3 Spin coating parameters used to deposit the different materials.

After thin film deposition, the edge of the substrate needs to be cleaned, as in our device architecture, the top electrode need to make contact with the patterned ITO electrodes. To clean the film edges, a cotton bud dipped into the solvent from which solution the film were cast was employed.

3.2.4 Spray coating of thin films

In this thesis, all the spray coating was conducted using a Prism 300 ultra-sonic spray coater (Ultrasonic Systems Inc.) that was operated in air under regular clean-room conditions.

This spray coater is a nozzle-less system, with the ultrasonic vibrating spray tip enabling the generation of a fine droplet mist.

Spray coating of PEDOT: PSS

PEDOT: PSS is the most popular HTL used in organic solar cells and in most of cases it is spin coated. However, there have been some successful attempts to spray coating a PEDOT: PSS hole transport layer.[198-200] In most of these reports, the active layer used was a P3HT: PCBM blend film. In this thesis we utilised a spray coated PEDOT: PSS HTL in PBDTTT-EFT:$PC_{71}BM$ and PffBT4T-2OD:$PC_{71}BM$ based OPV device.

Because of the aqueous nature of PEDOT: PSS, it is difficult to spray coat directly. To spray coat a PEDOT: PSS thin film, it is necessary to dilute the PEDOT: PPS (AI 4083) using 2-Propanol (IPA) and ethylene glycol (EG) according to the volume ratio 1:8:1. In the mixed ink, IPA improves wetting on an ITO coated glass substrate, with EG increasing viscosity of the films. During spray-coating, the substrates were held at 50°C to optimise the drying time of the films. As mentioned in Chapter 2, control over the spray coating parameters is crucial for optimising the uniformity and thickness of the resultant films. In this thesis, it was found that the distance between tip and substrate, the travel speed of the tip and delivery gas pressure should be set at 70 mm, 80 mm/s and 10 psi respectively to deposit a 30 nm PEDOT: PSS film having good surface uniformity. The films were then transferred to a hot plate at 120°C immediately after spray coating to undergo thermal annealing for approximately 20 minutes.

Spray coating of ZnO

In inverted devices, the active-layer blend is instead deposited on an electron-transporting layer such as zinc oxide (ZnO). Here, ZnO can be easily processed from solution using a sol-gel method, [201,202] with such materials also being compatible with deposition by spray coating.[98,203] For spray coating ZnO ETL, precursor gel used for spin coating was diluted with methanol at a volume ratio of 1:8 to reduce its viscosity and tune the wettablity. For spray-coating, the tip-substrate distance was kept at 45 mm, a lateral tip speed of 25 mm/s was used which created a uniform film having a thickness of around 25 to 30 nm. During

spray coating, substrates were held at room temperature. The films were then thermal annealed at 275 ºC for 5 minutes in air.

Spray coating of PBDTTT-EFT:$PC_{71}BM$

PBDTTT-EFT:$PC_{71}BM$ solutions for spray coating were prepared using a solvent mixture of CB and 3% (vol%) DIO as described in section 3.2.2. PBDTTT-EFT and $PC_{71}BM$ were blended at a weight ratio of 1:1.5 and dissolved at a total concentration of 5 mg/ml for. The PBDTTT-EFT:$PC_{71}BM$ blend films were spray coated onto the PEDOT:PSS layers fabricated both by spin or spray coating. During the spray coating, the distance between tip and substrate, travel speed of the tip and delivery gas pressure were held at 45 mm, 55 mm/s and 10 psi respectively. The substrate temperature was kept at 50 °C. These parameters processed films having a thickness of about 100 nm. The spray coating was conducted in air, and after depositing the active layers, the samples were immediately moved into a nitrogen-filled glove box to avoid further exposure to air and light.

Spray coating of PffBT4T-2OD:$PC_{71}BM$

To spray coat the PffBT4T-2OD:$PC_{71}BM$ active layer, we prepared an ink consisting of 1:1.2 weight ratio of PffBT4T-2OD:$PC_{71}BM$ dissolved at 5 mg/ml into a mixture of the solvents chlorobenzene (CB) and 1,2-dichlorobenzene (DCB) (volume ratio 1:1). The solvent mixture also contained a small (3%) volume concentration of 1,8-diiodooctane (DIO) in order to optimise the micro nanostructure of the BHJ film.[204,205] Before use, the ink was stirred at 110ºC for 5 hours to ensure the solids in the blend were fully solubilised. The active PffBT4T-2OD:$PC_{71}BM$ layer was then spray-cast onto the substrates held at 85°C. It was found that this substrate temperature encouraged the formation of a uniform film. Through extensive optimization spray trials, we determined that a spray tip velocity of 25mm/s at a tip-substrate separation of 45 mm and no extra gas pressure created films having a thickness 250 nm.

3.2.4 Top electrode deposition

After depositing the active layer, the substrates were transferred into a thermal evaporator which is connected to the glove box. In the vacuum chamber, top electrodes were

deposited via thermal evaporation. Normally, the base pressure during deposition was below 5 x 10^{-6} mbar. The film thickness and deposition rate of each material was monitored using a quartz crystal microbalance. The thickness and deposition rate for the buffer layers and electrodes are listed in Table 3.4.

Material	Role	Thickness	Deposition rate
Calcium (Ca)	Cathode buffer layer	5 nm	0.04 nm/s
Molybdenum oxide (MoO_x)	Anode Buffer layer	10 nm	0.04 nm/s
Aluminium (Al)	Electrode	100 nm	0.1 nm/s

Table 3.4 Thermal evaporation parameters used to deposit the different materials

3.2.5 Encapsulation

Before taking the devices out of the glove box, it is essential to encapsulate a device to prolong its lifetime. In this thesis, all the substrates were encapsulated using a glass slide which was fixed via UV-cured epoxy glue to cover all devices. The epoxy glue is purchased from Ossila Ltd. (with the product number of E131). It was exposed to UV-light for 30 minutes for solidification.

3.3 Photovoltaic characterisation

In order to evaluate the efficiency of OPV devices, it is conventional to use a standard light spectrum having a power density of approximately sunlight.

In our measurements, a Newport 92251A-1000 solar simulator with an AM1.5 spectrum and 1000W/m^2 output power was employed. A silicon solar cell certified by NERL was used as a reference to calibrate the solar simulator and a metal aperture mask was used to define the device area exposed to the illumination. To test the device, a voltage sweep from -1 V to 1 V was applied using a Keithley 237 sourcemeter which also recorded the photo current when the device was illuminated.

3.4 UV-vis absorption

The optical absorbance spectrum of various materials was measured using a Jobin Yvon Horiba Fluoromax-4 spectrometer, shown schematically in Figure 3.2.

Briefly, the system consists of four main parts: a lamp (light source), a monochromator, a reference detector and a transmission detector, which are located in the sample chamber.

The light source used was a Xenon lamp whose emission starts at 250 nm. After being focused by an elliptical mirror, the light emitted by the Xenon lamp enters the monochromator through a slit. Here the slit width controls both the resolution of the spectrometer and the intensity of the light entering the monochromator. A second mirror then collimates the light beam which is directed onto a diffraction grating. The diffracted light is reflected by a third mirror which is then incident on a slit. Using this process, only certain wavelengths can pass through the slits, with transmitted wavelength determined by the relative angle between the grating and the incident light. After exiting the monochromator, the light is directed to a beam splitter by a fourth mirror. Here part of the light is recorded by the reference detector, with the remaining component entering the sample chamber. The sample is held in a holder and is located perpendicular to the incident light. The transmission detector then collects the transmitted light, allowing the fraction of light absorbed to be calculated.

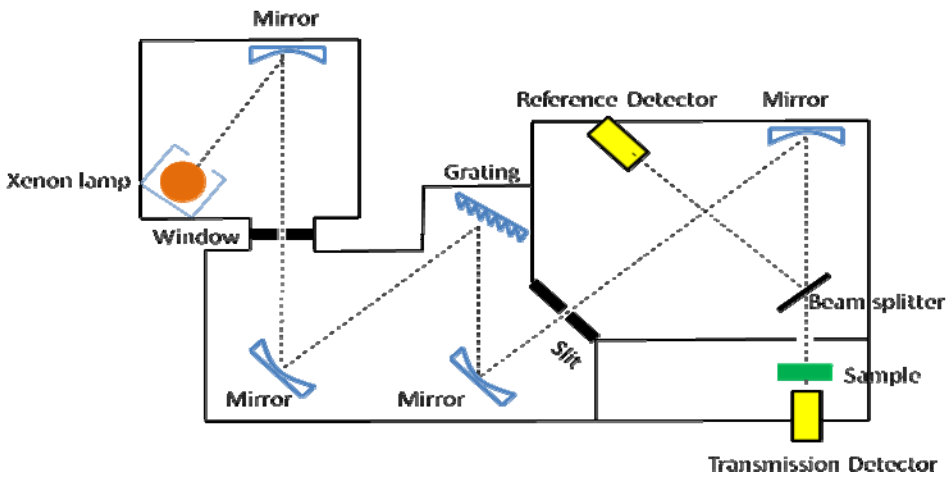

Figure 3.2. Schematic of Jobin Yvon Horiba Fluoromax-4 spectrometer.

The transmittance of the sample at wavelength λ can be expressed using:

$$T(\lambda) = \frac{I(\lambda)}{I_0(\lambda)} \tag{3.1}$$

where $I(\lambda)$ is the transmitted light intensity (recorded by the transmission detector), $I_0(\lambda)$ is the intensity of light incident onto the sample (measured by the reference detector). From this the absorption can be determined using Equation 3.2.

$$A(\lambda) = -\lg(T(\lambda)) = -\lg(\frac{I(\lambda)}{I_0(\lambda)}) \tag{3.2}$$

where $A(\lambda)$ is the absorption of the sample.

It is worth noting that not all of the light that does not reach the detector is absorbed by the sample. Rather reflection and scattering from the film also contribute to optical loss. To minimise such errors, a blank substrate is also measured which accounts for reflection and absorption in the substrate.

3.5 Photoluminescence (PL) spectroscopy

PL emission is widely used to investigate the optical and electronic properties of organic semiconductors. It can reveal information about the energy band gap and exciton behaviour. In OPV devices, PL is used to unravel the charge carrier behaviour and can provide indirect information regarding the nano-morphology of a BHJ film. [34,206,207]

A schematic diagram of the system used to measure the PL spectrum is shown in Figure 3.3. A diode laser with a wavelength of 532 nm was employed as the excitation light source. A neutral density filter was used to control the incident light intensity. The incident beam was then focused by a 100X objective lens having a 0.77 numerical aperture which focused the light beam to a spot having a diameter of 2.5 μm on the sample surface. This objective lens was mounted onto a 3-dimentional motorized stage which allowed the lens to be moved across the sample surface. The sample was held perpendicular to the incident laser and the emitted PL was guided into the detector through a long pass filter having a cut off wavelength of 532 nm. This was used to reject the incident laser from the collected signal.

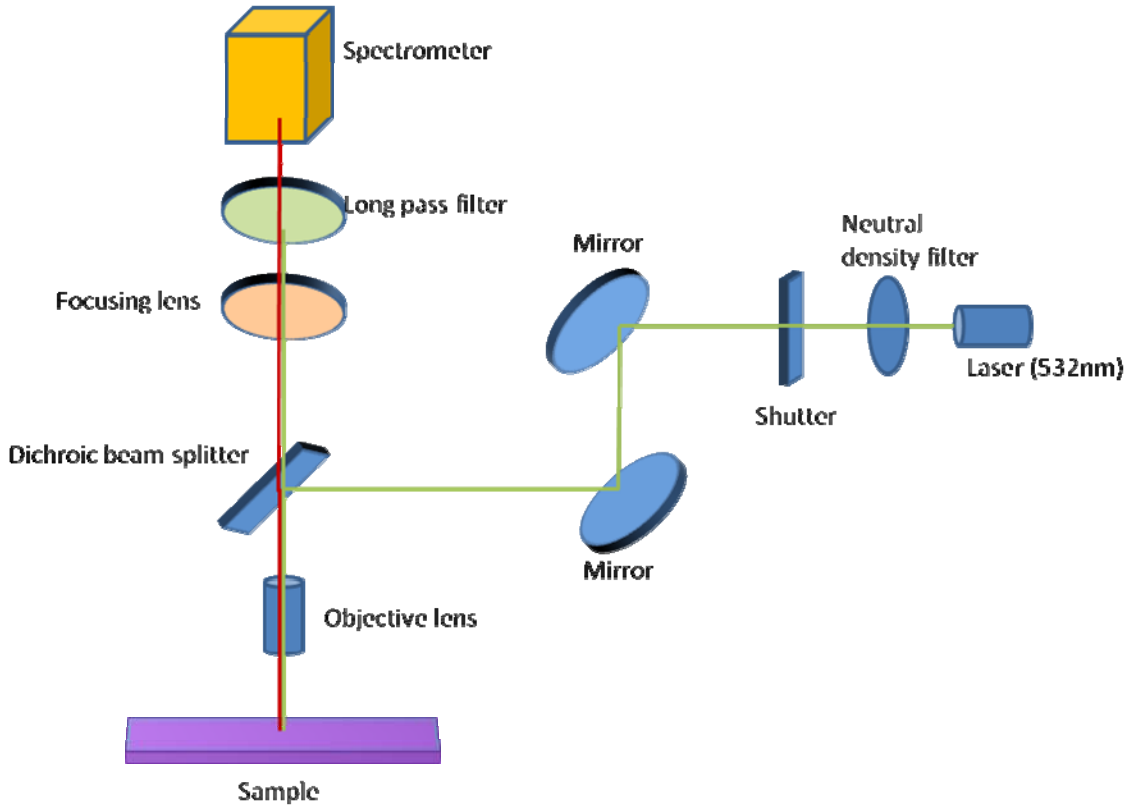

Figure 3.3 Schematic of PL measuring system

A Jobin Yvon 320 spectrometer was used to analyse the emitted PL. Within the spectrometer, two gratings with different line densities were used to diffract the light. This produced spectra having a resolution of 0.07 and 0.3 nm. Finally, a CCD cooled by liquid nitrogen was utilised to record the PL spectrum. The intensity of the PL spectra could be tuned by changing the integration time.

3.6 Atomic force microscopy

An atomic force microscope (AFM) is a common tool used to investigate the surface morphology of thin films. It is a type of scanning probe microscope (SPM). As shown in Figure 3.4, the core component is a cantilever having a sharp tip. AFM can work with the tip making contact with the sample (contact mode) or oscillating to make intermittent contact between the tip and the sample (tapping mode). In this thesis, tapping mode was used as polymer samples can be very soft, and thus tapping mode is used to minimise the damage to the surface.

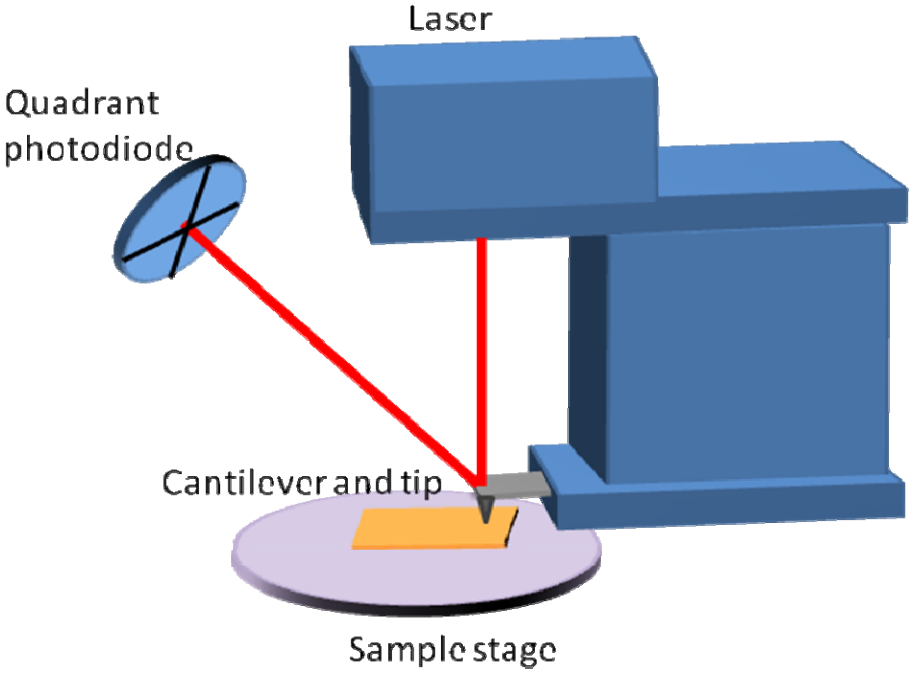

Figure 3.4 Schematic of an atomic force microscope

The sample stage is controlled by two electronic motors to move the cantilever around the sample surface (X and Y direction). An additional motor is used to control coarse movement along the vertical (Z) direction. A laser is incident onto the top surface of the cantilever and then reflected onto a four-quadrant photodiode. The displacement of the tip is then detected by the photodiode. In tapping mode, the cantilever is driven at its resonant frequency and the tip makes contact with the sample surface at its largest displacement. Here the "contact" is defined by the Van der Waals force between tip atoms and the sample surface atoms. Normally, the distance between tip and sample is several nanometres.

A feedback loop is crucial in an AFM system. As the distance of the tip and the sample changes due to variations in the height of the sample, the change in the reflected laser signal will be translated to an electronic signal which will instruct the piezoelectric actuator controlling Z direction motion to react to maintain a set-point tip-sample distance. By recording the relatively movement of the sample stage over the defined area, the topography of the sample can be imaged.

A phase image is performed by a separate module which can record the phase lag

between the cantilever drive signal and the signal sent to control the piezoelectric actuator in the Z direction at each “tap”. This phase lag is largely dependent on the material being studied and thus the phase image can distinguish domains of different stiffness; a property that is useful when imaging films containing more than one type of material or more than one phase of a single material.

In this thesis, a Dimension 3100 system (Vecoo Instruments) was used to perform AFM measurements. All measurements were conducted in tapping mode.

3.7 Spectroscopic Ellipsometry

Spectroscopic Ellipsometry (SE) can be used to measure the changes of polarisation of a light beam after reflection from a thin film. By modelling the signal, some optical information, including refractive index (n), extinction coefficient (k) and thickness of the sample can be determined. A schematic of a SE is shown in Figure 3.5.

In this thesis, a J A Wollam M2000v ellipsometer was used. It can be seen from Figure 3.5, the system has two arms, which make the same angle to the horizontal sample stage. A Xenon lamp light source was used having a wavelength range of 370 nm to 1000 nm. The light beam passes through a monochromator and a polariser before being incident on the sample. After reflection from the sample, the light is then directed into a detector arm.

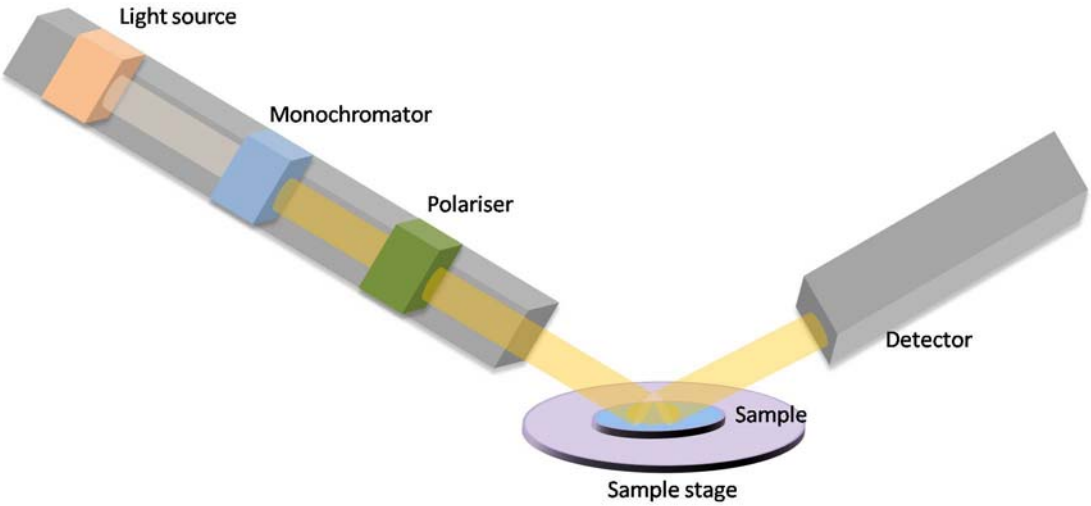

Figure 3.5 Schematic diagram of a spectroscopic ellipsometer.

The polarised light can be decomposed into two components: component oscillating perpendicular to the plane of incidence (s component), and component oscillating parallel to the plane of incidence (p component). After reflection and normalised to the initial value, the complex amplitudes of the two components are denoted as r_s and r_p respectively and measured separately, with the ratio between them defined as the reflectance ratio (ρ) which is a complex number.

$$\rho = \frac{r_p}{r_s} = \tan \Psi e^{i\Delta} \tag{3.3}$$

Here Ψ is the ratio between the two amplitudes and Δ is the phase difference before and after being reflected by the sample. Using these two parameters, the refractive index (n) and extinction coefficient (k) can be extracted by modelling Ψ and Δ as a function of wavelength. To determine the thickness of the film, a simple approach is to measure the wavelength region where no light is absorbed by the material (from 800nm to 1000nm). Therefore the extinction coefficient can be ignored (k=0). By employing a Cauchy dispersion model, the refractive index can be expressed as follows:

$$n = A + \frac{B}{\lambda^2} + \frac{C}{\lambda^4} \tag{3.4}$$

In this expression, A, B and C are all positive real numbers which are determined by fitting. With n obtained from Equation 3.4, the film thickness can be calculated through solving the Fresnel equations.

Using ellipsomtry, the glass transition temperature (T_g), at which an amorphous material transforms from a hard glassy state to a soft rubbery state can be determined. This is achieved by a dynamic measurement. A sample is heated, with Ψ and Δ being determined as a function of temperature. The film expansion rate can then be calculated, with the temperature at which the rate changes being identified as T_g.

3.8 Small angle neutron scattering

Small angle neutron scattering (SANS) is a type of small angle scattering (SAS) technique. In SANS, neutrons are elastically scattered by a sample, with the resultant

scattering pattern collected and analysed to investigate the shape, size and orientation of the components within the sample. SANS can probe structures with a length scale between 1 and 100 nm. The SANS facilities used in this thesis are located at LOQ at ISIS, STFC, UK. [208] The construction of LOQ is relatively simple, as shown in Figure 3.6. This consists of an evacuated beam line (11 m long) through which neutrons are incident onto the sample. At the beam line, the neutrons first fly through a Soller super mirror bender, with neutrons having a wavelengths less than 2 Å being removed. After this, an aperture selector is used for collimation. The neutron beam then enters a Frame overlap mirror, in which neutrons with wavelengths greater than 12 Å are removed. Before hitting the sample, the beam line is again collimated using a second aperture selector. The beam size at the sample is adjustable between 2 - 20 mm by the second aperture selector. The typical beam diameter is 8 mm.

Normally SANS requires samples with a relatively large thickness of several micrometres. To measure a single film that is much thinner than this, it is necessary to create a stack of samples.

After being scattered by the sample, neutrons are incident on a two-dimensional detector which is fixed 4 metres away from the sample. This detector can record the position and arrival times of the neutrons. It is shown in Figure 3.6, there are two separate detectors; the main detector collects scattered neutrons having a momentum transfer (q) in the range of 0.006 - 0.24 $Å^{-1}$. Neutrons with q in the range of 0.15 - 1.4 $Å^{-1}$ are instead collected by the high angle detector. Here the momentum transfer (q) is defined as

$$q = \frac{4\pi}{\lambda} \sin \frac{\theta}{2} \tag{3.5}$$

where θ is the scattering angle and λ is the incident wavelength (which in this case is 2.2 - 10.0 Å at 25 Hz chopper frequency).

To analysis the resultant scattering pattern, the relationship between intensity vs q is plotted. By modelling the scattering curve, information about the nano-morphology of the sample can be determined.

The measurements presented were recorded in collaboration with Dr. Andy Parnell and Dr. Gabriel Bernardo, University of Sheffield.

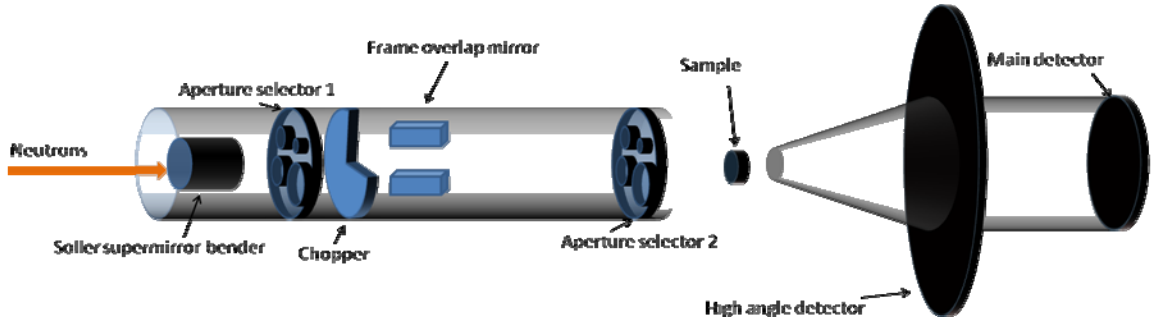

Figure 3.6 Structure of the SANS instrument: LOQ in ISIS UK.

3.9 Neutron reflectivity

Neutron reflectivity (NR) is another neutron technique used. The working principle is quite similar to neutron scattering, however the main difference is that unlike scattering, the neutrons are reflected by the sample as shown in Figure 3.7. As neutrons have greater mass than electrons, the electrons outside the nuclei are almost transparent to the neutron beam, and thus the neutron reflectivity pattern is sensitive to contrast arising from various nuclei. NR is an effective way to differentiate between various elements.

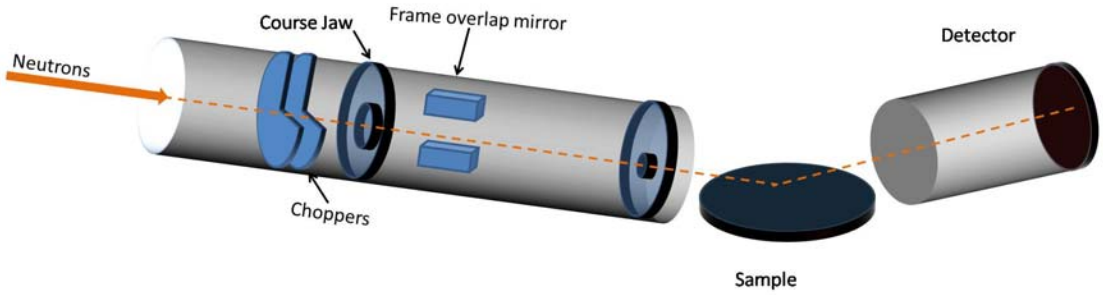

Figure 3.7 Structure of a NR instrument

The neutron reflectivity system used in this thesis is at INTER located at the ISIS neutron spallation source. The incident neutron wavelength of this system ranges from 1.5 Å to 14 Å with incident angles of 0.5º and 2.3º being used to cover the required momentum

transfer range. Again a frame overlap mirror is used to remove unwanted neutrons. In a NR measurement, the reflected neutrons are collected, and thus the substrates should ideally be completely opaque to neutrons. Because of this, silicon wafers with a thickness of several millimetres are a standard choice for NR. Furthermore, the reflection is quite sensitive to small bends of the sample, and thus more stable thick wafers are suitable for NR measurements.

NR data is analysed in an analogous manner to SANS, with the intensity as a function of momentum transfer recorded. To interpret the reflectivity profile, a model is developed that includes film thickness and neutron scattering length density (SLD). The vertical composition of the sample is then fitted using a model based on the assumption that the sample consists of a number of layers, having a particular thickness and SLD. Again, NR measurements were performed in conjunction with Dr. Andy Parnell and Dr. Gabriel Bernardo, University of Sheffield.

3.10 Outdoor lifetime testing

In order to explore the lifetime of OPV devices when used under real world conditions, an outdoor lifetime testing system was constructed. A photo of the system is shown in Figure 3.8.

The outdoor lifetime testing system was located on the Hicks Building rooftop which is in Sheffield, England (latitude and longitude of 53°22'N and 1°29'W respectively). The system is un-shaded to maximise the light flux received by the devices. It can be seen in Figure 3.8 that this system consists of three separate aluminium sample chambers which are each sealed by a toughened glass lid and rubber gasket. The sample chambers are connected to nitrogen cylinders through gas pipes. During operation, each sample chamber was filled with nitrogen at a slightly higher pressure than ambient to maintain the devices in an inert environment. In each chamber, 8 devices can be mounted, with all the devices being successively tested using a PXI-4132 multiplexer system. The PXI system is controlled by a computer that determines the PCE, J_{sc}, V_{oc} and FF of each device. There are also 8

temperature sensors mounted besides each device to continuously measure the temperature. The computer and multiplexer system were placed in a cabinet, as can be seen in Figure 3.8(a), to protect the hardware from rain, snow and wind. The sample chambers were fixed on top of the metal cabinet, and held at an angle of 30° with the horizon level as can be seen from Figure 3.8(b). All chambers point south to maximise the light flux incident to the samples.

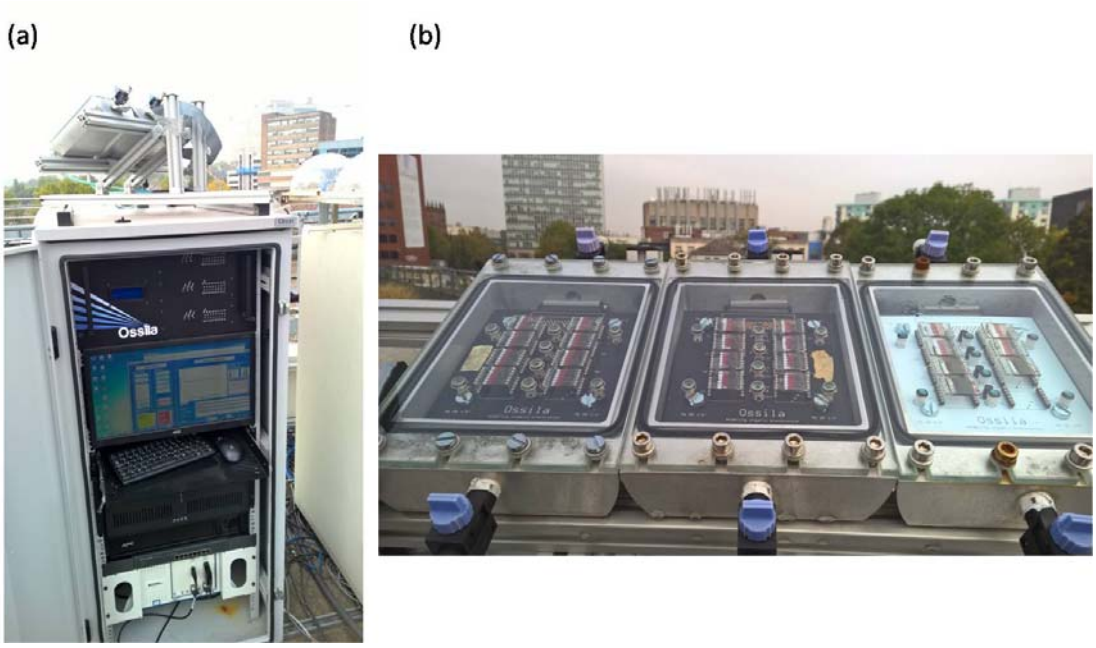

Figure 3.8 (a) The rooftop lifetime testing system in Sheffield. (b) The sample chamber of the lifetime testing system.

A pyranometer (SPN 1 Sunshine Pyranometer, Delta-T Devices) was employed to determine overall irradiance incident to the devices. This was used as reference to determine the incident power when calculate the power conversion efficiency. To double check the consistency and uniformity among different devices, 8 small silicon photodiodes were mounted in the testing chambers close to the devices being tested. The silicon photodiodes were equipped with visible colour filters to restrict their sensitivity to the wavelength range of 350 to 750 nm (Vishay VBPW21R).

The devices were tested sequentially at an interval of around 5 minutes, with the measurements performed from 6 am to 9 pm continuously every day. This period covered most of the day-time in Sheffield. Data processing is discussed in detail in chapter 7. During

measurement, the measurement system also recorded the temperature inside the chamber, the average humidity level outside the chambers and the irradiance.

A consensus on the stability testing protocols was published at the International Summit of OPV Stability (ISOS). Here our measurement follows the rule of intermediate level of outdoor testing (ISOS-O-2). A summary and comparison between the requirement of ISOS-O-2 and our testing setup is shown in Table 3.5.

	Items	**Requirement of ISOS-O-2[155]**	**Our outdoor lifetime testing system**
Testing setup	Light source	Direct sunlight	Fulfilled
	Mounting	Front side oriented towards the equator, at latitude angle	Fulfilled
	Load	Maximum power point or open circuit	Open circuit
	Temperature	Ambient	In the sample chamber.
	Relative humidity	Ambient	In the sample chamber.
	Characterisation light source	Sunlight	Sunlight
Testing protocol	Temperature	Monitored	Monitored
	Relative humidity (R.H.)	Monitored	Monitored
	Irradiance	Monitor irradiance and calculate accumulated irradiation	Fulfilled
	JV characterization	Full JV curve recording is preferred	Full JV curve was recorded
	Measurement intervals	15 minutes to 1 h is recommended	Around 5 minutes
Output strategy	Location/time	Report latitude, longitude and date	Fulfilled
	Irradiance and irradiation	Times of irradiance and JV measurement need to be recorded and correlated.	Fulfilled

	Exposure temperature/R.H.	Reported	Fulfilled
	Instantaneous performance parameters	Report J_{sc}, V_{oc}, FF and PCE	Fulfilled
	Stability parameters	Evolution of PCE, FF, Voc, J_{sc} with time and Ts80 calculated.	Fulfilled
	Measurement protocol and setup	Reported	Fulfilled

Table 3.5 The requirement from ISOS-O-2 and the corresponding details of outdoor lifetime testing system.

It can be seen from Table 3.5 that our outdoor lifetime testing system fulfils most of the requirements of ISOS-O-2, except for environmental temperature and relative humidity. In our system, the devices are located in a sample chamber, and thus the temperature inside the chamber is much higher than the ambient temperature. Similarly the relative humidity inside the chamber is lower than ambient because inside the chamber is kept filled with an over pressure of dry nitrogen as described above. Despite such inconsistencies, the data acquired using this system still follows the ISOS-O-2 protocol. Indeed the sample chamber can be considered as a type of encapsulation. Furthermore, the temperature and relative humidity data were effectively recorded "inside" the encapsulation, a feature that adds to the specification of the measurement.

3.11 Summary

In this chapter, the experimental techniques used in this thesis have been introduced. Chapter 3.2 describes the fabrication of OPV devices, including a detail introduction of spray coating of hole transport layer, electron transport layer and active layers. The content about device fabrication is relevant to all the experimental chapters; the spray coating is correlated

to Chapter 4 and 5. The characterisation of OPV devices is explained in Chapter 3.3, this part is relevant to all the experimental chapters. UV-vis absorption spectrum and atomic force microscopy are described in Chapter 3.4 and 3.6 respectively; these two techniques are used in Chapter 4, 5 and 6. Other techniques used in Chapter 6 including photoluminescence, spectroscopic ellipsometry, small angle neutron scattering, neutron reflectivity are presented in Chapter 3.5, 3.7, 3.8 and 3.9 respectively.

Finally the outdoor lifetime testing method is introduced in Chapter 3.10; Chapter 7 is based on this method.

Chapter 4 Fabrication of PBDTTT-EFT:$PC_{71}BM$ based solar cell arrays via spray coating in air

4.1 Introduction

In 2014, a polymer named poly[4,8-bis(5-(2-ethylhexyl)thiophen-2-yl)- benzo[1,2-b;4,5-b']dithiophene-2,6-diyl-alt-(4-(2-ethylhexyl)-3-fluorothieno[3,4-b]thiophene-)-2-carboxylate-2-6-diyl)] (also known as PBDTTT-EFT or PCE10) was reported, with OPV devices based on this material realising PCEs of over 9%.[61,209-211]

Notably, almost all of the high efficiency OPV devices reported based on PBDTTT-EFT have been prepared via spin coating in a glove box containing an inert atmosphere. Such progress motivated us to fabricate high efficiency OPV devices over large area substrates via spray coating in air.

In this chapter, OPV devices based on PBDTTT-EFT/$PC_{71}BM$ were fabricated via spray-coating in air onto substrates having an area of 5 x 5 cm^2. A single substrate was divided into arrays of 6 x 6 pixels; with the active area of each pixel being 2.54 x 2.54 mm^2. PEDOT: PSS hole transport layers were deposited via both spin and spray coating techniques. Each pixel was tested individually and it was found that for devices based on a spin coated HTL and a spray coated active layer, the PCE of the champion pixel was 8.75%. Devices with both HTL and active layer prepared by spray-coating had a maximum PCE of 8.06%.

The effects of light and air exposure of the active layer on device performance were also briefly explored, and were both found to be detrimental.

The device structures (both large area and small area reference devices) used in this chapter are shown in Figure 4.1.

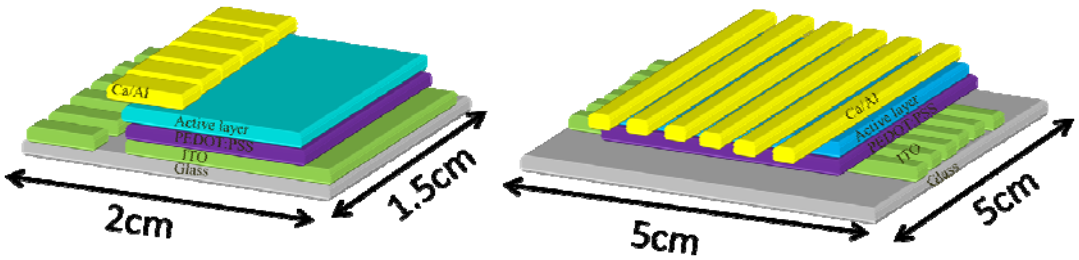

Figure 4.1 Schematic of device structures used in this chapter. Left: reference devices with small area pixels. Right: large area substrates with 36 working pixels.

4.2 PEDOT: PSS hole transport layer

PEDOT: PSS hole transport layer has been fabricated on large area substrate via spin and spray coating. The details of fabrication process have been described in Chapter 3.

The surface morphology of the PEDOT: PSS films prepared by spin and spray coating is characterised by AFM and presented in Figure 4.2(a) and (b) respectively. The root mean square (RMS) roughness of the spin coated PEDOT: PSS film was determined to be 1.4 nm. The spray coated film was slightly rougher (having a RMS roughness of 2.9 nm). This small increase was not however detrimental to the performance of the OPV devices.

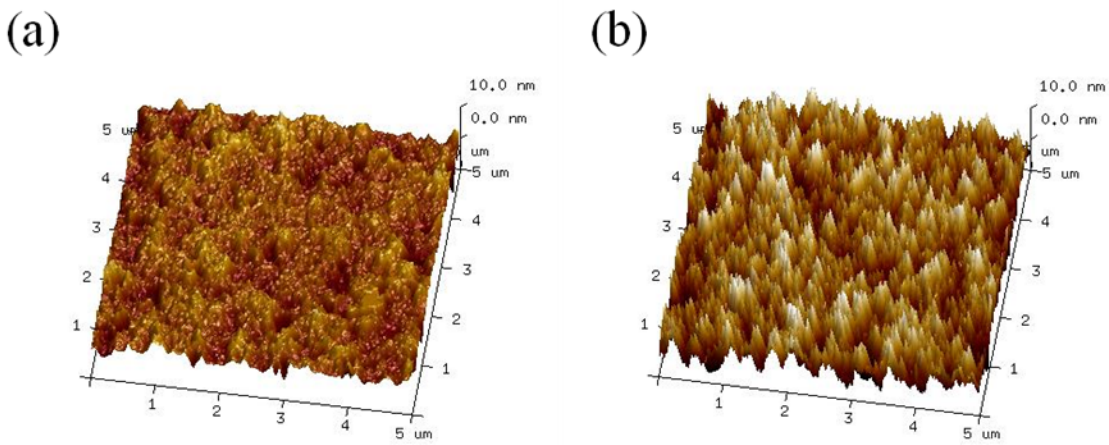

Figure 4.2 Top morphology of PEDOT: PSS films fabricated via (a) spin coating and (b) spray coating.

The conductivity of PEDOT: PSS films prepared by spin and spray coating was also measured to explore whether significant differences existed in their electronic properties. The overall resistance of a thin film material having two Ohmic contacts is given by

$$R = R_c + \frac{L}{\sigma wh} \tag{4.1}$$

Here R_c is the total contact resistance of the two electrodes, L and w are the length and width of the area between the two contacts, h is the thickness of the film and σ is its conductivity. Based on this simple theory, by measuring the resistance of the film with different channel lengths, it is possible to calculate the contact resistance and film conductivity.

To conduct the measurement, the PEDOT: PSS films were spin or spray-coated onto a glass substrate coated with pre-patterned ITO electrodes having four different channel lengths (50 μm, 75 μm, 100 μm and 150 μm), with channel widths fixed at 30 mm. The relationship between total resistance and channel length is plotted in Figure 4.3. Using Equation (4.1), the conductivity of spin and spray coated PEDOT: PSS films was calculated to be 0.0023 S cm^{-1} and 4.45 S cm^{-1} respectively.

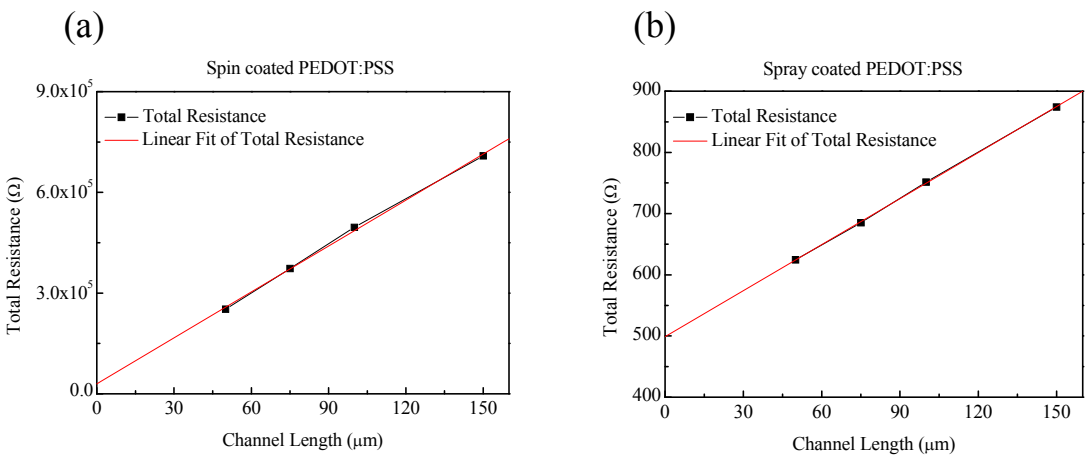

Figure 4.3 The relationship between total resistances and channel length of PEDOT: PSS films deposited by (a) spin and (b) spray coating.

For spray coating solution, IPA and ethylene glycol (EG) was added into the primary water solution in order to tune the wetting property. The increased conductivity of spray cast PEDOT: PSS film (4.45 S cm^{-1} comparing to 0.0023 cm^{-1} for spin coated analogue) was attributed to the use of organic solvent IPA and additive EG. It is well known that organic solvents and process additives can change both the degree of phase-separation between PEDOT and PSS within a PEDOT: PSS film, and increase the molecular orientation of the PEDOT component, leading to an increase in electrical conductivity of several orders of magnitude.[212,213]

4.3 PBDTTT-EFT:$PC_{71}BM$ active layers

The surface morphology of spin and spray coated PBDTTT-EFT:$PC_{71}BM$ films has been investigated using AFM. As shown in Figure 4.4, the result indicates that all the PBDTTT-EFT:$PC_{71}BM$ films had good surface uniformity. It appears that whether the PEDOT: PSS is deposited by spin or spray coating does not have a significant influence on the morphology of PBDTTT-EFT:$PC_{71}BM$ films. The RMS roughness of spray-coated PBDTTT-EFT:$PC_{71}BM$ films was determined to be about 0.5 nm; a value even smaller than the spin coated counterpart, whose RMS roughness was determined to be 1.6 nm. The reduced roughness of spray-coated PBDTTT-EFT:$PC_{71}BM$ films was speculated to result from the low concentration and low viscosity of the solution used for spray coating. We note that the reduced viscosity of such inks is useful for the more rapid formation of a continuous film from individual droplets during spray coating.

It can also be seen in Figure 4.4 that there are no large-scale $PC_{70}BM$ aggregates or domains caused by phase-separation.

It has been shown by other researchers [181] that an increased fraction of PBDTTT-EFT (about 60%) appears at the surface of a PBDTTT-EFT:$PC_{71}BM$ blend film, and that $PC_{71}BM$ aggregation can be suppressed by the presence of DIO. This suggests that the surface morphology observed here does not come from large-scale phase separation between PBDTTT-EFT and $PC_{71}BM$.

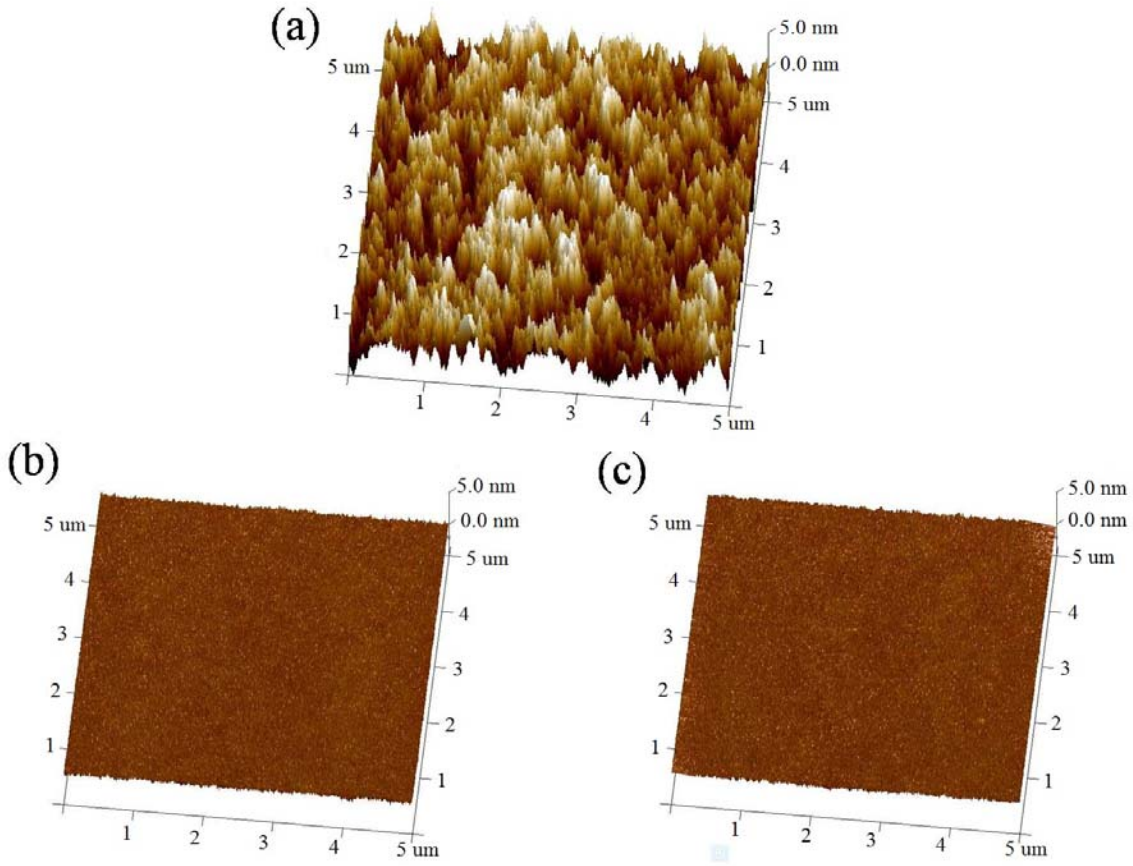

Figure 4.4 AFM surface morphology of (a) spin-coated PBDTTT-EFT:$PC_{71}BM$ on spin-coated PEDOT:PSS. (b) spray-coated PBDTTT-EFT:$PC_{71}BM$ on spin coated PEDOT:PSS and (c) spray-coated PBDTTT-EFT:$PC_{71}BM$ on spray coated PEDOT:PSS.

The UV-vis absorption of spin and spray coated PBDTTT-EFT:$PC_{71}BM$ films were also characterised. As shown in Figure 4.5, the absorption was almost identical for both such films. This indicates that the light harvesting properties of spin and spray cast films are likely to be similar.

Also PBDTTT-EFT:$PC_{71}BM$ films prepared by spin and spray coating have similar thickness; considering the concentration of the solution used for spray coating (5 mg/ml) is much lower than the spin coating solution (30 mg/ml), the spray coating is a cost-effective deposition technique.

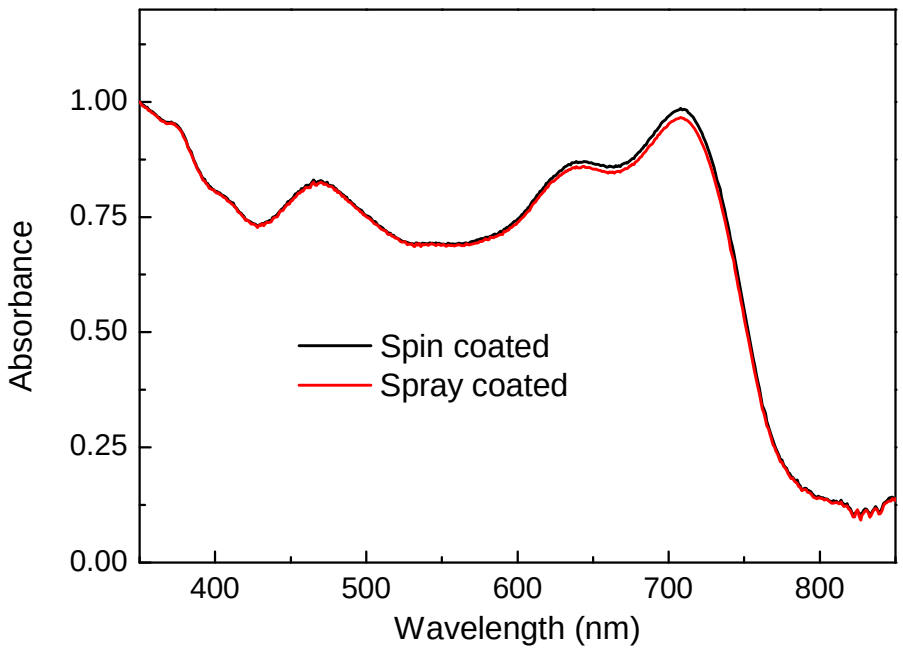

Figure 4.5 Absorption spectra of PBDTTT-EFT:$PC_{70}BM$ films fabricated by spin and spray coating.

4.4 Device performance

The devices were completed by evaporating a cathode composed of 5 nm Ca and 100 nm Al in a thermal evaporator under a pressure of below 5 x 10^{-6} mbar onto the film surface. The devices were then encapsulated using glass slides and UV-cured epoxy glue. A photo of completed arrays of OPV devices is shown in Figure 4.6 (a).

For PV testing, each solar cell pixel on the substrate was measured individually through an aperture mask employed to define the area exposed to the illumination (3.14 mm^2). This also prevented the other 35 pixels being simultaneously exposed. The PCEs of all the 36 individual pixels on the same substrate on which PEDOT: PSS layer was spin coated and the active layer was spray coated are summarised in Table 4.1. A 3D map of this data is also shown in Figure 4.6 (b). Here, we find a maximum PCE of 8.75% for one pixel. The average PCE of all 36 pixels was determined as 7.86%, with standard deviation of 0.60. A histogram of PCEs is presented in Figure 4.6 (c), from which we can see that a quarter of the 36 pixels

have an efficiency between 7.96 and 8.16%. It is also clear from Figure 4.6 (b) that some pixels with lower efficiency are located at the edge of the substrates. This is attributed to the fact that for the large area substrate, spin coating does not create a uniform film, with the film quality at the edges decreasing. As the HTL in this device was spin coated, the efficiency at the edges is somewhat reduced.

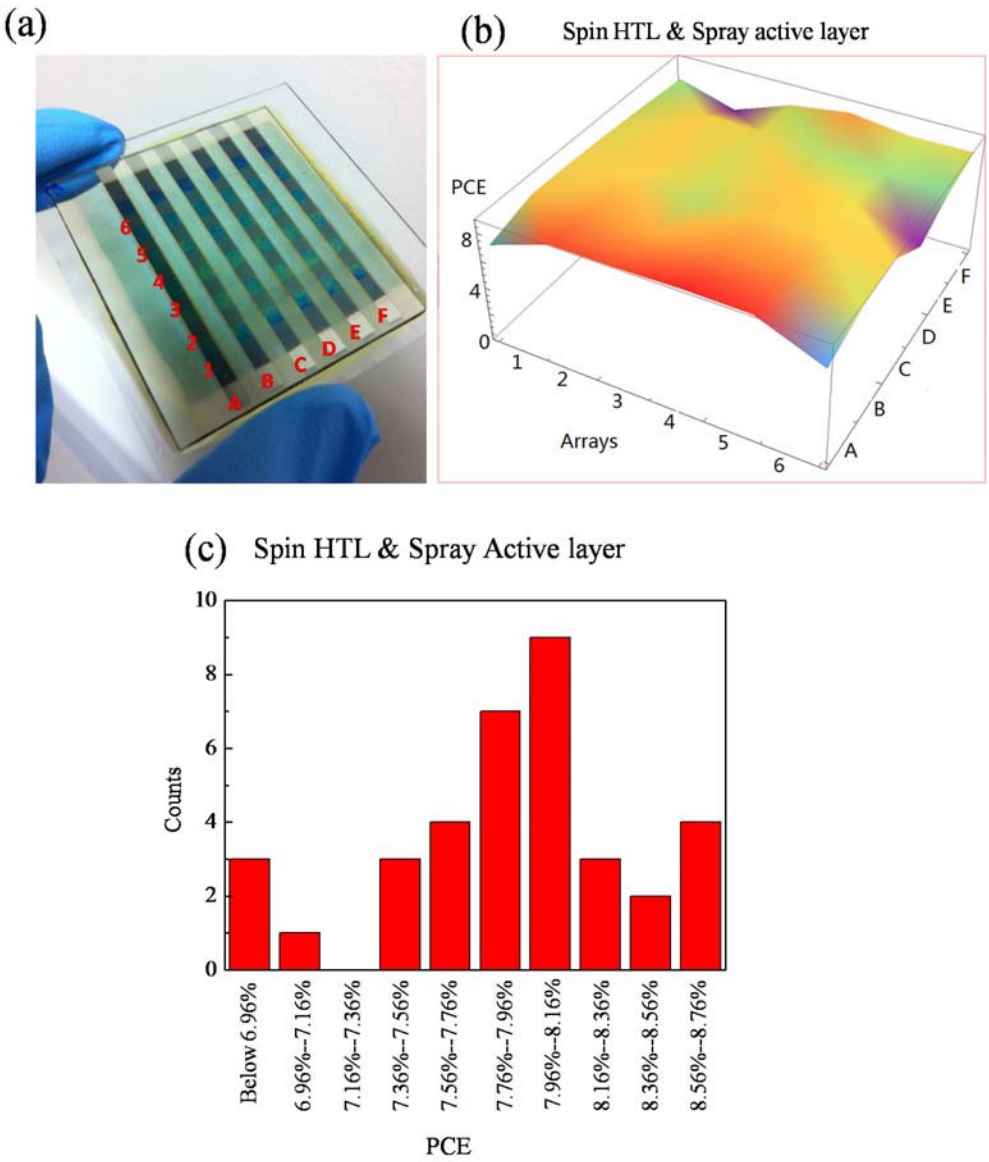

Figure 4.6 (a) Image of an array of organic solar cells. (b) PCEs of pixels whose PEDOT:PSS layer was spin coated and active layer was spray coated. (c) Efficiency distribution for the 36 pixels of the device shown in part (b).

Array number	1	2	3	4	5	6
A	7.06	8.61	8.62	8.75	8.70	6.81
B	8.06	8.32	8.23	8.39	8.41	7.75
C	8.00	8.05	7.63	8.09	8.03	8.04
D	7.89	8.08	7.82	8.10	7.93	6.12
E	7.69	8.03	7.93	7.62	7.49	7.34
F	7.43	6.15	7.70	8.34	7.78	7.86

Table 4.1 PCEs of organic solar cell arrays with a spin coated HTL and a spray coated active layer

Table 4.2 lists the PCEs across the array in which both the PEDOT: PSS layer and active layer were spray coated. A 3D map and statistics are also shown in Figure 4.7. It can be seen that all the pixels are operational. The highest and average efficiency was determined to be 8.06% and 7.50% respectively, with the standard deviation being 0.30.

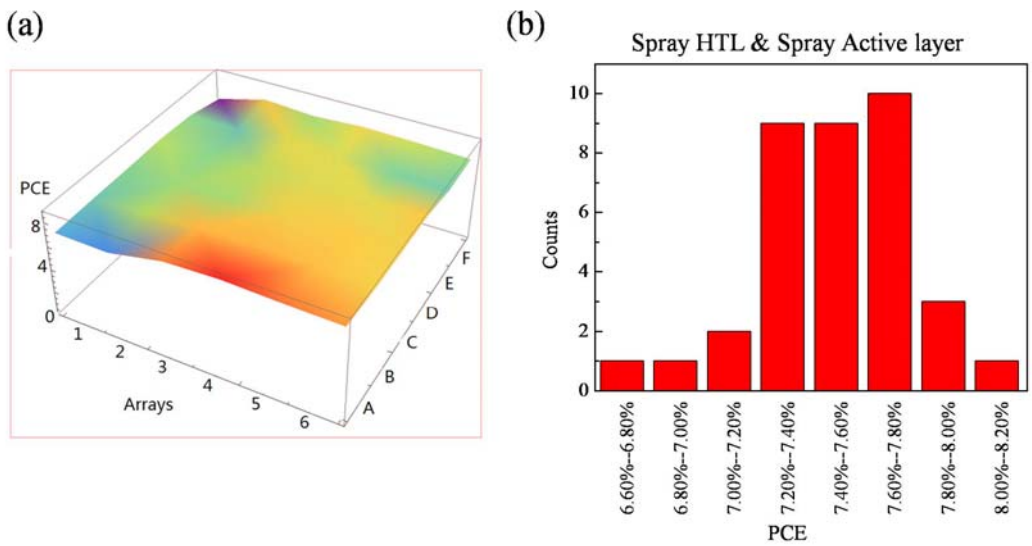

Figure 4.7 (a) 3D map of efficiency on a device with a spray coated PEDOT: PSS and a spray coated active layer. (b) Efficiency distribution of 36 pixels across the device shown in part (a).

Array number	1	2	3	4	5	6
A	7.07	6.98	7.88	8.06	7.91	7.84
B	7.20	7.46	7.74	7.77	7.74	7.65
C	7.29	7.38	7.71	7.65	7.68	7.65
D	7.44	7.31	7.48	7.57	7.59	7.68
E	7.31	7.21	7.59	7.56	7.26	7.22
F	6.63	7.68	7.39	7.61	7.51	7.34

Table 4.2 PCEs of solar cell arrays with a spray coated HTL and active layer

Interestingly, it can be seen in Figure 4.7 (a) that for the all spray-coated devices, the PCE of the edge pixels do not significantly drop as was observed in the device with the spin coated HTL. It is speculated that this is because spray coating a film over a large area results in fewer edge defects. From Figure 4.7 (b) we determined that about 78% of the pixels have efficiency between 7.20 and 7.80%. This range was narrower than devices using a spin coated PEDOT: PSS HTL.

For reference, the devices with both PEDOT: PSS layer and active layer prepared by spin coating were also investigated. Such devices had a peak PCE of 9.35% and average PCE of 9.11% with a standard deviation of 0.11. All of these values are superior to devices prepared using spray coating. It is worth noting however that the substrate used for spin coating is much smaller than the ones used in spray coating.

The JV curves of the pixel with the highest PCE from each type of device are illustrated in Figure 4.8.

The metrics of each type of device are summarised in Table 4.3. Although the standard deviation of devices with both PEDOT: PSS and active layer prepared by spray coating is smaller than devices with a spin coated PEDOT: PSS and a spray coated active layer; the average PCE is lower. This is attributed to PEDOT: PSS prepared with spray coating having a lower resistivity.

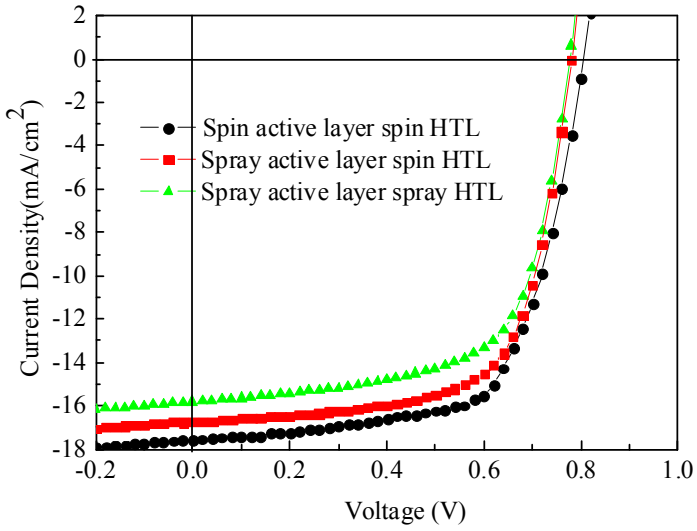

Figure 4.8 JV curves of organic solar cells with different fabrication technique

For a single pixel, high conductivity is beneficial for the extraction of charge carriers. [214,215] However, when we are measuring one of the 36 arrays in our pixelated device arrays, although we only illuminated the array under testing by utilizing an aperture mask, the effective area the holes can travel is larger beyond the illuminated area because of the high lateral conductivity of PEDOT: PSS layer. It is worth to note that the PEDOT:PSS covered the whole substrates while the ITO is patterned to six stripes, as shown in Figure 4.6(a), the crossover of the ITO and metal cathode create a working pixel. Consequently, charge carriers diffused to the region where no ITO layer exists below the HTL won't be collected and the effective device efficiency we measured is lower. This is evidenced by the fact that the short circuit current of OPVs with spray cast active and PEDOT: PSS layer is lower than those with spin cast PEDOT: PSS layer (see Table 4.3). This is also reflected by the series and shunt resistance, the lower shunt resistance for devices with spray coated PEDOT: PSS HTL is speculated to be caused by the pinholes or leakage induced by the high conductive PEDOT: PSS. The series resistance is also related to the design of the ITO pattern and the testing strategy. To clarify this, more work is needed and beyond the scope of current research.

Device type	Spin active layer & spin HTL	Spray active layer & spin HTL	Spray active layer & spray HTL
J_{sc} (mA/cm^2)	17.60 (17.06 ± 0.21)	16.75 (15.68 ± 0.76)	15.83 (15.16 ± 0.29)
V_{oc} (V)	0.81 (0.80 ± 0.01)	0.78 (0.77 ± 0.09)	0.78 (0.77 ± 0.04)
FF (%)	65.61 (65.01 ± 0.53)	66.97 (65.00 ± 2.23)	65.28 (64.29 ± 2.09)
PCE (%)	9.35 (9.11 ± 0.15)	8.75 (7.86 ± 0.60)	8.06 (7.50 ± 0.30)
R_{series}(Ω)	5.01 (5.22 ± 0.11)	3.66 (4. 74± 0.46)	4.48 (4.82± 0.21)
R_{shunt} (Ω)	624 (607 ± 30)	651 (611 ± 60)	628 (600 ± 41)

Table 4.3 Best and average device metrics of solar cells fabricated by different deposition techniques.

To compare device performance with reports from other groups, the hole and electron mobility was determined from single charge carrier device. Here, devices that mainly conduct holes were based on the structure ITO/PEDOT: PSS/PBDTTT-EFT:$PC_{71}BM$/Au. Electron dominate devices were also studied using the structure of ITO/Al/PBDTTT-EFT:$PC_{71}BM$/Ca/Al. According to SCLC theory, the hole and electron mobility can be obtained from the dark JV curve according to the following equation: [69,70]

$$J = \frac{9}{8}\varepsilon_0\varepsilon_r\mu\frac{V^2}{L^3} \tag{4.1}$$

Here the dark JV curve is presented in Figure 4.8. It can be seen the current at low effective voltage is limited by the injection. Only the high voltage region fulfils the space charge limited current theory. Thus in this measurement, we calculate the mobility based on the JV relationship at the voltage region of large than 5 V. Using this approach, the hole and electron mobility was determined as (3.8 ± 0.1) $\times 10^{-4}$ cm^2 V^{-1} s^{-1} and (2.0 ± 0.1) $\times 10^{-4}$ cm^2 V^{-1} s^{-1} respectively. This is at the same level with other reports on this material prepared by spin coating.[216] This result indicates the spray coated PBDTTT-EFT:$PC_{71}BM$ films have similar electrical properties with spin coated ones. And the short-term air exposure during the spray coating is not detrimental to the material.

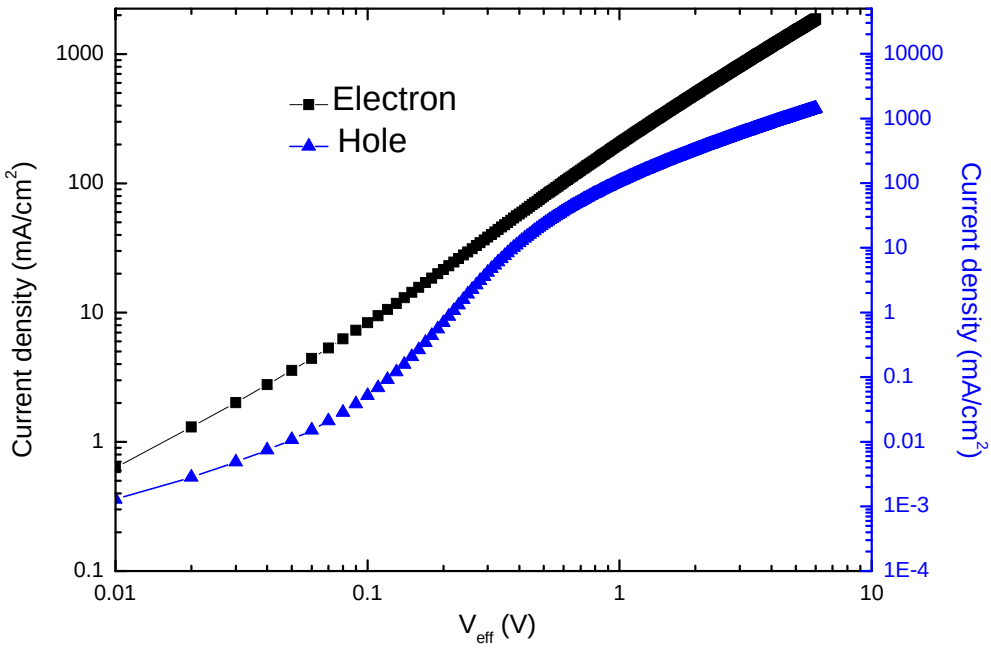

Figure 4.8 JV curves of hole and electron only devices utilising a PBDTTT-EFT:$PC_{71}BM$ active layer.

4.5 Effect of light and air exposure

Although the short-term exposure does not cause significant degradation in the charge mobility, we still speculate the lower PCE of devices spray coated in air result from photo oxidation. [136,217,218] To explore this, device active layers were spin coated onto small area substrates in nitrogen filled glove-box. Before the cathode deposition, the devices were then moved outside the glove-box and exposed to ambient atmosphere under dark or typical laboratory light conditions (white light with a power density of around 5 W/m^2) for different time periods.

The normalised metrics of devices having different exposure times are illustrated in Figure 4.9. It can be seen that the exposure of the active layer to ambient deteriorates the device performance, with the loss of efficiency being dramatically enhanced when the devices are exposed to light and air simultaneously. In particular, exposing the active layer to air in the dark for 30 minutes resulted in the device efficiency dropping to 81% of the unexposed

control. However when the active layer is exposed to light and air simultaneously, the efficiency dropped to 7% of its initial value.

Other work on the BDT based polymer PTB7 concluded that a photochemical reaction involving both light and oxygen is the cause of such degradation. [121,219]

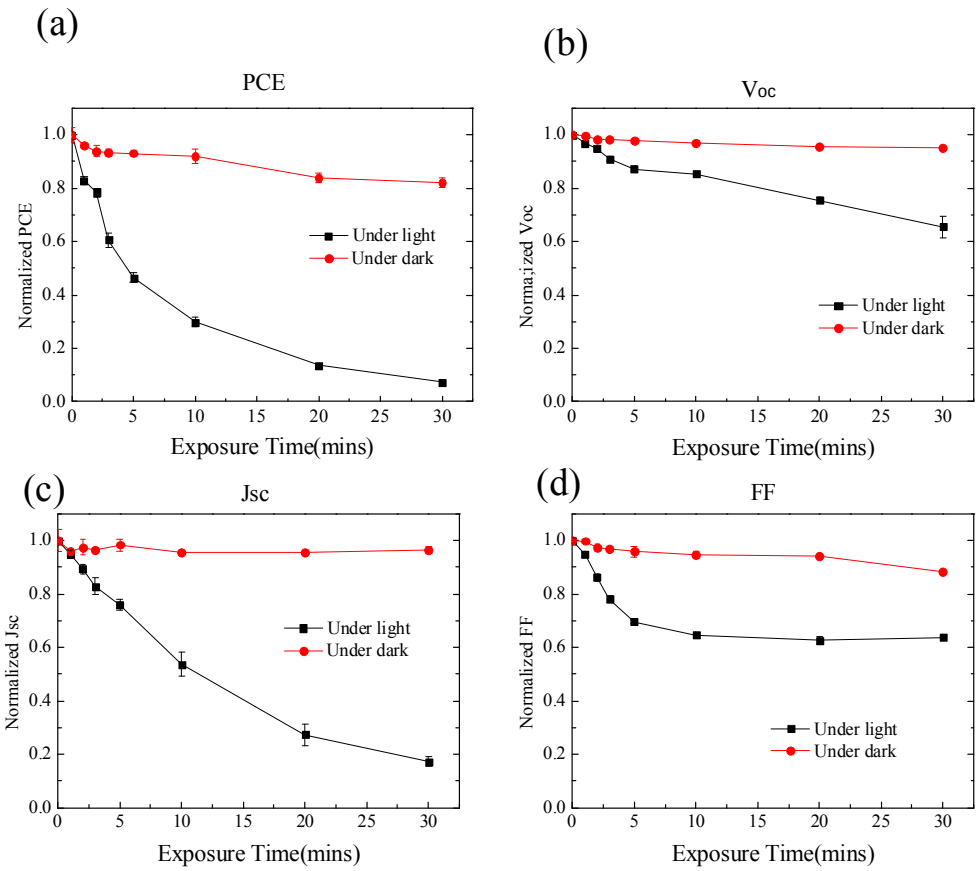

Figure 4.9 Normalised devices metrics following different exposure times.

It can be seen the degradation of PCE mainly comes from the significant drop of J_{sc} and FF. In work by Pearson et al. such degradation was attributed to charge trapping and decreased charge carrier lifetime. [131] We find therefore that PBDTTT-EFT:$PC_{71}BM$ based OPV devices undergo a significant loss in efficiency when exposed to ambient. The extent of this effect can be greatly suppressed by avoiding simultaneously exposing the devices to light. This result is consistent with the study on PTB7 by Kettle et al.[130] They found the degradation of PTB7 is a 2-step process and is particularly susceptible to illumination in the presence of oxygen. And in their study, using XPS, they found it is the alkoxy side chains that are

vulnerable, which is also present in PBDTTT-EFT and the chemical structures of PTB7 and PBDTTT-EFT are quite similar. We attribute the quite degradation of PBDTTT-EFT:$PC_{71}BM$ based OPV devices under simultaneous exposure to air and light to the photo-assisted reaction between oxygen and the alkoxy side chain.

This result indicates that any manufacture process conducted in air based on PBDTTT-EFT:$PC_{71}BM$ requires precise control of ambient light conditions.

4.6 Conclusion

PBDTTT-EFT:$PC_{70}BM$ based organic solar cell arrays were fabricated over large area substrates (5 x 5 cm^2) via spray coating PEDOT: PSS hole transport layer as well as the PBDTTT-EFT:$PC_{70}BM$ active layer in air. OPV devices with the active layer deposited by spray coating (PEDOT: PSS layer spin coated) had a PCE of up to 8.75%; a value comparable with spin coated devices. Solar cells with both spray cast PEDOT: PSS and active layers had a peak PCE of 8.06%.

A small efficiency loss of PCE was observed when devices were processed in air. This originates from photo-oxidation of the BDT based donor polymer. In order to suppress the loss in device efficiency caused by air exposure during spray coating, it is necessary to avoid simultaneously exposing the active layers to air and light. These results confirm that spray coating is a promising approach to facilitate the fabrication of high efficiency organic solar cells over large area substrates under ambient conditions.

Chapter 5 Fabrication of high efficiency organic solar cells based on a highly crystalline polymer via spray coating

5.1 Introduction

In Chapter 4, the fabrication of a donor-acceptor copolymer based organic solar cell via spray coating was introduced. The material system, PBDTTT-EFT:$PC_{71}BM$, is amorphous and does not tend to aggregate in solution. Another high performance polymer, namely PffBT4T-2OD, is high crystalline.

Although the PCE is one of the highest recorded from a single junction OPV device; the processing conditions used to cast a PffBT4T-2OD:$PC_{71}BM$ blend film play a significant role on the degree of polymer aggregation and can thus affect the performance of resultant devices. For this reason, moving thin film fabrication from spin to spray coating presents a number of challenges.

Most high efficiency devices based on PffBT4T-2OD:$PC_{71}BM$ blend films have used an inverted architecture comprising a structure of ITO/ZnO/active layer/Molybdenum oxide (MoOx)/Al. This fact motivated a study of the fabrication of PffBT4T-2OD:$PC_{71}BM$ based inverted OPV devices including a spray cast ZnO ETL. [98,203]

In this chapter, PffBT4T:2OD:$PC_{70}BM$ based bulk heterojunction organic solar cells having both conventional and inverted architectures were fabricated. The PffBT4T:2OD:$PC_{71}BM$ active layer, PEDOT: PSS HTL (for conventional devices) and ZnO ETL (for inverted devices) were all spray coated under ambient conditions. The composition of the PffBT4T:2OD:$PC_{71}BM$ ink was optimised, with devices based on a conventional architecture exhibiting a peak PCE of 8.13%. Those with an inverted structure had a champion efficiency of 8.43%. The work presented here establishes the fabrication of multilayer high efficiency OPV devices based on a highly crystalline polymer material by

spray coating.

5.2 Spin and spray coating ZnO

Spray pyrolysis has been used in fabrication of ZnO, [220,221] here we used another strategy: spray coat a uniform film from a precursor and then transfer the precursor to ZnO by a thermal annealing process. The reason is that spray pyrolysis of ZnO need to spray the solution to preheated substrates at 200-500 ^{o}C. In this case, it is rather difficult to control the thickness and morphology of the resultant film for our spray coater.

Atomic force microscopy was employed to investigate the surface morphology and roughness of spin- and spray coated ZnO films, as shown in Figure 5.1(a) and (b) respectively.

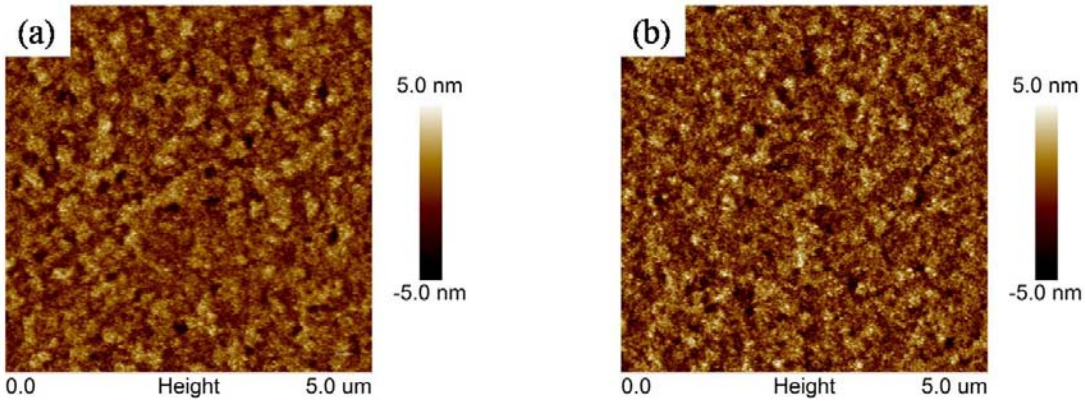

Figure 5.1 Surface morphology of (a) spin- and (b) spray coated ZnO films.

From an analysis of this image, we determine that spin- and spray-cast ZnO have RMS roughness of 1.16 nm and 1.35 nm respectively. It appears therefore the spray-coated ZnO film is slightly rougher than its spin-coated analogue, however previous work has shown that such roughness is not detrimental for OPV device performance. [97]

5.3 Optimising the PffBT4T-2OD:PC_{70}BM solution deposition process

To deposit a PffBT4T-2OD:PC_{71}BM active layer, a 5 mg/ml solution consisting of 1:1.2

weight ratio of PffBT4T-2OD:$PC_{71}BM$ was prepared. It is well known that the choice of solvent is crucial for optimising OPV device efficiency. PffBT4T-2OD has a strong tendency to aggregate in solution, thus it is necessary to heat the solution at 110 °C for a number of hours to ensure a well dissolved solution. It was found a chlorobenzene (CB) solution of PffBT4T-2OD had a very high viscosity, and thus the use of a single solvent does not appear to be ideal in this case. Rather mixing CB with another high boiling point solvent, such as 1, 2-dichlorobenzene (DCB) can be used to reduce solution viscosity. To determine the optimised blend ratio between CB and DCB, four different ratios were tested (CB:DCB = 2:1, 1:1, 1:2, 1:3). All the solvent blends were also mixed with a low (3%) volume concentration of 1, 8-diiodooctane (DIO) in order to optimise the micro nanostructure of the BHJ film. [204,205]

Standard architecture devices incorporating a spin coated PEDOT: PSS HTL were fabricated. The PffBT4T-2OD:$PC_{71}BM$ active layers were spray coated from the four solvent blends in air. The JV curves for devices coated from the different CB: DCB blend solutions are presented in Figure 5.2.

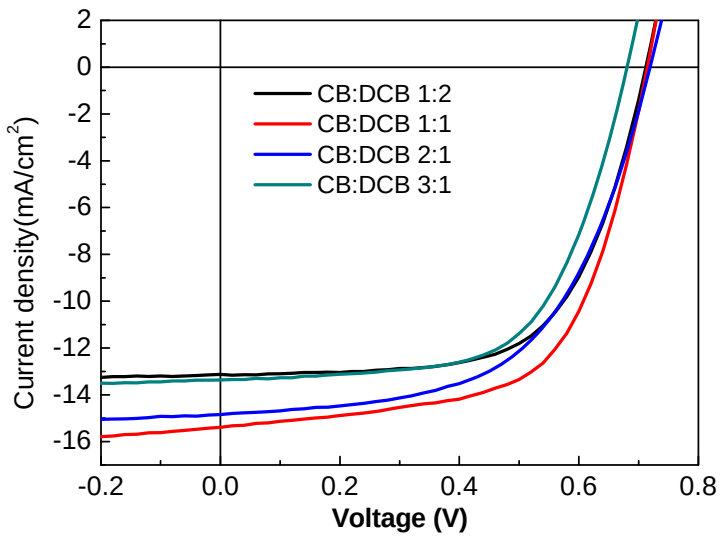

Figure 5.2 JV curves of devices coated from solutions at different CB:DCB blend ratios.

It was found that devices based on active layer cast from a blend ratio of 1:1 CB:DCB exhibited highest efficiency. This solvent blend was therefore used for all device development

reported in this chapter.

5.4 Device fabrication and characterisation

Before use, all the inks were stirred at 110ºC for at least 5 hours to ensure the solids in the blend were fully solubilised. It is worth noting that the relatively low concentration used in the ink for spray-coating effectively suppressed the aggregation problems of PffBT4T-2OD which are commonly encountered in high concentration solutions.

As a control, a PffBT4T-2OD:$PC_{71}BM$ active layer was also spin coated from a similar solution but at higher concentration (20 mg/ml).

AFM images of spin coated and spray coated PffBT4T-2OD:$PC_{71}BM$ blend films are shown in Figure 5.3. It is found that the RMS roughness of spray coated films is slightly greater than that of the spin coated film (7.32 nm compared to 4.65 nm). However, in BHJ OPV devices, the bulk morphology is likely to be of greater importance in determining device efficiency, with the surface morphology playing a secondary role.

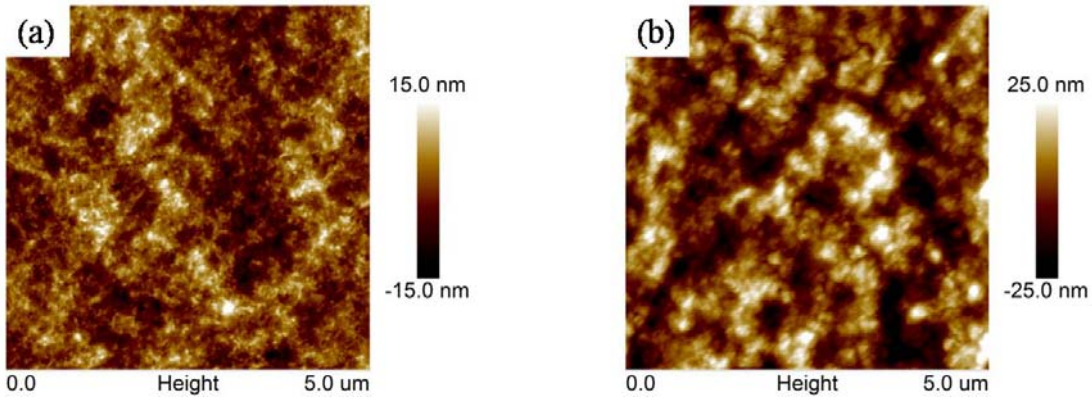

Figure 5.3 Surface morphology of (a) spin- and (b) spray coated PffBT4T-2OD:$PC_{70}BM$ blend films.

The UV-vis absorption of spin/spray coated PffBT4T-2OD:$PC_{71}BM$ films was also characterised. As shown in Figure 5.4, the absorption spectra for both films are almost identical. This indicates a similar degree of crystallinity in both films.

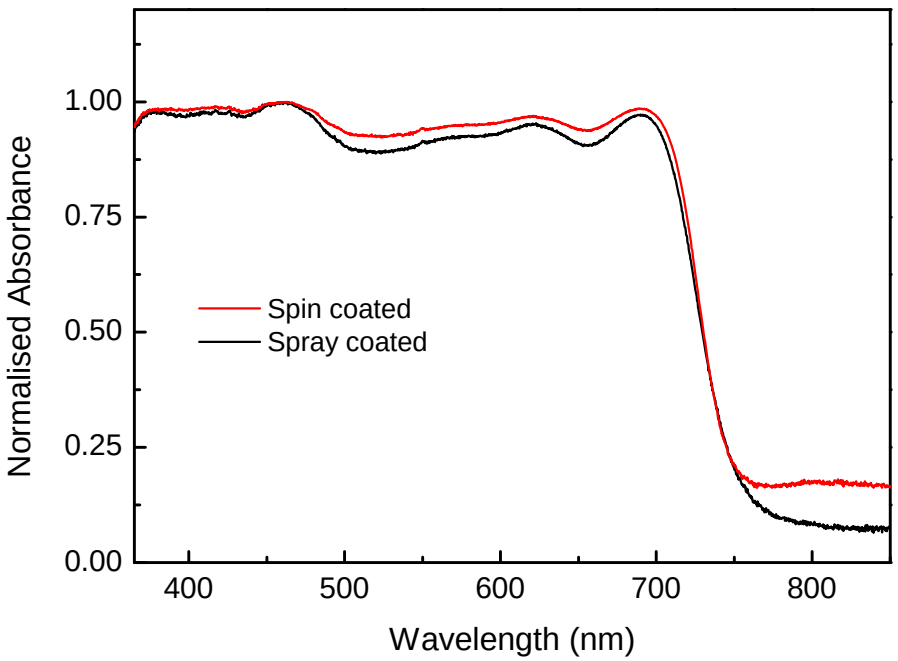

Figure 5.4 Absorption spectra of spin- and spray coated PffBT4T-2OD:PC71BM blend films.

The device performance is summarised Table 5.1. It can be seen the champion conventional devices exhibited an efficiency of 8.13%. For inverted devices, a peak efficiency of 8.43% was reached. For comparison Table 5.1 also includes the device metrics for nominally identical devices in which HTL (or ETL) were spin coated in air, and the active layers were spin coated in a nitrogen-filled glove box. JV curves of champion devices fabricated via spin- and spray coating with conventional and inverted structure are illustrated in Figure 5.5 (a) and (b).

Not surprisingly, the efficiency of the spin-coated devices are higher than equivalent devices in which both HTL (ETL) and active layer deposited by spray coating. Here PCEs of 9.02% and 9.36% were determined for conventional and inverted structure devices respectively.

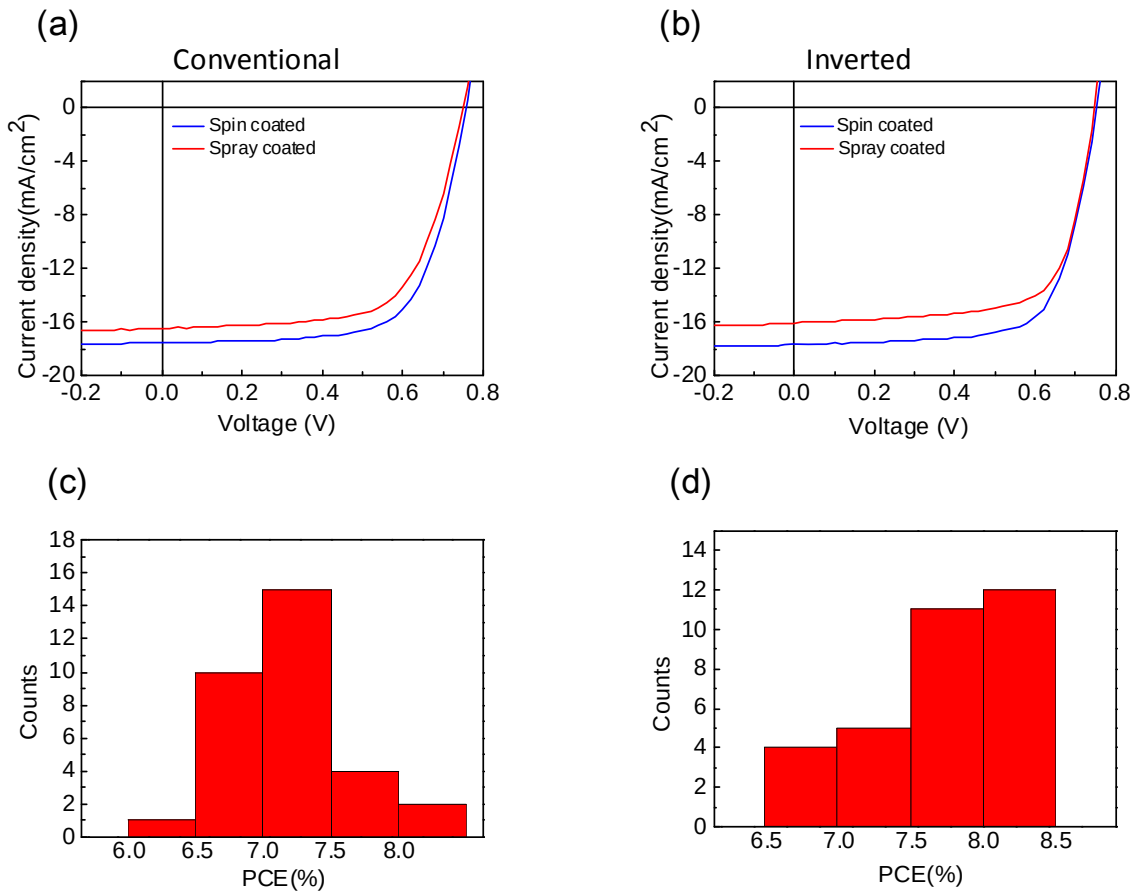

Figure 5.5 Parts (a) and (b) shows J-V curves of champion conventional and inverted devices fabricated by spin- and spray- coating respectively. Parts (c) and (d) show a distribution of device PCE recorded from spray-coated conventional and inverted devices respectively.

The lower efficiency of spray coated devices is primarily caused by a reduction in J_{sc}, which is a direct consequence of photo-oxidation of the active layer as it was exposed to the atmosphere. [10, 11] It is known that some high-performing donor polymers used in organic solar cells are very sensitive to exposure to oxygen in the presence of light, [12] whilst others are apparently significantly more stable. [13] It would be interesting to determine whether such degradation could be limited by performing spray-coating of the active layer in air under appropriate safe-lights or even under nitrogen in a glove box.

To explore the uniformity of the spray coated devices, the distribution of PCE recorded from 32 pixels distributed over 8 different substrates for both conventional and inverted devices are shown in Figures 5.6 (c) and (d). Here, the two edge pixels have been removed

from this analysis, as the film quality at the edge of the substrate always suffers from poor uniformity resulting in poor device performance. This could be avoided by better design of the substrate layout.

It can be seen the uniformity of the spray coated devices is promising. For conventional devices, more than 80% of the pixels have efficiency between 6.5% and 7.5%. The average efficiency of such device is 7.13% with a standard deviation of 0.44. For inverted devices, about 70% of the pixels have an efficiency of 7.5% to 8.5%. The average PCE is 7.75% with a standard deviation of 0.46. Although the spread in efficiency of the spray coated devices with both conventional and inverted devices is slightly larger than the spin coated devices, the observed standard deviation of 0.44 and 0.46 still indicates promising levels of uniformity.

Finally, we note that the area of the substrates used in this work is relatively small. However, our work highlights the possibility to fabricate high performance OPV devices based on highly crystalline polymers via spray coating.

Device	PCE (%)	V_{oc} (V)	J_{sc} (mA/cm^2)	FF (%)
Spin-coated conventional	9.02 (8.70±0.15)	0.76 (0.75±0.01)	-17.55 (-16.88±0.40)	68 (68±1)
Spray-coated conventional	8.13 (7.13±0.44)	0.75 (0.74±0.01)	-16.47 (-14.28±0.91)	66 (67±2)
Spin-coated inverted	9.36 (9.11±0.26)	0.75 (0.75±0.01)	-17.68 (-17.24±0.84)	70 (70±2)
Spray-coated inverted	8.43 (7.75±0.46)	0.75 (0.74±0.01)	-16.08 (-15.64±0.63)	70 (67±2)

Table 5.1 Key metrics for conventional and inverted devices fabricated by spin- and spray-coating.

5.5 Conclusion

We have investigated the performance of conventional OPVs incorporating spray coated

PEDOT: PSS hole transport layer and PffBT4T-2OD:$PC_{71}BM$ photoactive layers. This has been compared with inverted OPVs based on a spray coated ZnO electron transport layer and a PffBT4T-2OD:$PC_{71}BM$ photoactive layer. Critically the photoactive ink is based on the highly crystalline polymer PffBT4T-2OD that can be spray coated from a low concentration, cold solution without obvious problems resulting from aggregation. We determine a PCE of 8.13% for conventional devices and 8.43% for inverted devices using a gentle post deposition thermal annealing process that most likely removes any trapped casting solvent. Our work further demonstrates the feasibility of fabricating high performance OPVs via spray coating.

Chapter 6 The effect of DIO solvent additives and thermal annealing on the micro morphology of PffBT4T-2OD:$PC_{71}BM$ BHJ and OPV device performance

6.1 Introduction

As discussed in Chapter 5, PffBT4T-2OD exhibits high crystallinity and therefore high hole-mobility, and in PffBT4T-2OD:$PC_{71}BM$ blend films, it can form relatively pure polymer domains. It has been reported [7] that in solution, PffBT4T-2OD exhibits strong temperature-dependent aggregation behaviour. Consequently, PffBT4T-2OD based organic solar cells are always spin coated from warm solutions (> 60 ºC). The subsequent aggregation or crystallisation process that occurs during cooling and drying are crucial for optimising the resultant device performance.

It is known that thermal annealing is crucial for improving the efficiency of PffBT4T-2OD:$PC_{71}BM$ based OPV devices. In this chapter, the mechanism by which a DIO solvent additive and thermal annealing increases the efficiency of PffBT4T-2OD/$PC_{71}BM$ based organic solar cells is elucidated. Through techniques including SANS and ellipsometry, it is demonstrated that DIO acts as a plasticiser to assist molecular motion and domain coarsening. In these processes, thermal annealing plays antagonistic roles; it increases molecular mobility due to increased thermal energy, however it simultaneously promotes the evaporation of DIO which consequently decreases molecular mobility. Therefore, the ideal morphology results from a fine balance between these two effects; the evaporation rate of DIO and the rate at which domains coarsen in the plasticized film. We believe that this understanding of the mechanism by which additives improve device efficiency can be used in the development of advanced strategies for additive development.

Neutron reflectivity is also used to study the vertical structure of PffBT4T-2OD/$PC_{71}BM$ blend films. It is shown that solvent additives and thermal annealing have almost no effect on

the vertical morphology of the BHJ films.

6.2 Sample preparation and device fabrication

The OPV devices investigated in this chapter have the standard structure ITO/PEDOT: PSS/Active layer/Ca/Al, this can be referred to Figure 4.1 (left).

The active layers were spin coated using the method described in Chapter 3. Then the post-fabrication treatment was finished by annealing at 100°C for various times (3 minutes, 5 minutes, 10 minutes, 20 minutes and 60 minutes). Un-annealed films were also reserved for reference.

The surface morphology of the annealed and control films was imaged using AFM. It can be seen from Figure 6.1, the surface morphology of all films appears very similar with the root mean square (RMS) roughness in all the cases being about 4.4 nm. However, as mentioned previously the surface morphology is of limited utility to predict device performance.

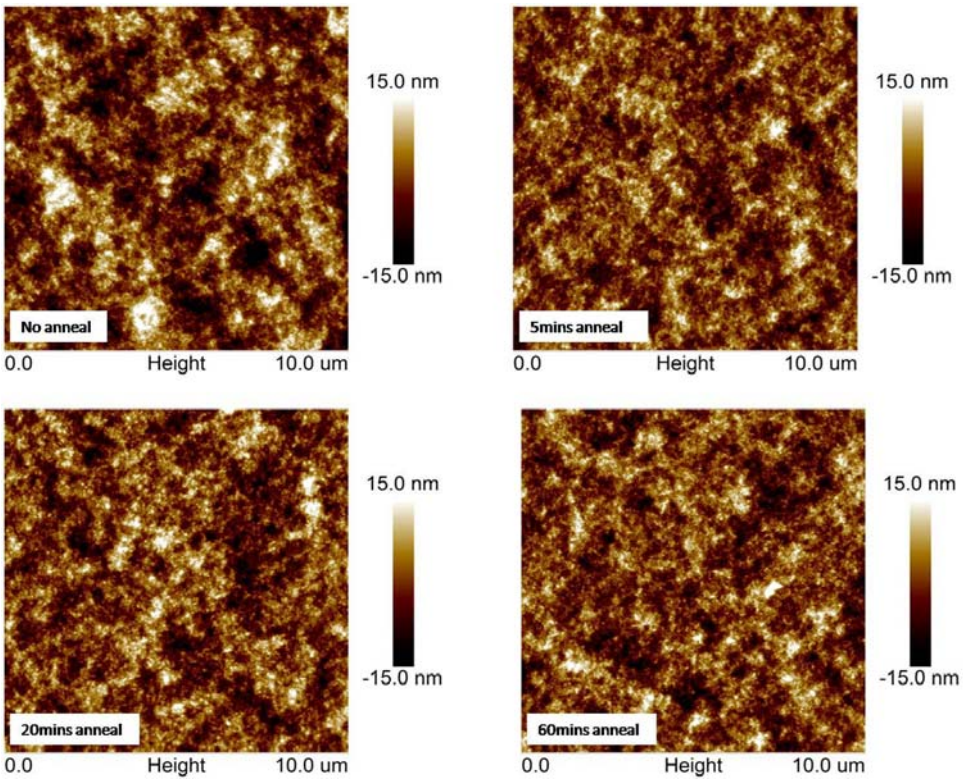

Figure 6.1 AFM images of films with/without different annealing time at 100°C.

The J-V curves of devices processed with DIO and annealed for different times as well as the non-annealed reference device are presented in Figure 6.2 and Table 6.1.

Anneal time	PCE (%)	V_{oc} (V)	FF (%)	J_{sc} (mA/cm^2)
No anneal	7.60 (7.20±0.22)	0.72 (0.72±0.007)	62 (60±2)	-16.94 (-16.53±0.59)
3 minutes	9.02 (8.70±0.15)	0.76 (0.75±0.002)	68 (68±1)	-17.55 (-16.88±0.40)
5 minutes	8.90 (8.73±0.20)	0.75 (0.75±0.002)	68 (68±2)	-17.33 (-17.09±0.30)
10 minutes	8.73 (8.56±0.11)	0.74 (0.75±0.004)	69 (68±1)	-16.99 (-16.83±0.19)
20 minutes	8.95 (8.61±0.23)	0.74 (0.75±0.005)	69 (68±1)	-17.58 (-16.85±0.39)
60 minutes	8.75 (8.40±0.25)	0.75 (0.75±0.002)	68 (67±1)	-17.07 (-16.73±0.31)

Table 6.1. Device metrics showing the peak and (average) values for PCE, Voc, FF and Jsc for devices with 3% DIO and various annealing times.

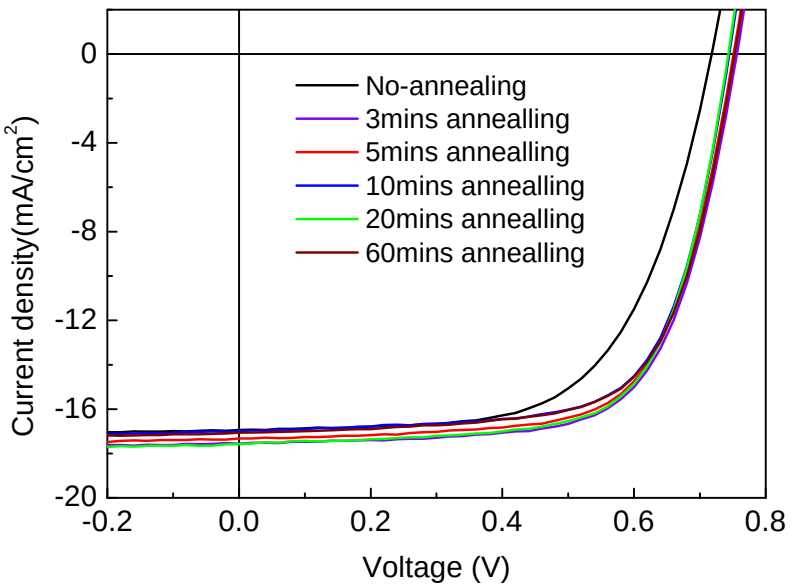

Figure 6.2 JV curves of devices subject to different annealing time at 100 °C before cathode evaporation.

It can be seen that for devices treated with 5 minutes thermal annealing at 100 ºC, the efficiency underwent a relative improvement of about 20%, from 7.20% to 8.73%. The V_{oc} of all annealed devices were quite similar, being 0.75V, while the un-annealed devices V_{oc} was smaller (0.72V). The fill factors of the devices were also improved by the annealing treatment. It was found that the efficiency improvements occurred in the first 3 to 5 minutes of annealing. Further annealing did not prove beneficial in terms of device performance.

To elucidate the effect of DIO on this process, solar cells without DIO in the active layer preparation were also fabricated. The surface morphology of the active layer processed without DIO before and after 5 minutes annealing are presented in Figure 6.3. It is found that the films processed without DIO are flatter, having a RMS roughness of about 3.1nm; a value that compares to 4.4 nm measured for films with 3% DIO additive.

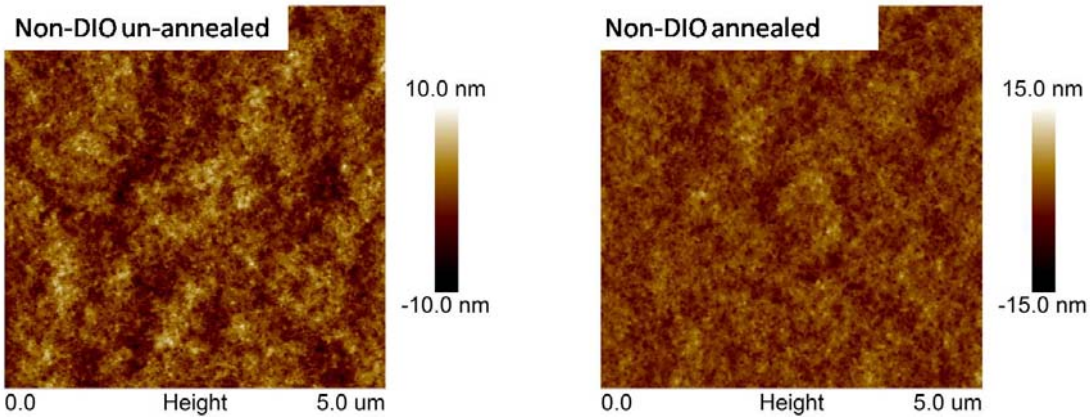

Figure 6.3 Surface morphology of PffBT4T-2OD:PC70BM blend films processed with and without annealing at 100 °C for 5 minutes.

Devices metrics and JV curves of devices with and without annealing are shown in Figure 6.4 and Table 6.2. It can be seen that the annealing treatment also has a positive effect on device efficiency in devices that did not contain DIO. However the relative improvement in PCE was about 12%, a value smaller than for devices processed with the DIO additive.

Anneal time	PCE (%)	V_{oc} (V)	FF (%)	J_{sc} (mA/cm^2)
No anneal	7.29 (7.08±0.20)	0.72 (0.72±0.01)	63 (62±1)	-16.13 (-15.83±0.30)
5 minutes	8.22 (7.95±0.26)	0.76 (0.75±0.01)	69 (68±1)	-15.69 (-15.40±0.30)

Table 6.2. Device metrics showing the peak and (average) values for PCE, V_{oc}, FF and J_{sc} for devices that did not contain DIO, both with and without thermal annealing.

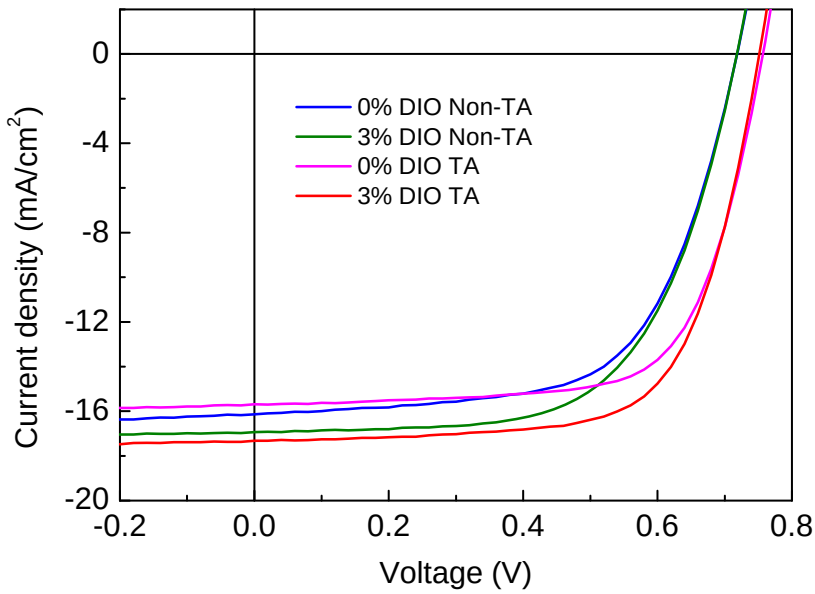

Figure 6.4 JV curves of devices processed with and without DIO, with different anneal conditions applied (non-anneal and thermal anneal at 100 ºC for 5 minutes).

It has been shown that the performance of OPV devices is closely related to the nano-morphology and the hierarchical structure of the BHJ [79,222-226]. To explore the origin of such enhancement, we have conducted a detailed morphological study of these processes using a number of different techniques.

6.3 UV-vis absorption and photoluminescence spectra

The UV-Vis absorption of PffBT4T-2OD:$PC_{70}BM$ blend films processed with DIO before and after annealing were measured as is shown in Figure 6.5. Here all spectra have been normalized to the intensity of the 0-1 transition peak at ~640 nm. It can be seen that the region at ~700 nm corresponding to the 0-0 transition peak remains almost unchanged with thermal annealing which suggests that no significant change in crystallinity has occurred [227].

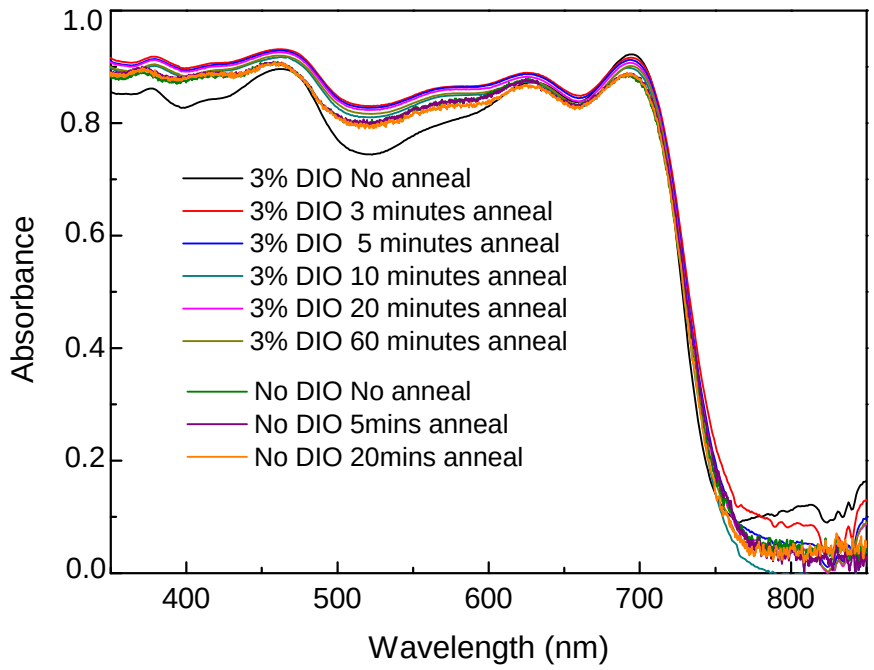

Figure 6.5 UV-vis absorption of PffBT4T-2OD:PC70BM blend films with different fabrication and thermal treatment as indicated.

As discussed in Chapter 2, the optical absorption of a film is correlated with the exciton generation process. In order to investigate the yield of exciton generation, we measured the photoluminescence (PL) spectrum of the different films as shown in Figure 6.6. From 0 to 3 minutes annealing, there is a dramatic increase in PL intensity that remains almost unchanged over the following 3 to 60 minutes annealing time. Theoretically the higher PL intensity corresponds to lower exciton quenching or a lower extent of donor/acceptor material mixing.

In a binary system, reduced mixing can result in the creation of purer or larger single phase domains. Therefore, the PL emission results suggest that annealing makes PffBT4T-2OD or $PC_{70}BM$ domains become purer or larger.

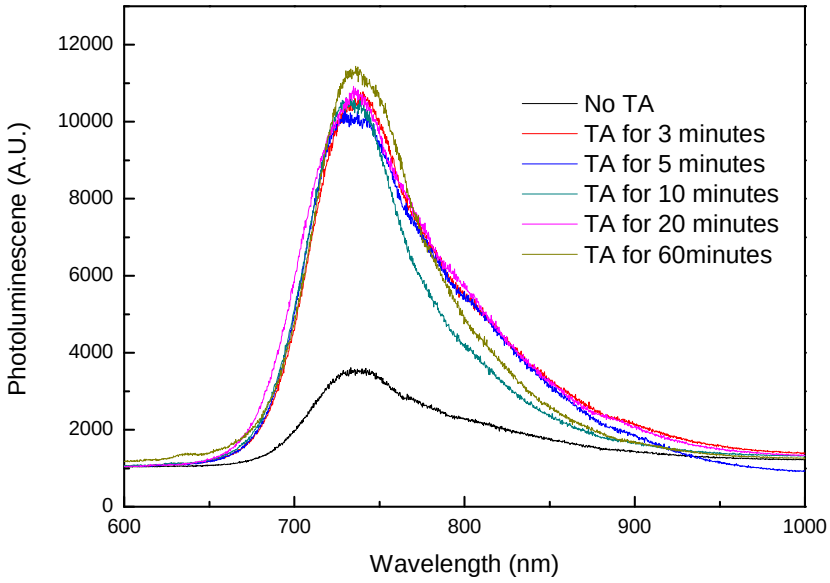

Figure 6.6 PL spectra of PffBT4T-2OD:$PC_{71}BM$ blend films processed with 3% DIO before and after annealing for various times.

6.4 Ellipsometry

Spectroscopic ellipsometry (using a M2000v, J.A. Woollam Co. ellipsometer) was used to determine film thicknesses at room temperature and to measure the drying dynamics of the organic layers (PEDOT: PSS and the PffBT4T-2OD:$PC_{71}BM$) as a function of time during annealing at 100 ºC. We used a Cauchy model to fit Ψ (the ratio of the amplitude of the incident and reflected light beams) and Δ (the ratio of the phase lag of the incident and reflected light beams) over the wavelength range in which films are optically transparent (840 to 1000 nm). For measurements during annealing, thin films were placed on a Linkam heating/cooling stage. The cell had two transparent windows to allow transmission of the polarized incident and reflected ellipsometry beams. The films were rapidly heated from 25ºC

to 100°C and left at 100 ºC for 1 hour, with Ψ and Δ recorded as a function of annealing time. This permitted the evolution in thickness to be followed throughout the annealing process.

The thickness variation with annealing time at 100 ºC was recorded for PffBT4T-2OD:$PC_{71}BM$ blend film processed with or without 3% DIO. This data is presented in Figure 6.7. The inset illustrates the same results after normalising to the final film thickness over the initial 5 minutes. As is shown below, this time period appears crucial for improving device performance.

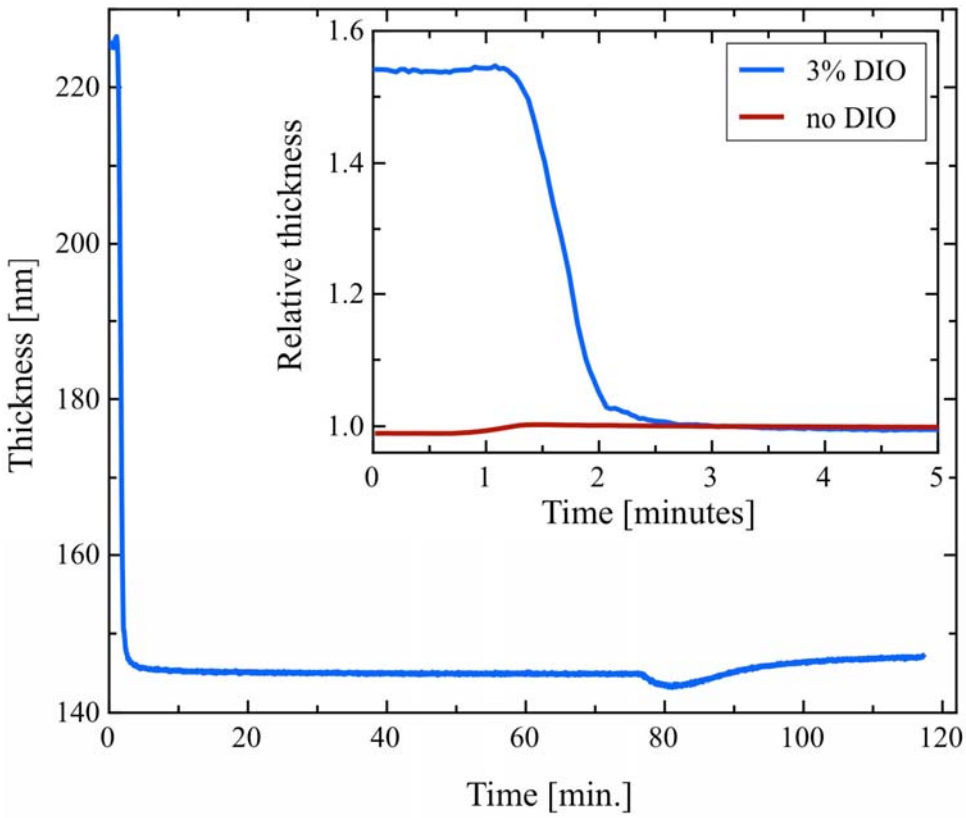

Figure 6.7 Dynamic data recorded during annealing of a PffBT4T-2OD:$PC_{70}BM$ blend film held at 100 ºC. The heating stage was ramped to 100 ºC at time t =1 minute.

The results clearly show that in the case of the film processed with DIO, there is a steep drop of >30% in film thickness during the first 2 minutes of annealing; a process that we attribute to the loss of DIO through evaporation. In contrast, the film that does not contain DIO undergoes a small increase in thickness, which we attribute to thermal expansion. This

indicates that in this film, the CB/DCB casting solvent underwent complete evaporation during spin-coating. Although CB and DCB have boiling points of 131 ºC and 180 ºC respectively, this complete evaporation results from the fact that films were spun-cast from a hot solution (100 ºC) onto substrates that were held at the same temperature. This result is consistent with other studies on P3HT/PCBM BHJ films [228] spun-cast from CB or from 1,2,5-trichlorobenzene (b.p.= 214 ºC) that dry almost completely in a time period shorter than 10s if heated to 50 ºC. We note however that it is possible that a residual fraction of the casting solvent also evaporates during the ellipsometry measurement itself, as measurements are only taken after the sample stage temperature was ramped at 130 ºC/min from RT to 100 ºC.

DIO is a liquid with an extremely low volatility, and thus before thermal annealing, a large fraction of DIO appears to have been trapped in the blend film. Using a simple calculation, it can be found that the weight concentration of DIO in the solution is about 55.2 mg/ml; a value even much higher than the concentration of PffBT4T-2OD:$PC_{71}BM$. Therefore the significant decrease of film thickness observed during the DIO evaporation process is understandable.

The thickness of films during this cooling cycle is presented in Figure 6.8. This allows the glass transition temperature (T_g) to be extracted. [229,230] During the cooling process, the T_g is determined by the temperature at which the thermal expansion coefficient changes. Note that in these measurements, the DIO is completely removed from the film during the initial temperature ramp. It can be seen in Figure 6.10 that the T_g of blend film processed with DIO is slightly higher than the one processed without DIO. Although the linear fitting quality of the experimental curve is high (with adj r-square larger than 0.998); the slight difference of T_g between films processed with or without DIO can still be attributed to the experiment deviation or the error from the fitting process. Admittedly, we cannot exclude the possibility that the films processed with or without DIO comes from different degree of chain stacking; without more experimental evidence, we tend to claim the fitting error is the main cause of the difference.

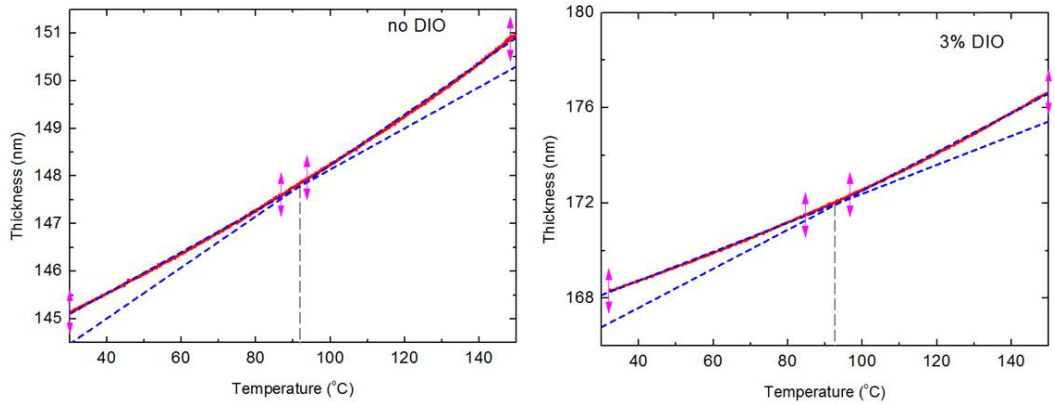

Figure 6.8 Extraction of T_g of the blend film during the film cooling process.

6.5 Neutron Reflectivity

For NR characterisation, thin films (PEDOT: PSS/PffBT4T-2OD:$PC_{70}BM$) were spin-coated on polished 4.0 mm thick 50.0 mm diameter circular silicon wafers (Prolog Semicor, Ukraine) that had been pre-coated with PEDOT: PSS. Neutron reflectivity data was measured at the ISIS neutron spallation source (Oxfordshire, UK) using the INTER instrument, which has a useable incident neutron wavelength range from 1.5 Å – 14 Å. Two angles were collected to cover the required momentum transfer range using incident angles of 0.5º and 2.3º. The recorded NR data (see Figure 6.11(a)) was fitted using the thicknesses measured by ellipsometry as a starting point.

NR data was modelled using the methods of Névot and Croce [231] and the parameter values for the OPV blend layer were allowed to float and converge to a global minimum whilst constant values were used for the PEDOT: PSS layer (thickness, roughness and scattering length density). The fitting was performed by Dr. A. Parnell and Dr. G. Bernardo, University of Sheffield.

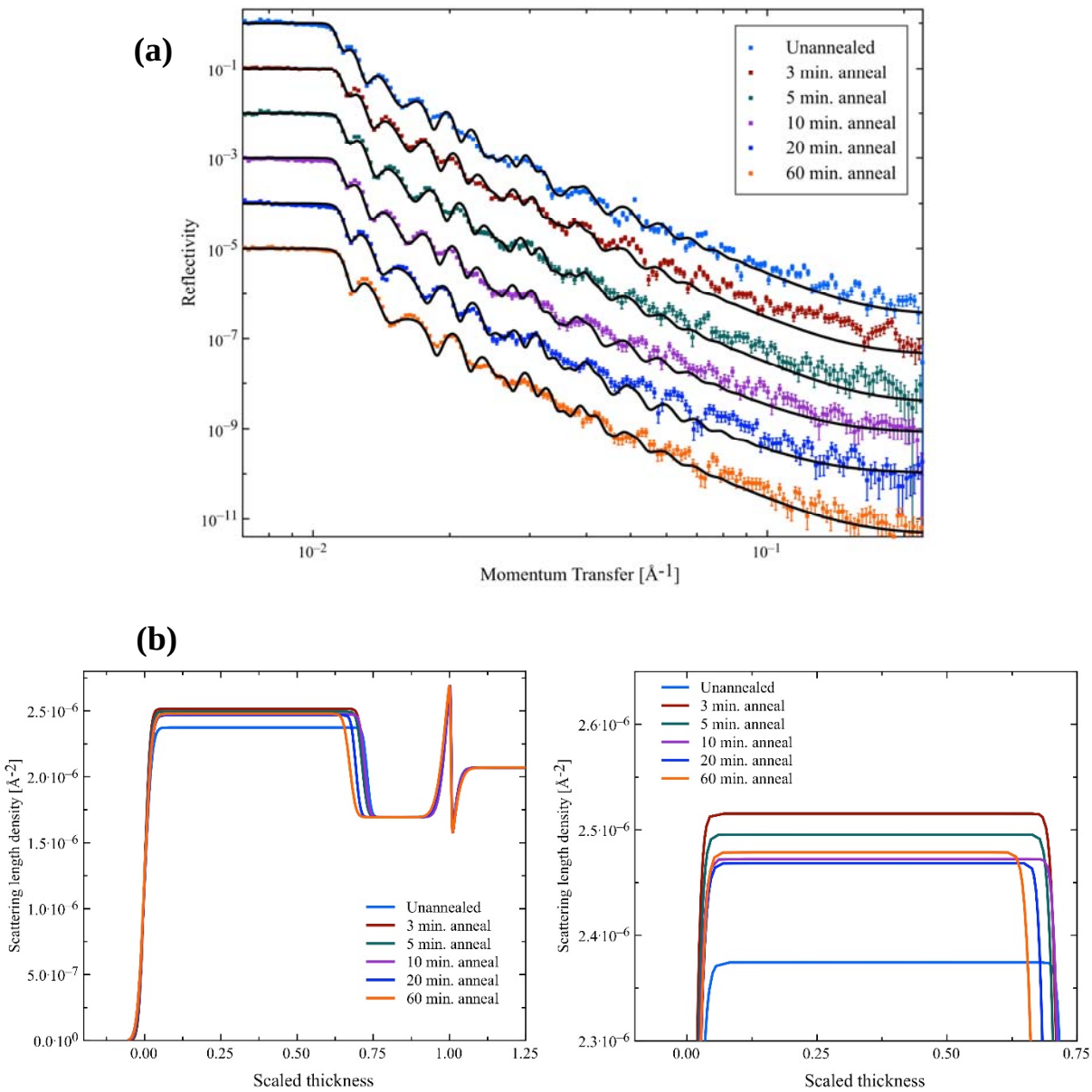

Figure 6.9 NR data (a) and SLD profiles (b) for PffBT4T-2OD:PC70BM blend films with different annealing treatment; the samples are all spin coated on PEDOT: PSS modified silicon wafer. The right figure in part (b) is a zoom-in of the left figure.

As different materials have different scattering length densities (SLD) for incident neutrons, and thus all the samples measured could be fitted assuming three layers (silicon wafer, PEDOT: PSS and PffBT4T-2OD:PC_{70}BM blend). Our measurements indicate there is no change in vertical structure induced by the thermal annealing. The scattering SLD profiles of all the samples are all shown in Figure 6.9 (b).

It can be seen from Figure 6.9 (b) that the effective SLD of un-annealed and 3 minutes' annealed PffBT4T-2OD:$PC_{71}BM$ blends were 2.37×10^{-6} Å^{-2} and 2.52×10^{-6} Å^{-2} respectively. The increase indicates some morphological change within the blends. With further annealing, the SLD reduced slightly, the origin of which is still unclear, nevertheless, the SLD for all the annealed samples was greater than 2.46×10^{-6} Å^{-2}. We believe that the variation among samples with different annealing time can most likely be attributed to the experimental uncertainty.

6.6 Small angle neutron scattering

SANS was employed to investigate the micro morphology of the PffBT4T-2OD:$PC_{71}BM$ blend films. As described in Chapter 3, SANS measurement requires the preparation of samples having a thickness of ~1 μm. This could most easily be achieved by solvent casting the polymer: fullerene blend films [11, 12]. However, the morphology of solvent cast films is usually different from the active layers used in solar cell devices, which tend to be much thinner. Some research has previously explored using SANS to probe polymer: fullerene blend films having a thickness of ~100 nm. An alternate approach is to use a stack of ~10 thin films to increase the SANS signal intensity [9, 10, 14, 35].

SANS measurements were conducted using the LOQ diffractometer from ISIS Pulsed Neutron Source (Oxford, UK). Spectrosil™ slides (Knight Optical WHQ 1500-C) with a radius of 7.5 mm and thickness of 0.5mm were used as substrates. After ultrasonic cleaning in IPA and DI water successively, a 30 nm PEDOT: PSS layer was spin coated. The PffBT4T-2OD:$PC_{71}BM$ films were then spin coated onto the PEDOT: PSS coated substrates. After film drying, thermal annealing was performed for various times. Stacks of 12 films on quartz discs (equivalent to a total active dry layer thickness of ~2.4 μm [12 x 200 nm]), were assembled in order to generate good signal to noise statistics in the SANS signal.

LOQ is a fixed-geometry "white beam" time-of-flight instrument which utilizes a neutron beam modulated at 25 Hz and having a wavelength range between 2 and 10 Å. Data are simultaneously recorded on two, two-dimensional, position-sensitive neutron detectors, to provide a simultaneous measure of scattering over the q-range 0.008−1.6 Å^{-1} ($q = 4\pi/\lambda \sin \theta/2$,

where θ is the scattering angle). Each sample stack and background sample were typically measured for 1 to 2 hours in order to gather data having sufficiently high statistical precision. A background sample was studied consisting of a PEDOT: PSS film. Each raw scattering data set was then radially-averaged, corrected for the detector efficiency, sample transmission and background scattering and then converted to scattering cross-section data and plotted on absolute scale ($\partial\Sigma/\partial\Omega$ vs q) using Mantid software[232]. For convenience, we shall follow the normal convention of referring to $\partial\Sigma/\partial\Omega$ as intensity (I).

In Figure 6.10 we show SANS spectra recorded from a stack of 12 PffBT4T-2OD/$PC_{70}BM$ films on quartz discs with intensity plotted versus scattering vector, for both the annealed and non-annealed samples. In SANS, the intensity is proportional to the number, size and contrast of the scattering entities in a sample, while the q-dependence of the intensity is related to their shape and local arrangement. As can be seen, there is a clear and gradual increase in scattering intensity at small q values after annealing for 5 and 20 minutes. However, samples annealed for 20 and 60 minutes show very similar scattering intensity, suggesting that after 20 minutes the system has evolved to a situation of nearly thermodynamic equilibrium.

Thus the relationship between the intensity and momentum transfer can unveil morphological information within the BHJ films. In the case of PffBT4T-2OD:$PC_{70}BM$ blend films, the polymer and $PC_{70}BM$ have different neutron scattering properties and by fitting the SANS data, we can obtain the domain size of polymer/$PC_{70}BM$ phases. Data analysis was again done by Dr A. Parnell and Dr. G. Bernardo, University of Sheffield. The fitting was done according to models provided by SasView software (Version 3.1.1).

To interpret the data, the Debye-Bueche (DB) [233,234] model was employed which is appropriate for a binary system. According to this model, the intensity can be expressed as:

$$I(q) = \frac{Cl^3}{(1+q^2l^2)^2} + B \qquad C = 8\pi\left(\Delta\rho\right)^2 \phi_1\phi_2 \tag{6.1}$$

where $\Delta\rho$ is a contrast factor that refers to the neutron scattering length density difference between the two compositions within the binary system, ϕ_1 and ϕ_2 are the volume

fractions of each phase, and C is defined as the scattering invariant. B is a background intensity level which can be subtracted and l is the correlation length which can be used to extract the domain size of each phases.

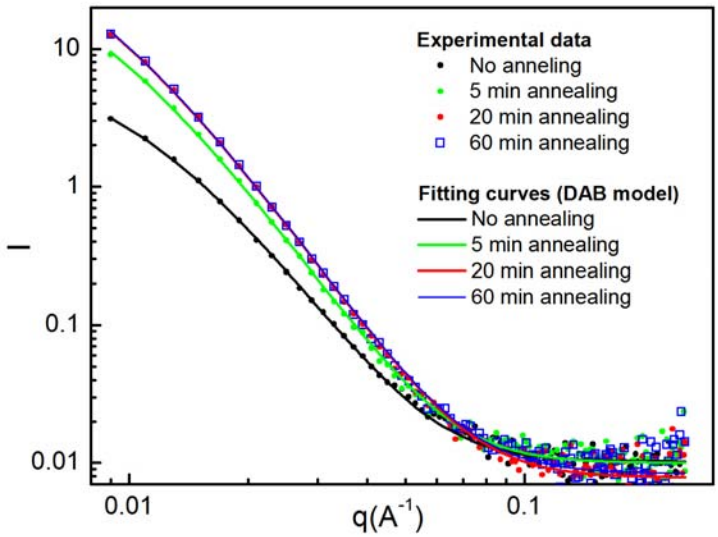

Figure 6.10 Curves of SANS intensity (I) vs scattering vector (q) for PffBT4T-2OD:PC70BM blend films processed with 3% DIO before and after annealing for 5, 20 and 60 minutes.

It can be seen from Figure 6.12 that the data can be well fitted by the DB model. The parameters obtained from the fitting are listed in Table 6.3. For completeness, the fitting parameters for samples processed without DIO are also included in the same table.

For samples processed with 3% DIO, the scattering invariant (C) underwent a large increase after 5 minutes annealing at 100 °C. After longer annealing times, C increased further but to a much lesser extent. In films processed without DIO, annealing induced increase in C, but to a less extent.

From the definition in Equation 6.1, it can be seen that purer domains, which have a larger value of $\Delta\rho$ lead to a larger value of C. We therefore conclude that the increased values of C on thermal annealing correspond to domains within a PffBT4T-2OD:$PC_{71}BM$ films that are purer, with this effect being more significant in films processed with 3% DIO than those

processed without DIO.

The evolution of correlation length presented in Table 6.3 shows very similar trend as the scattering invariant. From the correlation length, the domain size of polymer and fullerene can be calculated through the relationship given by: [235]

$$d_1 = \frac{l}{\phi_2}, \qquad d_2 = \frac{l}{\phi_1} \tag{6.2}$$

Here d_i is the domain size of the two phases. Other parameters have the same meaning as before.

	Sample	Scattering invariant(C) (cm^{-4})	Correlation length (l_i) (Å)	(χ^2/ Npts)	Polymer domain size (d_1) (nm)	Fullerene domain size (d_2) (nm)
With DIO 3 wt%	No-anneal	1.17×10^{-5}	91.3 ± 0.7	0.72	21	16
	5 min anneal	2.44×10^{-5}	129.1 ± 1.0	2.03	30	23
	20 min anneal	3.29×10^{-5}	136.4 ± 0.7	4.62	31	24
	60 min anneal	3.32×10^{-5}	136.9 ± 1.0	3.26	31	24
Without DIO	No-anneal	1.94×10^{-5}	98.4 ± 1.2	0.96	22	18
	5 min anneal	1.98×10^{-5}	97.4 ± 1.1	1.38	22	18

Table 6.3 Scattering invariant (C) and correlation lengths (l) obtained from fitting the experimental data by Debye-Brumberger model.

We can use some simple calculations to calculate domain sizes. In our films, the weight ratio of PffBT4T-2OD and $PC_{70}BM$ was 1:1.2. The fullerene also has a higher density than most polymers (about 50% higher). We therefore calculate a volume fraction of about 0.56 for PffBT4T-2OD (ϕ_1) and 0.44 for $PC_{70}BM$ (ϕ_2). For an un-annealed blend film containing 3% DIO, we extract a polymer domain size of about 21nm. After 5 minutes annealing this domain size coarsens to 30 nm. With further annealing, the domain size further coarsens to 31 nm. For

samples processed without DIO, the domain size remains approximately unchanged on annealing. It is worth to stating that our assumptions are basic, but the magnitude of the polymer domain size is consistent with previous reports [30] and our observations using SEM. Such results are also consistent with the PL measurements; a fact that explains the origin of the improved device performance induced by the addition of 3% DIO and thermal annealing at 100 °C.

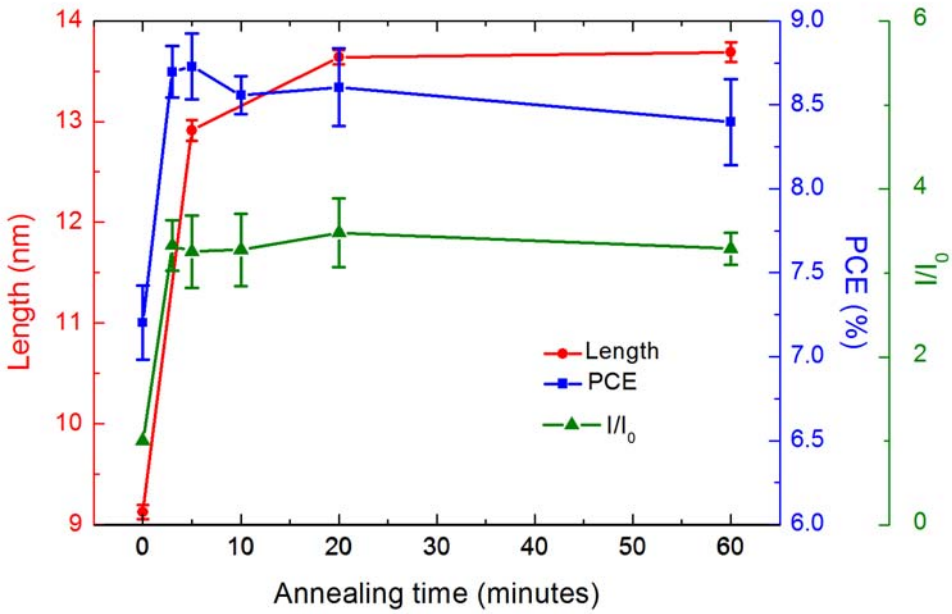

Figure 6.11 Plots of solar cell efficiency, correlation length, the PL intensity ratio between annealed and un-annealed PffBT4T-2OD:PC70BM blend as a function of annealing time for samples processed with 3% DIO.

In Figure 6.11, we plot correlation length, device efficiency and relative photoluminescence intensity for films as a function of annealing time. It can be seen that after 3 minutes annealing the PL intensity increases significantly, a result consistent with the coarsened domain size of polymer/fullerene and purer domains. As the UV-vis absorption was not apparently enhanced by thermal annealing, the improved device performance is likely attributed to more efficient exciton dissociation and charge transport; properties that are assisted by an optimal nano-structure within the PffBT4T-2OD:$PC_{71}BM$ blend.

We link domain size (correlation length) with device efficiency in Figure 6.12. It can be

seen that the highest efficiency is observed in devices processed with 3% DIO subject to 5 minutes annealing. Here the correlation length was in the range of 11.7 – 12.9 nm; a value that corresponds to a domain size about 25 to 30 nm (see Equation 6.2). With further coarsening of the domains, the efficiency decreases slightly.

The trend of device efficiency as a function of the correlation length suggests that both the DIO additive and thermal annealing can combine to create an optimised nano-morphology, resulting in a purer domains and preferred domain size to maximise OPV device efficiency.

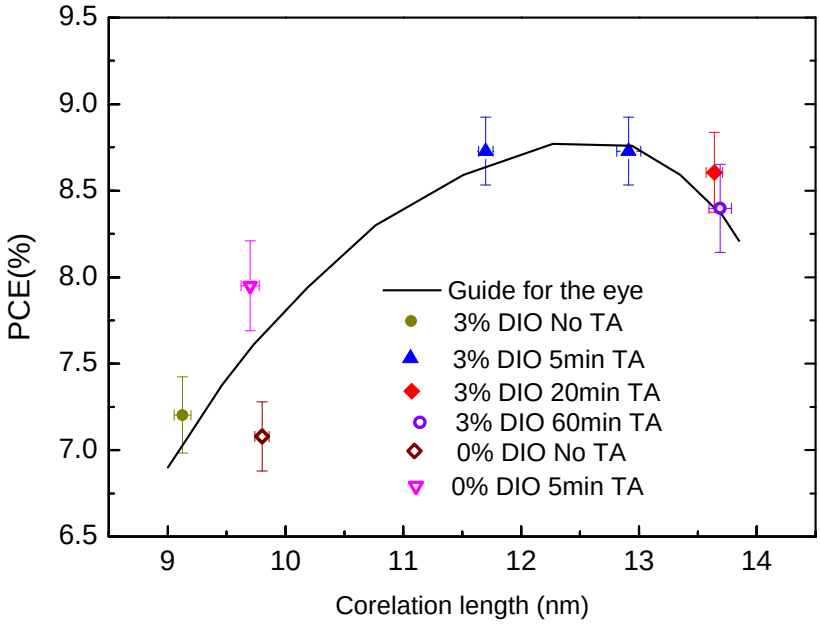

Figure 6.12 Correlation between PCE and correlation length for samples processed with/without DIO and with/without annealing.

6.7 Conclusion

In conclusion therefore, we have explored the morphology of a PffBT4T-2OD/$PC_{70}BM$ OPV applicable blend film during thermal annealing using a variety of optical and structural probes. Neutron reflectivity measurements indicate that the vertical distribution of $PC_{70}BM$ within such films is fairly homogeneous, a feature that is qualitatively different from other

polymer: fullerene blends [192-195]. Importantly, we find that DIO improves the PCE of PffBT4T-2OD:$PC_{71}BM$ OPV devices upon annealing by plasticizing the film. This plasticization enables the coarsening of the nano-morphology of the BHJ during annealing at 100 ºC, with characteristic length scales having an initial value of 9-10 nm reaching a value of 12-13 nm after around 5 minutes. Although further annealing leads to further small increases in characteristic length scale (to ~14 nm) this is apparently detrimental to device PCE.

Our results strongly suggest therefore that there is interplay between the kinetics of domain coarsening and the evaporation of DIO. Indeed, the amount of plasticizer DIO present in the film drops abruptly during annealing due to evaporation, being almost completely removed from the film after the first 3 minutes. On removal of the DIO, the rate of domain coarsening drops abruptly, with the final film phase morphology becoming effectively locked-in; further annealing up to 20 minutes is not proved to be beneficial for the device performance. We believe therefore that the domain size within a polymer: fullerene blend may be controllable through the selection of plasticizers having different evaporation rates, with our results providing a rational framework for the development of improved processing routes for PV-applicable BHJ materials.

Chapter 7 Real world lifetime study of PCDTBT:$PC_{71}BM$ based solar cells for over a year

7.1 Introduction

Polymer poly [N-9'-heptadecanyl-2,7-carbazole-alt-5,5- (4',7'-di-2- thienyl-2',1',3'-benzothiadiazole)] (PCDTBT) is one of the D-A copolymer commonly used as donor material in bulk heterojunction OPVs. [175,236,237] This polymer has been shown to have a high degree of photochemical stability, with recent work under accelerated conditions using a solar simulator suggesting that PCDTBT:$PC_{71}BM$ based OPVs could have an operational lifetime of up to 15 years [238]. Significantly however, such studies have been performed in a well-controlled laboratory; a condition that is very different from the "real-world" in which such devices are eventually expected to operate.

In this chapter, we discuss an extended operational outdoor lifetime study of PCDTBT:$PC_{71}BM$ based OPV devices performed over a period of one year (~8800 hours) with devices located in Sheffield, England. To investigate whether the techniques used to fabricate the devices played a significant role in modifying their operational lifetime, the active organic layer was spin-coated from one of three different solvents/solvent blends; namely chlorobenzene (CB), chloroform (CF) and blend of carbon disulfide (CS_2) and acetone (4:1 volume ratio).

7.2 Testing protocols

Although it has been introduced in Chapter 3, the testing protocols will be discussed briefly here.

The devices explored in this chapter utilised a conventional structure of ITO/PEDOT: PSS/Active layer/Ca/Al (referred to Figure 4.1 left), with each device containing 6 pixels. PEDOT: PSS was employed as the hole transport layer as it has good operational stability when used in PCDTBT:$PC_{71}BM$ based solar cells. [35] Devices were made following the

procedure described in Chapter 3 and encapsulated using UV-cured epoxy and a glass slide. In the measurements described below, 6 devices were characterised (two devices per casting-solvent), with all device substrates housed in the same test-chamber.

Devices were also measured in laboratory using a Newport 92251A-1000 AM 1.5 solar simulator after fabrication and before undergoing the outdoor lifetime testing. Devices fabricated from CF, CB and CS_2/Acetone solutions were found to have initial PCEs of 5.04%, 5.36% and 6.24% respectively. The enhanced efficiency of devices cast from the non-halogenated CS_2/Acetone solvent blend is thought to result from enhanced crystallisation of the $PC_{71}BM$. [207]

Devices were tested using the rooftop lifetime testing system described in detail in Chapter 3. The devices were taken back to laboratory every two months to measure their performance using a solar simulator to confirm the reliability of the real-world lifetime testing setup.

Our experiments commenced on 18th September 2014 (corresponding to early-autumn in England), and ended on 20th September 2015, covering a period of a complete year. Clearly, the exposure conditions experienced by the OPVs are very different from those under an AM1.5 solar simulator in a lab, and thus it was necessary to relate the device performance recorded under fluctuating light levels to that recorded under standard test conditions. To do this, we have linearly normalized the J_{sc} (and thus PCE) determined at each point in time to a value expected for a (AM1.5) light exposure of 1000W/m^2.

However it is well-known that the PCE measured at any one irradiance level cannot be exactly determined on the basis of this normalization process. To confirm this, one of the devices was measured in laboratory under different irradiance (250, 500 or 1000 W/m^2) using an AM1.5 solar simulator. The results of this are shown in Figure 7.2 and Table 7.1. Here a variation in the efficiency of about 7% (between 0.25 sun and 1 sun) was determined after normalising J_{sc} according to different irradiance levels.

To further explore this effect, we grouped out-door device measurements into three data-sets which are dependent on the irradiance level under which they were measured (950 – 1050

W/m^2, 450 – 550 W/m^2 and 200 – 300 W/m^2). The JV curves recorded within each light level were then adjusted using the light intensity recorded by the Si solar-cell, permitting the PCE and J_{sc} to be related to an irradiance level of 1000W/m^2. For each group of light-level measurements, we then compared the PCE, $J_{sc,}$ V_{oc} and FF measurements made throughout the year to data recorded on the first day of the experiment. Following analysis of the data (see Figure 7.3), it was found that the device metrics recorded at the different light levels were very similar and thus we combined this data into a single data-set for each device metric. While this process does not eliminate errors resulting from measurements made at different light levels, it at least permits us to follow the performance of the devices over the year (particularly during the winter months when ambient light levels are much lower).

Irradiance level (W/m^2)	1000	500	250
PCE (%)	5.90	5.73	6.33
Jsc (mA/cm^2)	-10.91	-10.32	-11.49
Voc (V)	0.93	0.93	0.90
FF (%)	58.00	59.64	60.95

Table 7.1 Metrics of a device measured under different irradiance levels in laboratory and then normalised to an irradiance intensity of 1000W/m^2.

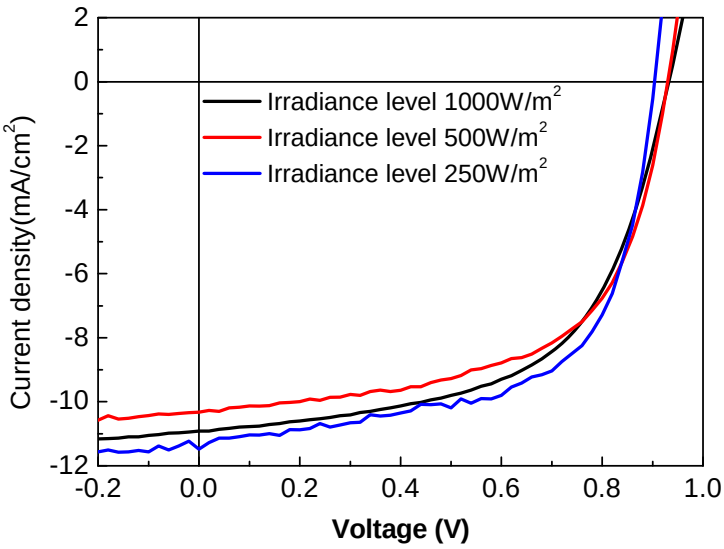

Figure 7.2 J-V curves of devices measured under different irradiance levels in laboratory after normalising to an irradiance intensity of 1000 W/m^2.

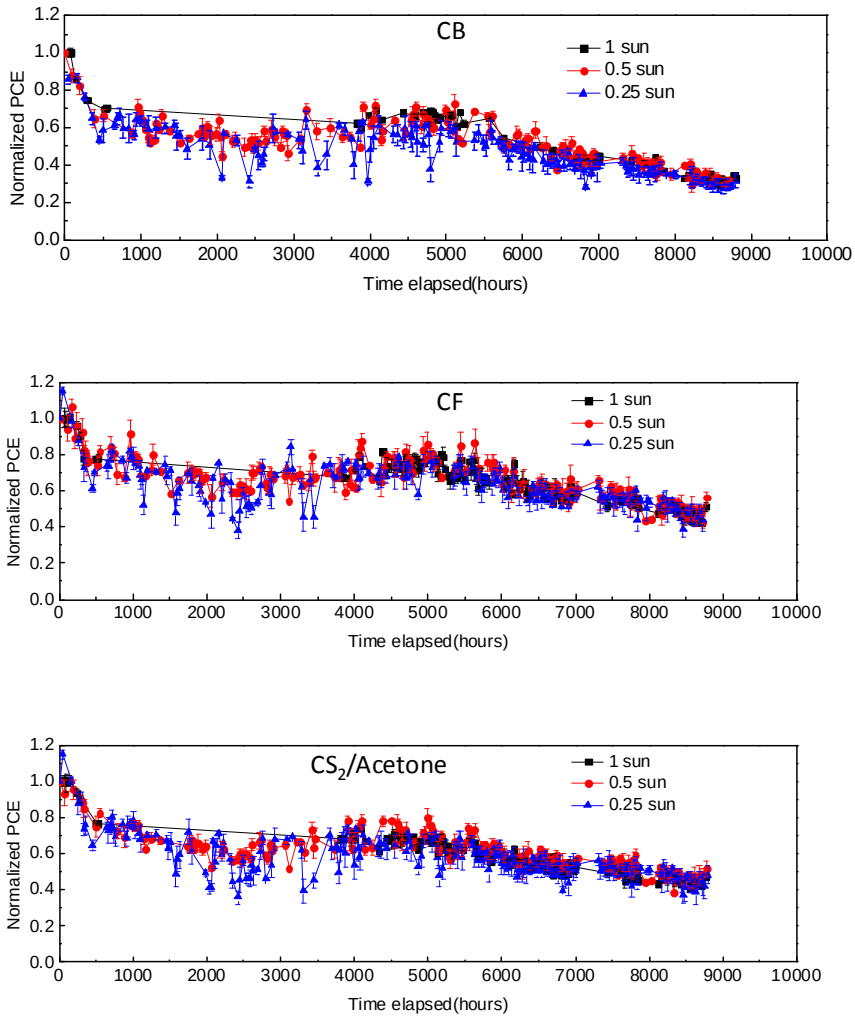

Figure 7.3 Evolution of PCE normalised to different irradiance level as a function of time for organic solar cells processed from different solvents.

7.3 Stability of "edge pixels"

We first discuss data recorded from the edge pixels (Pixels located at the edge of the substrate). The time dependent efficiency of edge pixels is shown in Figure 7.4. It can be seen that such pixels degraded quickly, with the PCE dropping to zero after about 5 days of measurement.

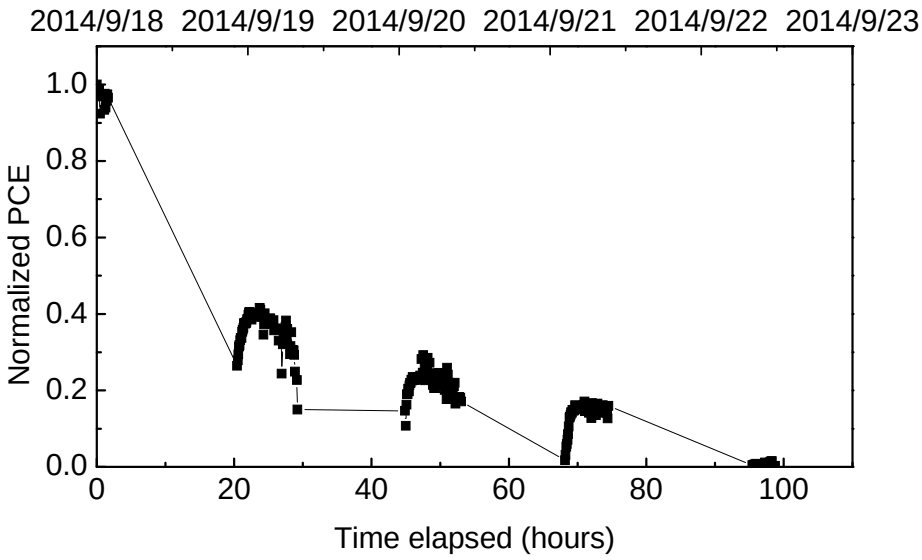

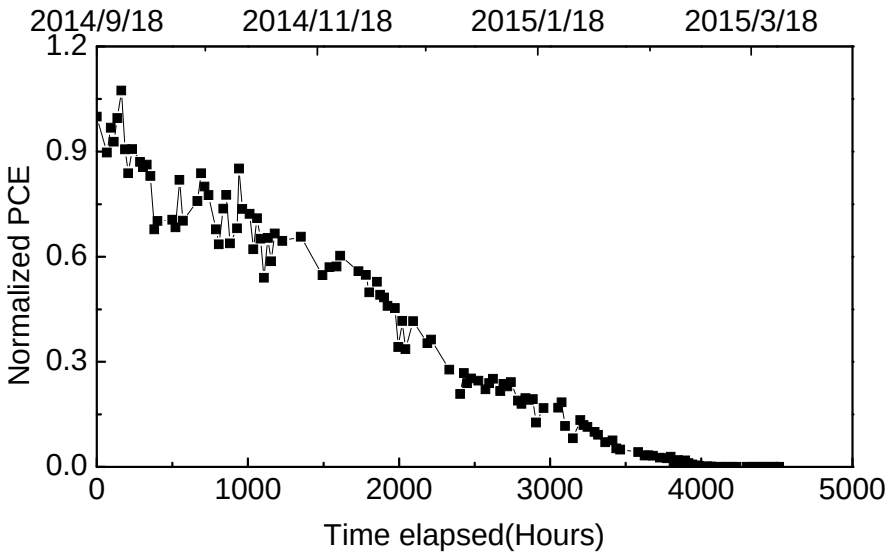

Figure 7.4 Evolution in efficiency of an “edge pixel” (top) and a “sub-edge pixel” (bottom).

The stability of sub-edge pixels (pixels between the “edge pixels” and central pixels) is better, as shown in Figure 7.4 (bottom). Here the efficiency dropped almost linearly for about 3500 hours before it fell to zero. It can be seen that pixels in positions 1, 2, 5 and 6 undergo no obvious burn-in process, with device efficiency dropping in an almost linear fashion. We attribute the rapid degradation of such pixels to the progressive edge-ingress of water and oxygen into the device. (Note that although the devices were housed in a hermetically sealed chamber that was back-filled with nitrogen, we suspect that as the devices were inserted/removed periodically for indoor testing under a solar simulator, water was repeatedly

adsorbed onto the chamber walls and then slowly migrated towards the active pixels.) Indeed, our previous work indicates that the ingress from the edge of an OPV to its centre is facilitated via the presence of the hydroscopic PEDOT: PSS.[36] The importance of sealing the edges of devices has been highlighted in other studies as well. [18] Since pixels 1 and 6 are located at the edge of the device substrate, it is not surprising that these pixels degrade most rapidly. Indeed, after one year, that cathodes of such pixels at the edge of the substrate appear highly degraded (see Figure 7.6). It is also likely that a break-down of the encapsulation contributes to device degradation. Indeed after one year, we find that the colour of the epoxy glue used to fix the cover-slip in place had turned from yellow to yellow-green. As the glass lid of the chamber had > 90% optical transmission for $\lambda > 350$ nm, then exposure of the device to some fraction of the sun's UVA spectrum is likely to result in photo-chemical changes to the epoxy that are anticipated to change its lamination / barrier properties. However, the use of a 400 nm UV filter could presumably minimise this effect.

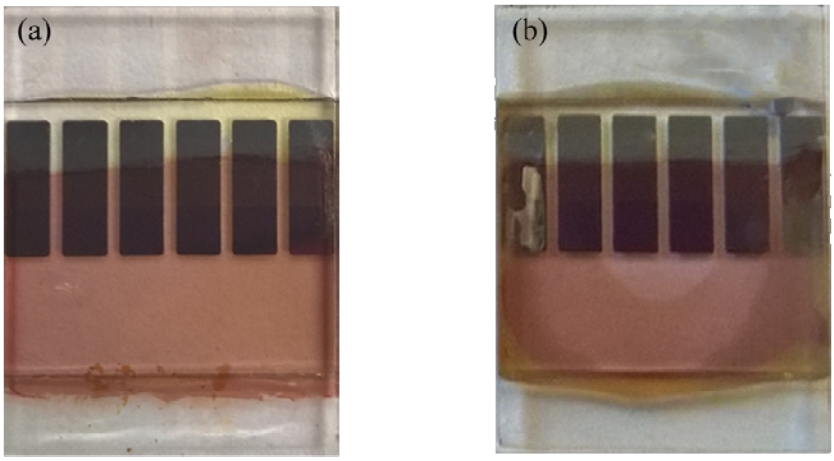

Figure 7.6 Photographs of PCDTBT:$PC_{71}BM$ based solar cells (a) before and (b) after outdoor testing for one year.

7.4 Central pixels

The stability of pixels at the centre of the substrate (pixels 3 and 4) was much better than the edge/sub-edge pixels. The evolution of PCE, J_{sc}, V_{oc} and FF of such pixels are plotted in Figure 7.7. The data for devices processed from different solvents are presented separately. The PCE and J_{sc} are normalised according to the silicon photocell recorded irradiance levels. The device performance recorded indoor under the standard AM1.5 solar simulator is also presented in the same figure. Encouragingly, device metrics recorded in the laboratory and under real-world conditions are in good agreement. This confirms the validity of the normalising method used here.

It can be seen that all the devices undergo a burn-in process during which the V_{oc} and FF degrade rapidly, with the J_{sc} undergoing a relatively smaller reduction. Such phenomena have also been observed when PCDTBT:PC_{71}BM OPVs have been aged under laboratory conditions.[34] This burn-in process has been attributed to light-induced reactions in the active layer that lead to the formation of sub-band gap states. An important feature of the burn-in process is that it appears to stop after a rapid initial loss of performance, suggesting that the reacting species become depleted after sufficient exposure to light. In our previous lifetime study on PCDTBT:PC_{71}BM OPVs carried out in laboratory, we determined a burn-in period of about 60 hours.[35] The burn-in period in the outdoor tests was almost 10 times longer (around 450 hours) – an effect that we ascribe the lower *average* light-flux experienced by the devices operating under real-world conditions (~100 W/m^2 compared to 1000 W/m^2).

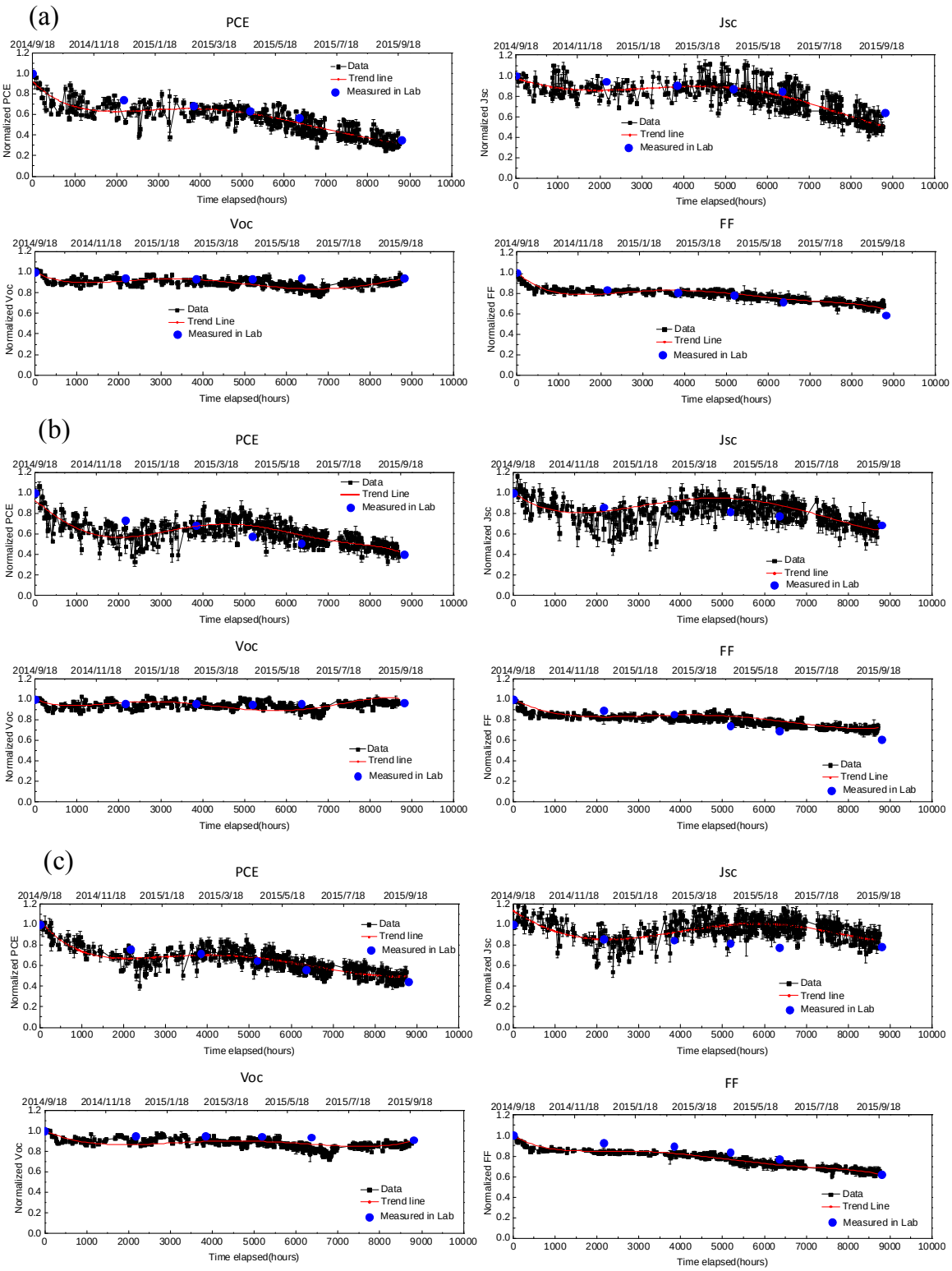

Figure 7.7 Evolution of the normalised device metrics of solar cells with active layer processed from (a) CB, (b) CF and (c) CS_2/Acetone.

To explore whether device stability is dependent on the solvent used to cast the active layer, we tabulate the relative performance of each individual pixel to its initial level in Table 7.2 for the two central pixels of the substrates that were cast from each solvent (equivalent to 4 pixels per solvent-type). We find that the relative changes in the FF and V_{oc} for devices cast from each type of solvent are similar. There is however some spread in the J_{sc} of devices cast from the different solvents, with the greatest reduction in J_{sc} apparently observed in devices cast from CB. We note that the statistical significance of this observation is questionable. However it may suggest that enhanced degradation occurs in devices that are cast from solvents having a higher boiling point. More measurements on a larger number of devices under accelerated aging conditions are needed to confirm such effects.

Solvent	CB		CF		CS_2/acetone	
Relative PCE after 1 year (PCE_{1y}/PCE_0)%	Pixel 1	29%	Pixel 1	31%	Pixel 1	43%
	Pixel 2	31%	Pixel 2	42%	Pixel 2	45%
	Pixel 3	35%	Pixel 3	40%	Pixel 3	42%
	Pixel 4	25%	Pixel 4	45%	Pixel 4	38%
	average	**30±4%**	**average**	**40±6%**	**average**	**42±3%**
Relative J_{sc} after one year (Jsc_{1y}/Jsc_0)%	Pixel 1	61%	Pixel 1	53%	Pixel 1	74%
	Pixel 2	59%	Pixel 2	67%	Pixel 2	79%
	Pixel 3	64%	Pixel 3	69%	Pixel 3	76%
	Pixel 4	47%	Pixel 4	72%	Pixel 4	63%
	average	**58±7%**	**average**	**65±8%**	**average**	**73±7%**
Relative V_{oc} after 1 year (Voc_{1y}/Voc_0)%	Pixel 1	93%	Pixel 1	96%	Pixel 1	91%
	Pixel 2	93%	Pixel 2	97%	Pixel 2	91%
	Pixel 3	94%	Pixel 3	97%	Pixel 3	93%
	Pixel 4	93%	Pixel 4	96%	Pixel 4	94%
	average	**93±0%**	**average**	**96±1%**	**average**	**92±2%**
Relative FF after one year (FF_{1y}/FF_0)%	Pixel 1	51%	Pixel 1	62%	Pixel 1	64%
	Pixel 2	57%	Pixel 2	64%	Pixel 2	62%
	Pixel 3	57%	Pixel 3	61%	Pixel 3	59%
	Pixel 4	58%	Pixel 4	65%	Pixel 4	65%
	average	**56±3%**	**average**	**63±2%**	**average**	**62±3%**

Table 7.2 Statistics of degradation after one year's real-world testing for the two central pixels (3 and 4) from two different substrates.

In Table 2, the parameters are normalised to individual pixels. Here the energy yield should be a meaningful parameter to evaluate the stability of OPV devices processed with different solvents. However the initial efficiency for these devices was different and they were measured subsequently rather than simultaneously; in this case comparing the energy yield cannot predict the device stability. The evolution of PCE clearly results from the combined effects of J_{sc}, V_{oc} and FF, and thus after one year operating under real-world conditions, we find that the PCE of devices cast from CB, CF and CS_2/Acetone have been reduced to (30±4)%, (40±6)%, and (42±3)% of their initial level. As is conventional, we determine the device T_S80 lifetime from the time at which the device efficiency falls to 80% of its initial value at the end of the burn-in process (here starting at 450 hours). Using this approach, we determine T_S80 lifetimes for devices cast from CB, CS_2 /Acetone and CF to be (5200±210), (5700±180) and (6200±270) hours respectively. Our measurements suggest therefore that devices cast from CB have the shortest T_S80 lifetime, although more data is needed on a larger number of devices to explore the statistical significance of this observation.

7.5 Weather information over the testing period

In Figure 7.7, it can be seen that there is an increase of J_{sc} after 2000 hours. We attribute this effect to a seasonal rise in local temperature. To confirm this, we plot the average temperature in the test chamber, the average humidity of the ambient air and the maximum irradiance over the year in Figure 7.9. We emphasise that the temperature sensor was located inside the chamber close to the devices, and this temperature was always higher than that of the ambient air outside the chamber. It can be seen that the chamber temperature closely follows that of the irradiance. Returning to Figure 7.7, it can be seen that J_{sc} undergoes an apparent increase after 2000 hours; a process that closely correlates with this seasonal rise in the average temperature. This indicates a positive relationship between J_{sc} and operational temperature; an observation also made in other studies.[30, 31, 37] The mechanism that underlies this process can be assigned to temperature-dependent charge-carrier transport leading to suppressed electron-hole recombination.

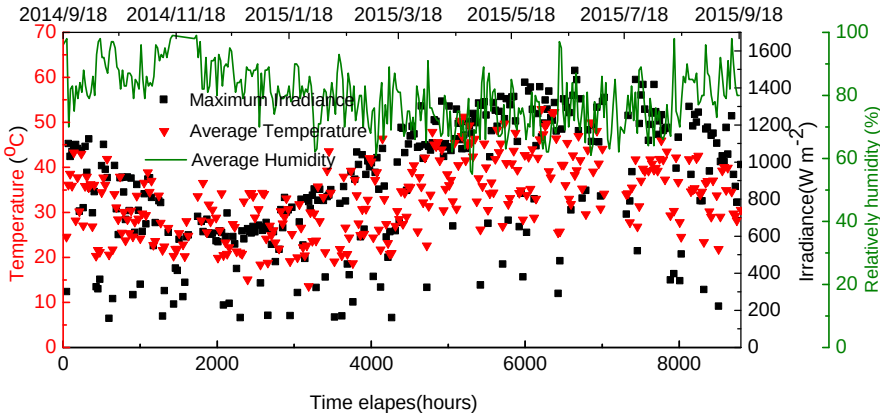

Figure 7.9 Irradiance, temperature in the chamber and ambient humidity recorded over the course of one year.

For completeness, we plot the daily temperature recorded in the chamber over a sunny summer day and a cloudy winter day in Figure 7.10. We find that in summer, the temperature inside the chamber can change at a rate of 10°C/hour, reaching a maximum temperature of 75°C; a process that we believe causes thermally induced stress between the different layers in the device resulting in additional path-ways for the diffusion of oxygen or moisture into the film. More work is required to characterise the nature of the encapsulation seal over time, as we believe improved encapsulation will further extend the lifetime of our devices.

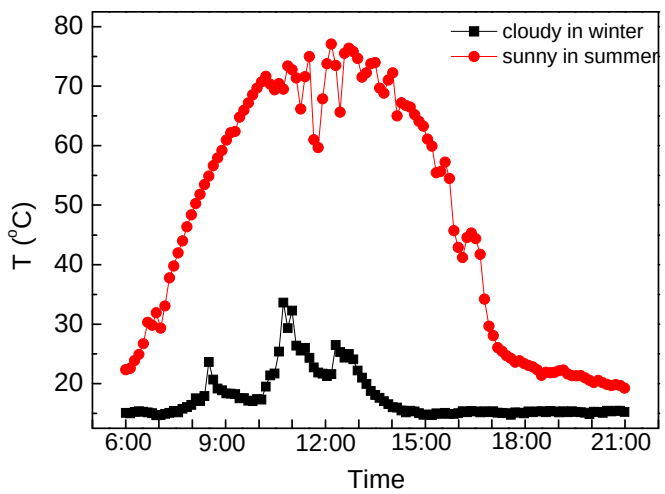

Figure 7.10 Comparison of measured temperature fluctuation on a cloudy winter day and a sunny summer day.

We plot the cumulative energy dose received by the devices tested outdoors as a function of time as shown in Figure 7.8. As it has been mentioned that the burn-in process in real-world condition was about 450 hours, I noticed the accumulative energy dose received after the first 450 hours was approximately 215 MJ/m^2. This corresponds to a period of 60 hours for devices exposed to a constant light intensity of 1000W/m^2, our previous study found in laboratory condition, under constant illumination of 1000W/m^2, the burn-in period for PCDTBT:PC$_{71}$BM based OPV devices was about 65 hours.[144] These results confirm that the length of the burn-in period is directly proportional to the incident light flux.

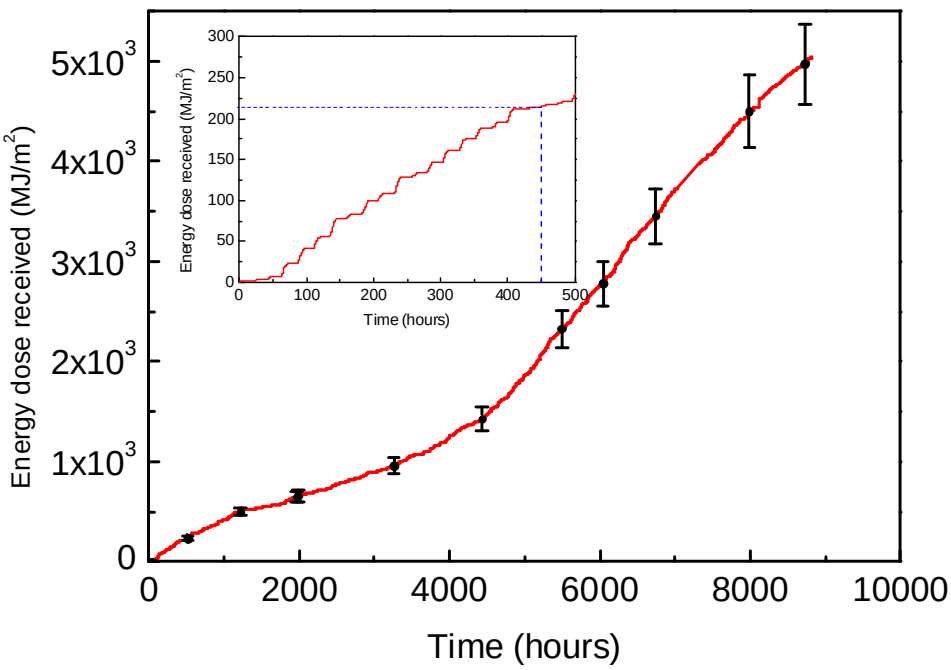

Figure 7.8 Cumulative energy dose received by the devices tested in real-world conditions as a function of time with the zoom in of first 500 hours inserted.

7.6 Measurement in laboratory

Devices were returned to the laboratory to test efficiency under a standard AM1.5 solar simulator every two months. The device metrics recorded are illustrated in Table 7.3 with JV curves presented in Figure 7.11. Data points are also plotted in Figure 7.7.The PCE drop are normalised to each individual pixels respectively.

Solvent	Metrics	2014 0916	2014 1215	2015 0223	2015 0420	2015 0608	2015 0918
CB	PCE (%)	5.36	3.98	3.65	3.41	3.04	1.88
	Jsc (mA/cm^2)	-10.25	-9.65	-9.27	-8.94	-8.65	-6.53
	Voc (V)	0.90	0.85	0.84	0.84	0.85	0.85
	FF (%)	58.14	45.48	46.74	45.51	41.42	34.05
CF	PCE (%)	5.04	3.69	3.46	2.89	2.58	2.03
	Jsc (mA/cm^2)	-10.68	-9.20	-9.01	-8.68	-8.26	-7.34
	Voc (V)	0.86	0.82	0.82	0.81	0.82	0.83
	FF (%)	55.16	48.96	47.00	40.92	38.06	33.41
CS2/Acetone	PCE (%)	6.24	4.74	4.47	4.04	3.48	2.78
	Jsc (mA/cm^2)	-10.51	-9.04	-8.99	-8.61	-8.12	-8.25
	Voc (V)	0.94	0.89	0.89	0.89	0.89	0.86
	FF (%)	63.00	58.59	56.42	52.74	48.55	39.24

Table 7.3 Device metrics measured in the laboratory on different dates.

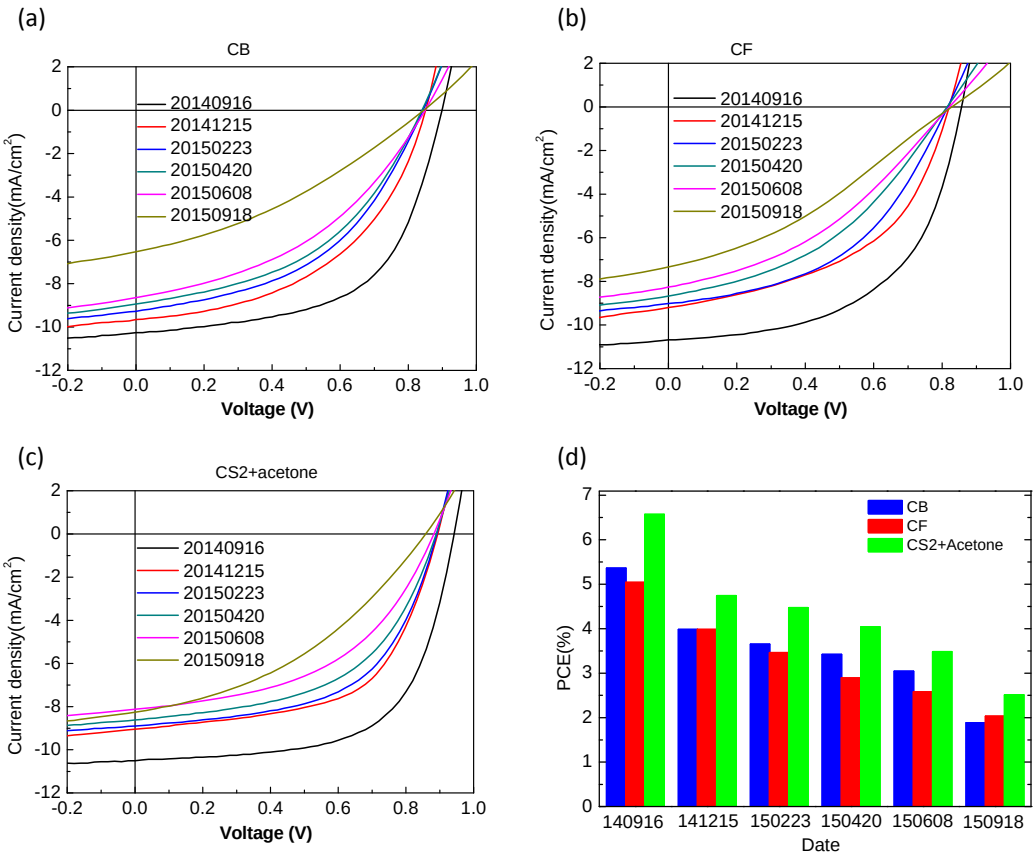

Figure 7.11 J-V curves of devices cast from (a) CB, (b) CF, (c) CS_2/Acetone measured in laboratory and (d) a summary of the efficiency recorded on different dates.

It can be seen that there is a good agreement between the laboratory and real-world performance of devices. This verifies the reliability of the real-world lifetime testing presented in this chapter.

7.7 Conclusion

In summary, PCDTBT:$PC_{71}BM$ based OPV devices were fabricated from three different solvents/solvent blends and encapsulated with epoxy glue and glass slides. Device operation was then tracked in an outdoor laboratory for a period of one year. We find that pixels near the edge of device substrate have reduced stability due to the ingress of water and oxygen through the device layers and through the encapsulation epoxy. Pixels close to the centre of the device substrate have enhanced stability, with T_S80 lifetimes (post burn-in) recorded of up to 6000 hours. Our study shows that the PCDTBT:$PC_{71}BM$ based PSCs have good stability in outdoor conditions over the course of a year, with most significant degradation ascribed to a thermally induced stress in the device (or device encapsulation) rather than significant photo-oxidation of the active layer. We speculate that with more sophisticated encapsulation techniques, together with the use of UV400 filtration may result in significantly enhanced T_S80 lifetimes under real-world operation.

Although the devices processed with CB presented shortest T_s80 lifetime, considering there were only four pixels for each type of devices, we don't want to emphasise the significance of this finding. To illustrate the impact of casting solvent on the device stability, a statistical study must be conducted involving large amount of individual devices. Based on our results, we cannot conclude the null hypothesis or the difference induced by casting solvents.

Chapter 8 Conclusions and Outlook

8.1 Conclusions

Although currently, OPV techniques still cannot challenge the dominance of Si-based PV techniques, as the efficiency is still low and the stability issue is remain need to be solved. But this does not mean we should abort OPV. Its advantage is obvious and some significant improvement has been presented in last decades with the efficiency now improving to above 11% for single junction devices. In order to reduce fabrication cost, different scalable techniques have been developed that are compatible with roll-to-roll fabrication. Research continues to achieve higher device efficiency through the development of materials with improved electronic and morphological properties. Device efficiency can also be optimised by control of the device fabrication process, including solvent engineering and post deposition treatment. As device efficiency has increased, more attention is being focused onto improving device stability. As the real-world is much more complex than a laboratory, evaluating device stability when operating under real-world conditions can unveil essential information.

In this thesis, I have explored three practical aspects regarding OPV devices: (i) innovative and scalable fabrication methods, (ii) strategies to optimise nano-scale morphology and thus device performance, and (iii) the real-world stability of OPV devices tested over prolonged time scale.

In chapter 4, PBDTTT-EFT:$PC_{71}BM$ based OPV arrays were fabricated over large area substrates (5 x 5 cm^2) by spray coating the PEDOT: PSS HTL and/or the PBDTTT-EFT:$PC_{71}BM$ photoactive layers under ambient conditions.

By optimising the fabrication process, I fabricated OPV devices in which the active layer was spray coated (HTL layer spin coated) having PCEs of up to 8.75%. This value is comparable with spin coated devices. For devices with both HTL and active layer spray coated, a maximum PCE of 8.06% was realised. Control measurements determined that a small reduction in device efficiency occurred for devices spray-coated in air. This was found

to originate from photo-oxidation of the donor polymer PBDTTT-EFT. In order to obtain optimum device efficiency, the simultaneous exposure of the active layers to air and light should be minimized. These results confirm that spray coating is a promising approach to facilitate the fabrication of high efficiency organic solar cells over large area substrates under ambient conditions.

In Chapter 5, I investigated the performance of conventional OPVs incorporating a spray coated PEDOT: PSS hole transport layer and PffBT4T-2OD:$PC_{71}BM$ photoactive layers. This was compared with inverted OPVs based on a spray coated ZnO electron transport layer and a PffBT4T-2OD:$PC_{71}BM$ photoactive layer. Critically the photoactive ink was based on the highly crystalline polymer PffBT4T-2OD, and it was shown that this ink could be spray coated from a cold low concentration solution without obvious problems resulting from aggregation. I determined a PCE of 8.13% for conventional devices and 8.43% for inverted devices using a gentle post deposition thermal annealing process which most likely removed any trapped casting solvent. This work further demonstrates the feasibility of fabricating high performance OPVs via spray coating.

In Chapter 6, it was demonstrated that the addition of a 3% by mass DIO solvent additive can improve the efficiency of PffBT4T-2OD:$PC_{71}BM$ based OPV devices. Thermal annealing was also shown to have the same effect on improving the efficiency. However, the mechanisms for these two optimisation strategies are different. DIO plasticises the blend film and affects the nano-morphology within the BHJ films. However thermal annealing for time periods as short as 3 to 5 minutes can increase the purity of polymer/fullerene domains, a property that is beneficial for OPV devices. It was also shown that thermal annealing can assist the removal of residual DIO from the blend films, with the size of polymer/fullerene domains coarsening during this process. Following the removal of residual DIO, further annealing leads to minimal coarsening of the domain size and negative effects on the device performance. These results illustrate that the kinetics of the evaporation of DIO from the blend film control the nano-morphology within a PffBT4T-2OD:$PC_{71}BM$ BHJ. This work contributes to a growing understanding of the mechanism by which different optimisation strategies improve OPV device efficiency based on highly crystalline materials. It will also

help in the design and optimisation of new materials.

In Chapter 7, PCDTBT:$PC_{71}BM$ based OPV devices were fabricated using three different solvents/solvent mixtures and encapsulated using UV-cured epoxy glue and glass slides. Such devices were tested continuously over a period of one year in real-world condition using an outdoor lifetime testing system. It is found that edge pixels on a device substrate exhibited poor stability because of the ingress of oxygen and moisture through the gap between device layers and the encapsulation slides. Central pixels have much better stability, with T_S80 lifetimes of around 6000 hours found for devices processed using low boiling point solvents. More evidence is needed to confirm the effect of solvent choice on the stability performance of PCDTBT:$PC_{71}BM$ based solar cells.

This real-world lifetime study illustrates that PCDTBT:$PC_{71}BM$ based solar cells have good stability in real-world conditions operation over a period of one year. The most significant degradation was ascribed to the thermal stress or failure of the encapsulation rather than the degradation of the photoactive layer. I believe using more sophisticated encapsulation techniques it will be possible to further improve the T_S80 lifetimes of such devices under real-world conditions.

8.2 Outlook and suggested future work

Chapter 4 and 5: Further work can be done to increase the active area of single pixels. It has been shown with the increase of active area, the FF of the device decreases. It would be interesting to investigate to what extent the active area can be increased in devices based on high efficiency polymers. It would also be interesting to fabricate all spray coated devices with the top electrodes spray coated from conductive nanowires.

Chapter 6: More characterisation should be applied to BHJ films such as TEM to accurately determine domain size and compare this to the result of neutron scattering measurements. If this new approach can be shown to accurately characterise and predict micro and nano-morphologies within a polymer: fullerene BHJ, it would be an exciting result.

Chapter 7: The encapsulation process still needs to be improved by replacing the epoxy

and sealing the edge better. The pattern of the substrates can also be optimised through better design with degradation to the edge pixels reduced. The architecture of the device can also be changed; as inverted devices are expected to have better stability. However this has not yet been tested using our method due to limited time being available.

References

1 *BP Statistical Review of World Energy 2015*. (2015).

2 *Global Energy Statistical Yearbook*, 2015. (2015).

3 French, D. 1997 Kyoto Protocol to the 1992 UN framework convention on climate change. *J Environ Law* **10**, 227-239 (1998).

4 Ramachandra, T. V. & Shruthi, B. V. Spatial mapping of renewable energy potential. *Renew Sust Energ Rev* **11**, 1460-1480 (2007).

5 Lunde, P. J. *Solar thermal engineering space heating and hot water systems*. (Wiley, 1980).

6 Mills, D. Advances in solar thermal electricity technology. *Solar Energy* **76**, 19-31 (2004).

7 Green, M. A. *Solar cells operating principles, technology, and system applications*. (Prentice-Hall, 1982).

8 Yogi Goswami, D. Solar Thermal Power Technology: Present Status and Ideas for the Future. *Energy Sources* **20**, 137-145 (1998).

9 *UK energy statistics: 2016 provisional* (2017).

10 http://www.theecoexperts.co.uk/how-much-electricity-does-average-solar-panel-system-generate, (2017).

11 Green, M. A., Emery, K., Hishikawa, Y., Warta, W. & Dunlop, E. D. Solar cell efficiency tables (Version 45). *Progress in Photovoltaics: Research and Applications* **23**, 1-9 (2015).

12 Jackson, P. *et al.* New world record efficiency for Cu(In,Ga)Se2 thin-film solar cells beyond 20%. *Progress in Photovoltaics: Research and Applications* **19**, 894-897 (2011).

13 Britt, J. & Ferekides, C. Thin-film CdS/CdTe solar cell with 15.8% efficiency. *Appl Phys Lett* **62**, 2851-2852 (1993).

14 Carlson, D. E. & Wronski, C. R. Amorphous silicon solar cell. *Appl Phys Lett* **28**, 671-673 (1976).

15 Green, M. A. Third generation photovoltaics: Ultra-high conversion efficiency at low cost. *Progress in Photovoltaics: Research and Applications* **9**, 123-135 (2001).

16 Wei, J. *et al.* Double-Walled Carbon Nanotube Solar Cells. *Nano Lett* **7**, 2317-2321 (2007).

17 Ito, S. *et al.* High-Efficiency Organic-Dye- Sensitized Solar Cells Controlled by Nanocrystalline-TiO2 Electrode Thickness. *Adv Mater* **18**, 1202-1205 (2006).

18 Garnett, E. C., Brongersma, M. L., Cui, Y. & McGehee, M. D. Nanowire Solar Cells. *Annual Review of Materials Research* **41**, 269-295 (2011).

19 Liu, M., Johnston, M. B. & Snaith, H. J. Efficient planar heterojunction perovskite solar cells by vapour deposition. *Nature* **501**, 395-398 (2013).

20 Scharber, M. & Sariciftci, N. Efficiency of Bulk-Heterojunction Organic Solar Cells. *Progress in Polymer Science* **38**, 1929-1940 (2013).

21 Liu, Y. *et al.* Aggregation and morphology control enables multiple cases of high-efficiency polymer solar cells. *Nat Commun* **5**, 395-398 (2014).

22 Darling, S. B. & You, F. The case for organic photovoltaics. *Rsc Adv* **3**, 17633-17648 (2013).

23 Li, S. *et al.* Energy-Level Modulation of Small-Molecule Electron Acceptors to Achieve over 12% Efficiency in Polymer Solar Cells. *Adv Mater* **28**, 9423-9429 (2016).

24 Hook, J. R. & Hall, H. E. *Solid state physics*. 2nd edn, (Wiley, 1991).

25 Brutting, W. *Physics of organic semiconductors*. (Wiley-VCH, 2005).

26 Gueymard, C. A., Myers, D. & Emery, K. Proposed reference irradiance spectra for solar energy systems testing. *Solar Energy* **73**, 443-467 (2002).

27 Shockley, W. & Queisser, H. J. Detailed Balance Limit of Efficiency of p-n Junction Solar Cells. *J Appl Phys* **32**, 510-519 (1961).

28 Rühle, S. Tabulated values of the Shockley–Queisser limit for single junction solar cells. *Solar Energy* **130**, 139-147 (2016).

29 Scharber, M. C. & Sariciftci, N. S. Efficiency of bulk-heterojunction organic solar cells. *Progress in Polymer Science* **38**, 1929-1940 (2013).

30 Scharber, M. C. *et al.* Design Rules for Donors in Bulk-Heterojunction Solar Cells—Towards 10 % Energy-Conversion Efficiency. *Adv Mater* **18**, 789-794 (2006).

31 Koster, L. J. A., Shaheen, S. E. & Hummelen, J. C. Pathways to a New Efficiency Regime for Organic Solar Cells. *Adv Energy Mater* **2**, 1246-1253 (2012).

32 Clarke, T. M. & Durrant, J. R. Charge Photogeneration in Organic Solar Cells. *Chem Rev* **110**, 6736-6767 (2010).

33 Feynman, R. P. (Basic Books,, New York, 2003).

34 Brédas, J.-L., Norton, J. E., Cornil, J. & Coropceanu, V. Molecular Understanding of Organic Solar Cells: The Challenges. *Accounts Chem Res* **42**, 1691-1699 (2009).

35 Yang, C. M. *et al.* Enhanced photovoltaic response of organic solar cell by singlet-to-triplet exciton conversion. *Appl Phys Lett* **90**, (2007).

36 Angel, F. A. & Tang, C. W. Understanding the effect of triplet sensitizers in organic photovoltaic devices. *Org Electron* **30**, 247-252 (2016).

37 Shao, Y. & Yang, Y. Efficient organic heterojunction photovoltaic cells based on triplet materials. *Adv Mater* **17**, 2841-2845 (2005).

38 Snedden, E. W., Monkman, A. P. & Dias, F. B. Kinetic Studies of Geminate Polaron Pair Recombination, Dissociation, and Efficient Triplet Exciton Formation in PC:PCBM Organic Photovoltaic Blends. *J Phys Chem C* **116**, 4390-4398 (2012).

39 Xu, Z. H., Wu, Y. & Hu, B. Dissociation processes of singlet and triplet excitons in organic photovoltaic cells. *Appl Phys Lett* **89**, 131116 (2006).

40 Förster, T. Transfer Mechanisms of Electronic Excitation Energy. *Radiation Research Supplement* **2**, 326-339 (1960).

41 Miyakawa, T. & Dexter, D. L. Phonon Sidebands, Multiphonon Relaxation of Excited States, and Phonon-Assisted Energy Transfer between Ions in Solids. *Phys Rev B* **1**, 2961-2969 (1970).

42 Scully, S. R. & McGehee, M. D. Effects of optical interference and energy transfer on exciton diffusion length measurements in organic semiconductors. *J Appl Phys* **100**, 034907 (2006).

43 Chamberlain, G. A. Organic solar cells: A review. *Sol Cells* **8**, 47-83 (1983).

44 Tang, C. W. 2-Layer Organic Photovoltaic Cell. *Appl Phys Lett* **48**, 183-185 (1986).

45 Hiramoto, M., Fujiwara, H. & Yokoyama, M. p-i-n like behavior in three-layered organic solar cells having a co-deposited interlayer of pigments. *J Appl Phys* **72**, 3781-3787 (1992).

46 Granstrom, M. *et al.* Laminated fabrication of polymeric photovoltaic diodes. *Nature* **395**, 257-260 (1998).

47 Ayzner, A. L., Tassone, C. J., Tolbert, S. H. & Schwartz, B. J. Reappraising the Need for Bulk Heterojunctions in Polymer−Fullerene Photovoltaics: The Role of Carrier Transport in All-Solution-Processed P3HT/PCBM Bilayer Solar Cells. *The Journal of Physical Chemistry C* **113**, 20050-20060 (2009).

48 Layer-by-layer processed high-performance polymer solar cells. *Appl Phys Lett* **101**, 263901 (2012).

49 Chen, D., Liu, F., Wang, C., Nakahara, A. & Russell, T. P. Bulk Heterojunction Photovoltaic Active Layers via Bilayer Interdiffusion. *Nano Lett* **11**, 2071-2078 (2011).

50 Lee, K. H. *et al.* Morphology of All-Solution-Processed "Bilayer" Organic Solar Cells. *Adv Mater* **23**, 766-770 (2011).

51 Vosgueritchian, M., Lipomi, D. J. & Bao, Z. Highly Conductive and Transparent PEDOT: PSS Films with a Fluorosurfactant for Stretchable and Flexible Transparent Electrodes. *Adv Funct Mater* **22**, 421-428 (2012).

52 Hammond, S. R. *et al.* Low-temperature, solution-processed molybdenum oxide hole-collection layer for organic photovoltaics. *J Mater Chem* **22**, 3249-3254 (2012).

53 Betancur, R., Maymó, M., Elias, X., Vuong, L. T. & Martorell, J. Sputtered NiO as electron blocking layer in P3HT:PCBM solar cells fabricated in ambient air. *Sol Energ Mat Sol C* **95**, 735-739 (2011).

54 Steirer, K. X. *et al.* Solution deposited NiO thin-films as hole transport layers in organic photovoltaics. *Org Electron* **11**, 1414-1418 (2010).

55 Zilberberg, K. *et al.* Inverted Organic Solar Cells with Sol–Gel Processed High Work-Function Vanadium Oxide Hole-Extraction Layers. *Adv Funct Mater* **21**, 4776-4783 (2011).

56 Li, S.-S., Tu, K.-H., Lin, C.-C., Chen, C.-W. & Chhowalla, M. Solution-Processable Graphene Oxide as an Efficient Hole Transport Layer in Polymer Solar Cells. *Acs Nano* **4**, 3169-3174 (2010).

57 Kim, J. Y. *et al.* New Architecture for High-Efficiency Polymer Photovoltaic Cells Using Solution-Based Titanium Oxide as an Optical Spacer. *Adv Mater* **18**, 572-576 (2006).

58 Yu, G., Gao, J., Hummelen, J. C., Wudl, F. & Heeger, A. J. Polymer Photovoltaic Cells: Enhanced Efficiencies via a Network of Internal Donor-Acceptor Heterojunctions. *Science* **270**, 1789 (1995).

59 White, MS. *et al.* Inverted bulk-heterojunction organic photovoltaic device using a solution-derived ZnO underlayer. *Appl Phys Lett* **89**, 143517 (2006).

60 Chen, J. D. *et al.* Single-Junction Polymer Solar Cells Exceeding 10% Power Conversion Efficiency. *Adv Mater* **27**, 1035-1041 (2014).

61 Zhang, S. *et al.* Side Chain Selection for Designing Highly Efficient Photovoltaic Polymers with 2D-Conjugated Structure. *Macromolecules* **47**, 4653-4659 (2014).

62 Waldauf, C. *et al.* CHighly efficient inverted organic photovoltaics using solution based titanium oxide as electron selective contact. *Appl Phys Lett* **89**, 233517 (2006).

63 Yan, Y. *et al.* Light-Soaking-Free Inverted Polymer Solar Cells with an Efficiency of 10.5% by Compositional and Surface Modifications to a Low-Temperature-Processed TiO2 Electron-Transport Layer. *Adv Mater* **29**, 1 (2017).

64 Jorgensen, M. *et al.* Stability of Polymer Solar Cells. *Adv Mater* **24**, 580-612 (2012).

65 Norrman, K., Madsen, M. V., Gevorgyan, S. A. & Krebs, F. C. Degradation Patterns in Water and Oxygen of an Inverted Polymer Solar Cell. *J Am Chem Soc* **132**, 16883-16892 (2010).

66 Hertel, D. & Bässler, H. Photoconduction in Amorphous Organic Solids. *Chemphyschem* **9**, 666-688 (2008).

67 Coropceanu, V. *et al.* Charge Transport in Organic Semiconductors. *Chem Rev* **107**, 926-952 (2007).

68 Miller, A. & Abrahams, E. Impurity Conduction at Low Concentrations. *Physical Review* **120**, 745-755 (1960).

69 Gurney, R. W. & Mott, N. F. The Theory of the Photolysis of Silver Bromide and the Photographic Latent Image. *Proceedings of the Royal Society of London A: Mathematical, Physical and Engineering Sciences* **164**, 151-167 (1938).

70 Murgatroyd, P. N. Theory of space-charge-limited current enhanced by Frenkel effect. *Journal of Physics D: Applied Physics* **3**, 151 (1970).

71 Servaites, J. D., Ratner, M. A. & Marks, T. J. Organic solar cells: A new look at traditional models. *Energ Environ Sci* **4**, 4410-4422 (2011).

72 Garcia-Belmonte, G. *et al.* Charge carrier mobility and lifetime of organic bulk heterojunctions analyzed by impedance spectroscopy. *Org Electron* **9**, 847-851 (2008).

73 Perrier, G., de Bettignies, R., Berson, S., Lemaître, N. & Guillerez, S. Impedance spectrometry of optimized standard and inverted P3HT-PCBM organic solar cells. *Sol Energ Mat Sol C* **101**, 210-216 (2012).

74 Kavasoglu, N., Sertap Kavasoglu, A., Birgi, O. & Oktik, S. Intensity modulated short circuit current spectroscopy for solar cells. *Sol Energ Mat Sol C* **95**, 727-730 (2011).

75 Adhitya, K., Alsulami, A., Buckley, A., Tozer, R. C. & Grell, M. Intensity-Modulated Spectroscopy on Loaded Organic Photovoltaic Cells. *Ieee J Photovolt* **5**, 1414-1421 (2015).

76 Cowan, S. R., Roy, A. & Heeger, A. J. Recombination in polymer-fullerene bulk heterojunction solar cells. *Phys Rev B* **82**, 245207 (2010).

77 Rand, B. P., Burk, D. P. & Forrest, S. R. Offset energies at organic semiconductor heterojunctions and their influence on the open-circuit voltage of thin-film solar cells. *Phys Rev B* **75**, 115327 (2007).

78 Riedel, I. *et al.* Effect of Temperature and Illumination on the Electrical Characteristics of Polymer–Fullerene Bulk-Heterojunction Solar Cells. *Adv Funct Mater* **14**, 38-44 (2004).

79 Qi, B. & Wang, J. Open-circuit voltage in organic solar cells. *J Mater Chem* **22**, 24315-24325 (2012).

80 Mihailetchi, V. D., Xie, H. X., de Boer, B., Koster, L. J. A. & Blom, P. W. M. Charge Transport and Photocurrent Generation in Poly(3-hexylthiophene): Methanofullerene Bulk-Heterojunction Solar Cells. *Adv Funct Mater* **16**, 699-708 (2006).

81 Marsh, R. A., Hodgkiss, J. M. & Friend, R. H. Direct Measurement of Electric Field-Assisted Charge Separation in Polymer:Fullerene Photovoltaic Diodes. *Adv Mater* **22**, 3672-3676 (2010).

82 Blom, P. W. M., Mihailetchi, V. D., Koster, L. J. A. & Markov, D. E. Device Physics of Polymer:Fullerene Bulk Heterojunction Solar Cells. *Adv Mater* **19**, 1551-1566 (2007).

83 Veldman, D. *et al.* Compositional and Electric Field Dependence of the Dissociation of Charge Transfer Excitons in Alternating Polyfluorene Copolymer/Fullerene Blends. *J Am Chem Soc* **130**, 7721-7735 (2008).

84 Sze, S. M. *Physics of Semiconductor Devices*. (Wiley-Interscience, 1981).

85 Dongaonkar, S. *et al.* Universality of non-Ohmic shunt leakage in thin-film solar cells. *J Appl Phys* **108**, 124509 (2010).

86 Peumans, P. & Forrest, S. R. Separation of geminate charge-pairs at donor–acceptor interfaces in disordered solids. *Chem Phys Lett* **398**, 27-31 (2004).

87 Gong, X. *et al.* Bulk Heterojunction Solar Cells with Large Open-Circuit Voltage: Electron Transfer with Small Donor-Acceptor Energy Offset. *Adv Mater* **23**, 2272-2277 (2011).

88 Tamayo, AB. *et al.* A low band gap, solution processable oligothiophene with a dialkylated diketopyrrolopyrrole chromophore for use in bulk heterojunction solar cells. *Appl Phys Lett* **94**, 103301 (2009).

89 Jeong, W.-I., Lee, J., Park, S.-Y., Kang, J.-W. & Kim, J.-J. Reduction of Collection Efficiency of Charge Carriers with Increasing Cell Size in Polymer Bulk Heterojunction Solar Cells. *Adv Funct Mater* **21**, 343-347 (2011).

90 Koster, LJA. *et al.* Bimolecular recombination in polymer/fullerene bulk heterojunction solar cells. *Appl Phys Lett* **88**, 052104 (2006).

91 Clarke, T. M., Jamieson, F. C. & Durrant, J. R. Transient Absorption Studies of Bimolecular Recombination Dynamics in Polythiophene/Fullerene Blend Films. *The Journal of Physical Chemistry C* **113**, 20934-20941 (2009).

92 Howard, I. A. *et al.* Charge Recombination and Exciton Annihilation Reactions in

Conjugated Polymer Blends. *J Am Chem Soc* **132**, 328-335 (2010).

93 Schilinsky, P. *et al.* Simulation of light intensity dependent current characteristics of polymer solar cells. *J Appl Phys* **95**, 2816-2819 (2004).

94 Flow of a Viscous Liquid on a Rotating Disk. *J Appl Phys* **29**, 858-862 (1958).

95 Zhang, Y., Griffin, J., Scarratt, N. W., Wang, T. & Lidzey, D. G. High efficiency arrays of polymer solar cells fabricated by spray-coating in air. *Progress in Photovoltaics: Research and Applications* **24**, 275-282 (2016).

96 Scarratt, N. W. *et al.* Polymer-based solar cells having an active area of 1.6 cm2 fabricated via spray coating. *APL Mater.* **3**, 126108 (2015).

97 Wang, T. *et al.* Fabricating High Performance, DonorAcceptor Copolymer Solar Cells by Spray-Coating in Air. *Adv Energy Mater* **3**, 505-512 (2013).

98 Kang, J.-W. *et al.* Fully spray-coated inverted organic solar cells. *Sol Energ Mat Sol C* **103**, 76-79 (2012).

99 Girotto, C., Moia, D., Rand, B. P. & Heremans, P. High-Performance Organic Solar Cells with Spray-Coated Hole-Transport and Active Layers. *Adv Funct Mater* **21**, 64-72 (2011).

100 Reale, A. *et al.* Spray Coating for Polymer Solar Cells: An Up-to-Date Overview. *Energy Technol-Ger* **3**, 385-406 (2015).

101 Faeth, G. M., Hsiang, L. P. & Wu, P. K. Structure and breakup properties of sprays. *International Journal of Multiphase Flow* **21**, 99-127 (1995).

102 Eslamian, M. Spray-on Thin Film PV Solar Cells: Advances, Potentials and Challenges. *Coatings* **4**, 60 (2014).

103 Yu, B. K. *et al.* Factors to be Considered in Bulk Heterojunction Polymer Solar Cells Fabricated by the Spray Process. *Ieee J Sel Top Quant* **16**, 1838-1846 (2010).

104 Barrows, A. T. *et al.* Efficient planar heterojunction mixed-halide perovskite solar cells deposited via spray-deposition. *Energ Environ Sci* **7**, 2944-2950 (2014).

105 Susanna, G. *et al.* Airbrush spray-coating of polymer bulk-heterojunction solar cells. *Sol Energ Mat Sol C* **95**, 1775-1778 (2011).

106 Vak, D. *et al.* Optically monitored spray coating system for the controlled deposition of the photoactive layer in organic solar cells. *Appl Phys Lett* **106**, 033302 (2015).

107 Kannappan, S., Palanisamy, K., Tatsugi, J., Shin, P.-K. & Ochiai, S. Fabrication and characterizations of PCDTBT: PC71BM bulk heterojunction solar cell using air brush coating method. *J Mater Sci* **48**, 2308-2317 (2012).

108 Scrratt, N. *et al.* Polymer-based solar cells having an active area of 1.6 cm2 fabricated via spray coating. *Apl Mater* **3**, 126108 (2015).

109 Krebs, F. C. Fabrication and processing of polymer solar cells: A review of printing and coating techniques. *Sol Energ Mat Sol C* **93**, 394-412 (2009).

110 Chang, Y.-H. *et al.* Polymer solar cell by blade coating. *Org Electron* **10**, 741-746 (2009).

111 Krebs, F. C. All solution roll-to-roll processed polymer solar cells free from indium-tin-oxide and vacuum coating steps. *Org Electron* **10**, 761-768 (2009).

112 Helgesen, M., Carlé, J. E. & Krebs, F. C. Slot-Die Coating of a High Performance Copolymer in a Readily Scalable Roll Process for Polymer Solar Cells. *Adv Energy Mater* **3**, 1664-1669 (2013).

113 Lucera, L. *et al.* Highly efficient, large area, roll coated flexible and rigid OPV modules with geometric fill factors up to 98.5% processed with commercially available materials. *Energ Environ Sci* **9**, 89-94 (2016).

114 Yang, X. *et al.* Nanoscale morphology of high-performance polymer solar cells. *Nano Lett* **5**, 579-583 (2005).

115 Sivula, K., Ball, Z. T., Watanabe, N. & Fréchet, J. M. Amphiphilic diblock copolymer compatibilizers and their effect on the morphology and performance of polythiophene: fullerene solar cells. *Adv Mater* **18**, 206-210 (2006).

116 Miyanishi, S., Zhang, Y., Tajima, K. & Hashimoto, K. Fullerene attached all-semiconducting diblock copolymers for stable single-component polymer solar cells. *Chem Commun* **46**, 6723-6725 (2010).

117 Li, Z. *et al.* Performance enhancement of fullerene-based solar cells by light processing. *Nature communications* **4**, 2227 (2013).

118 Distler, A. *et al.* The Effect of PCBM Dimerization on the Performance of Bulk Heterojunction Solar Cells. *Adv Energy Mater* **4**, 1-6 (2014).

119 Zhang, S., Ye, L. & Hou, J. Breaking the 10% Efficiency Barrier in Organic Photovoltaics: Morphology and Device Optimization of Well-Known PBDTTT Polymers. *Adv Energy Mater* **6**, 1502529-n/a (2016).

120 Liang, Y. *et al.* For the Bright Future—Bulk Heterojunction Polymer Solar Cells with Power Conversion Efficiency of 7.4%. *Adv Mater* **22**, E135-E138 (2010).

121 Razzell-Hollis, J. *et al.* Photochemical stability of high efficiency PTB7:PC70BM solar cell blends. *J Mater Chem A* **2**, 20189-20195 (2014).

122 Lu, L. Y. & Yu, L. P. Understanding Low Bandgap Polymer PTB7 and Optimizing Polymer Solar Cells Based on It. *Adv Mater* **26**, 4413-4430 (2014).

123 Abdel-Fattah, T. M. *et al.* Degradation Behavior of PTB7:PC71BM and P3HT:PC71BM Organic Solar Cells with TiOx Interlayer. *Solar Fuels and Photocatalysts 3* **61**, 51-54 (2014).

124 Liao, S.-H., Jhuo, H.-J., Cheng, Y.-S. & Chen, S.-A. Fullerene Derivative-Doped Zinc Oxide Nanofilm as the Cathode of Inverted Polymer Solar Cells with Low-Bandgap Polymer (PTB7-Th) for High Performance. *Adv Mater* **25**, 4766-4771 (2013).

125 Collins, B. A. *et al.* Absolute Measurement of Domain Composition and Nanoscale Size Distribution Explains Performance in PTB7:PC71BM Solar Cells. *Adv Energy Mater* **3**, 65-74 (2013).

126 Yan, Y. *et al.* Light-Soaking-Free Inverted Polymer Solar Cells with an Efficiency of

10.5% by Compositional and Surface Modifications to a Low-Temperature-Processed TiO2 Electron-Transport Layer. *Adv Mater* **29**, 1604044 (2017).

127 Arbab, E. A. A., Taleatu, B. & Mola, G. T. Environmental stability of PTB7:PCBM bulk heterojunction solar cell. *J Mod Optic* **61**, 1749-1753 (2014).

128 Álvarez-Fernández, A. *et al.* Performance and stability of PTB7:PC71BM based polymer solar cells, with ECZ and/or PVK dopants, under the application of an external electric field. *Journal of Materials Science: Materials in Electronics* **27**, 6271-6281 (2016).

129 Bartesaghi, D., Ye, G., Chiechi, R. C. & Koster, L. J. A. Compatibility of PTB7 and [70]PCBM as a Key Factor for the Stability of PTB7:[70]PCBM Solar Cells. *Adv Energy Mater* **6**, 1502338-n/a (2016).

130 Kettle, J., Ding, Z., Horie, M. & Smith, G. C. XPS analysis of the chemical degradation of PTB7 polymers for organic photovoltaics. *Org Electron* **39**, 222-228 (2016).

131 Pearson, A. J. *et al.* Critical light instability in CB/DIO processed PBDTTT-EFT:PC71BM organic photovoltaic devices. *Org Electron* **30**, 225-236 (2016).

132 Peters, C. H. *et al.* High Efficiency Polymer Solar Cells with Long Operating Lifetimes. *Adv Energy Mater* **1**, 491-494 (2011).

133 Peters, C. H. *et al.* The Mechanism of Burn-in Loss in a High Efficiency Polymer Solar Cell. *Adv Mater* **24**, 663 (2012).

134 Glatthaar, M. *et al.* Efficiency limiting factors of organic bulk heterojunction solar cells identified by electrical impedance spectroscopy. *Sol Energ Mat Sol C* **91**, 390-393 (2007).

135 Paci, B. *et al.* In situ energy dispersive x-ray reflectometry measurements on organic solar cells upon working. *Appl Phys Lett* **87**, 194110 (2005).

136 Jorgensen, M., Norrman, K. & Krebs, F. C. Stability/degradation of polymer solar

cells. *Sol Energ Mat Sol C* **92**, 686-714 (2008).

137 Voroshazi, E. *et al.* Influence of cathode oxidation via the hole extraction layer in polymer:fullerene solar cells. *Org Electron* **12**, 736-744 (2011).

138 Kim, H. *et al.* Influence of controlled acidity of hole-collecting buffer layers on the performance and lifetime of polymer: fullerene solar cells. *The Journal of Physical Chemistry C* **115**, 13502-13510 (2011).

139 Bovill, E. S. R. *et al.* Air processed organic photovoltaic devices incorporating a MoOx anode buffer layer. *Appl Phys Lett* **102**, 183303 (2013).

140 Griffin, J. *et al.* The Influence of MoOx Anode Stoicheometry on the Performance of Bulk Heterojunction Polymer Solar Cells. *Adv Energy Mater* **3**, 903-908 (2013).

141 Yun, J.-M. *et al.* Solution-Processable Reduced Graphene Oxide as a Novel Alternative to PEDOT: PSS Hole Transport Layers for Highly Efficient and Stable Polymer Solar Cells. *Adv Mater* **23**, 4923-4928 (2011).

142 Lin, CT. *et al.* Influences of evaporation temperature on electronic structures and electrical properties of molybdenum oxide in organic light emitting devices. *J Appl Phys* **107**, 053703 (2010).

143 Lee, Y.-J. *et al.* Low-Temperature Solution-Processed Molybdenum Oxide Nanoparticle Hole Transport Layers for Organic Photovoltaic Devices. *Adv Energy Mater* **2**, 1193-1197 (2012).

144 Bovill, E. *et al.* The role of the hole-extraction layer in determining the operational stability of a polycarbazole: fullerene bulk-heterojunction photovoltaic device. *Appl Phys Lett* **106**, 073301 (2015).

145 Jin, H. *et al.* Polymer−Electrode Interfacial Effect on Photovoltaic Performances in Poly(3-hexylthiophene):Phenyl-C61-butyric Acid Methyl Ester Based Solar Cells. *The Journal of Physical Chemistry C* **113**, 16807-16810 (2009).

146 Yu, D., Yang, Y.-Q., Chen, Z., Tao, Y. & Liu, Y.-F. Recent progress on thin-film

encapsulation technologies for organic electronic devices. *Optics Communications* **362**, 43-49 (2016).

147 Burrows, P. E. *et al.* Gas permeation and lifetime tests on polymer-based barrier coatings. *Organic Light-Emitting Materials and Devices IV* **4105**, 75-83 (2001).

148 Cros, S. *et al.* Definition of encapsulation barrier requirements: A method applied to organic solar cells. *Sol Energ Mat Sol C* **95, Supplement 1**, S65-S69 (2011).

149 Krebs, F. C., Alstrup, J., Spanggaard, H., Larsen, K. & Kold, E. Production of large-area polymer solar cells by industrial silk screen printing, lifetime considerations and lamination with polyethyleneterephthalate. *Sol Energ Mat Sol C* **83**, 293-300 (2004).

150 Madakasira, P. *et al.* Multilayer encapsulation of plastic photovoltaic devices. *Synthetic Met* **155**, 332-335 (2005).

151 Sarkar, S., Culp, J. H., Whyland, J. T., Garvan, M. & Misra, V. Encapsulation of organic solar cells with ultrathin barrier layers deposited by ozone-based atomic layer deposition. *Org Electron* **11**, 1896-1900 (2010).

152 Tanenbaum, D. M. *et al.* Edge sealing for low cost stability enhancement of roll-to-roll processed flexible polymer solar cell modules. *Sol Energ Mat Sol C* **97**, 157-163 (2012).

153 Krebs, F. C. *et al.* The OE-A OPV demonstrator anno domini 2011. *Energ Environ Sci* **4**, 4116-4123 (2011).

154 Medford, A. J. *et al.* Grid-connected polymer solar panels: initial considerations of cost, lifetime, and practicality. *Opt Express* **18**, A272-A285 (2010).

155 Reese, M. O. *et al.* Consensus stability testing protocols for organic photovoltaic materials and devices. *Sol Energ Mat Sol C* **95**, 1253-1267 (2011).

156 Lee, J. U., Jung, J. W., Jo, J. W. & Jo, W. H. Degradation and stability of polymer-based solar cells. *J Mater Chem* **22**, 24265-24283 (2012).

157 Katz, E. A., Manor, A., Mescheloff, A., Tromholt, T. & Krebs, F. C. Accelerated

Stability Testing of Organic Photovoltaics Using Concentrated Sunlight. *2012 38th Ieee Photovoltaic Specialists Conference (Pvsc)*, 3249-3252 (2012).

158 Krebs, F. C. Degradation and stability of polymer and organic solar cells. *Sol Energ Mat Sol C* **92**, 685-685 (2008).

159 Haillant, O. Accelerated weathering testing principles to estimate the service life of organic PV modules. *Sol Energ Mat Sol C* **95**, 1284-1292 (2011).

160 Haillant, O., Dumbleton, D. & Zielnik, A. An Arrhenius approach to estimating organic photovoltaic module weathering acceleration factors. *Sol Energ Mat Sol C* **95**, 1889-1895 (2011).

161 Hauch, J. A., Schilinsky, P., Choulis, S. A., Rajoelson, S. & Brabec, C. J. The impact of water vapor transmission rate on the lifetime of flexible polymer solar cells. *Appl Phys Lett* **93**, 103306 (2008).

162 Katz, E. A., Gevorgyan, S., Orynbayev, M. S. & Krebs, F. C. Out-door testing and long-term stability of plastic solar cells. *Eur Phys J-Appl Phys* **36**, 307-311 (2006).

163 Hauch, J. A. *et al.* Flexible organic P3HT : PCBM bulk-heterojunction modules with more than 1 year outdoor lifetime. *Sol Energ Mat Sol C* **92**, 727-731 (2008).

164 Gevorgyan, S. A. *et al.* Interlaboratory outdoor stability studies of flexible roll-to-roll coated organic photovoltaic modules: Stability over 10,000 h. *Sol Energ Mat Sol C* **116**, 187-196 (2013).

165 Angmo, D. *et al.* Outdoor Operational Stability of Indium-Free Flexible Polymer Solar Modules Over 1 Year Studied in India, Holland, and Denmark. *Adv Eng Mater* **16**, 976-987 (2014).

166 Madsen, M. V. *et al.* Worldwide outdoor round robin study of organic photovoltaic devices and modules. *Sol Energ Mat Sol C* **130**, 281-290 (2014).

167 Krebs, F. C., Espinosa, N., Hosel, M., Sondergaard, R. R. & Jorgensen, M. 25th Anniversary Article: Rise to Power - OPV-Based Solar Parks. *Adv Mater* **26**, 29-39

(2014).

168 Teran-Escobar, G., Pampel, J., Caicedo, J. M. & Lira-Cantu, M. Low-temperature, solution-processed, layered V2O5 hydrate as the hole-transport layer for stable organic solar cells. *Energ Environ Sci* **6**, 3088-3098 (2013).

169 Josey, D. S. *et al.* Outdoor Performance and Stability of Boron Subphthalocyanines Applied as Electron Acceptors in Fullerene-Free Organic Photovoltaics. *ACS Energy Letters* **2**, 726-732 (2017).

170 Bristow, N. *et al.* Outdoor performance of organic photovoltaics: Diurnal analysis, dependence on temperature, irradiance, and degradation. *Journal of Renewable and Sustainable Energy* **7**, 013111 (2015).

171 Burlingame, Q., Zanotti, G., Ciammaruchi, L., Katz, E. A. & Forrest, S. R. Outdoor operation of small-molecule organic photovoltaics. *Org Electron* **41**, 274-279 (2017).

172 Sommer-Larsen, P., Jørgensen, M., Søndergaard, R. R., Hösel, M. & Krebs, F. C. It is all in the Pattern—High-Efficiency Power Extraction from Polymer Solar Cells through High-Voltage Serial Connection. *Energy Technol-Ger* **1**, 15-19 (2013).

173 Campoy-Quiles, M. *et al.* Morphology evolution via self-organization and lateral and vertical diffusion in polymer: fullerene solar cell blends. *Nat Mater* **7**, 158-164 (2008).

174 Bartelt, J. A. *et al.* The Importance of Fullerene Percolation in the Mixed Regions of Polymer-Fullerene Bulk Heterojunction Solar Cells. *Adv Energy Mater* **3**, 364-374 (2013).

175 Staniec, P. A. *et al.* The Nanoscale Morphology of a PCDTBT: PCBM Photovoltaic Blend. *Adv Energy Mater* **1**, 499-504 (2011).

176 Park, S. H. *et al.* Bulk heterojunction solar cells with internal quantum efficiency approaching 100%. *Nat Photonics* **3**, 297-U295 (2009).

177 Ye, L. *et al.* From Binary to Ternary Solvent: Morphology Fine-tuning of D/A Blends in PDPP3T-based Polymer Solar Cells. *Adv Mater* **24**, 6335-6341 (2012).

178 Liu, X., Huettner, S., Rong, Z., Sommer, M. & Friend, R. H. Solvent additive control of morphology and crystallization in semiconducting polymer blends. *Adv Mater* **24**, 669-674 (2012).

179 Hoven, C. V. *et al.* Improved Performance of Polymer Bulk Heterojunction Solar Cells Through the Reduction of Phase Separation via Solvent Additives. *Adv Mater* **22**, E63-E66 (2010).

180 Yao, E.-P. *et al.* The study of solvent additive effects in efficient polymer photovoltaics via impedance spectroscopy. *Sol Energ Mat Sol C* **130**, 20-26 (2014).

181 Huang, W. *et al.* Unraveling the Morphology of High Efficiency Polymer Solar Cells Based on the Donor Polymer PBDTTT-EFT. *Adv Energy Mater* **5**, 1401259 (2015).

182 Liu, J. *et al.* Constructing the nanointerpenetrating structure of PCDTBT: PC70BM bulk heterojunction solar cells induced by aggregation of PC70BM via mixed-solvent vapor annealing. *J. Mater. Chem. A* **1**, 6216-6225 (2013).

183 Gholamkhass, B. & Servati, P. Solvent-vapor induced morphology reconstruction for efficient PCDTBT based polymer solar cells. *Org Electron* **14**, 2278-2283 (2013).

184 Ma, W. *et al.* Influence of Processing Parameters and Molecular Weight on the Morphology and Properties of High-Performance PffBT4T-2OD:PC71BM Organic Solar Cells. *Adv Energy Mater* **5**, 23 (2015).

185 Zhang, Y. *et al.* Understanding and controlling morphology evolution via DIO plasticization in PffBT4T-2OD/PC71BM devices. *Scientific Reports* **7**, 44269 (2017).

186 Kiel, J. W., Eberle, A. P. R. & Mackay, M. E. Nanoparticle Agglomeration in Polymer-Based Solar Cells. *Phys Rev Lett* **105**, 168701 (2010).

187 Chen, D., Nakahara, A., Wei, D., Nordlund, D. & Russell, T. P. P3HT/PCBM Bulk Heterojunction Organic Photovoltaics: Correlating Efficiency and Morphology. *Nano Letters* **11**, 561-567 (2011).

188 Yin, W. & Dadmun, M. A New Model for the Morphology of P3HT/PCBM Organic

Photovoltaics from Small-Angle Neutron Scattering: Rivers and Streams. *Acs Nano* **5**, 4756-4768 (2011).

189 Chen, H. *et al.* Correlation of polymeric compatibilizer structure to its impact on the morphology and function of P3HT:PCBM bulk heterojunctions. *Journal of Materials Chemistry A* **1**, 5309-5319 (2013).

190 Shen, H., Zhang, W. & Mackay, M. E. Dual Length Morphological Model for Bulk-Heterojunction, Polymer-Based Solar Cells. *Journal of Polymer Science Part B-Polymer Physics* **52**, 387-396 (2014).

191 Lu, H., Akgun, B. & Russell, T. P. Morphological Characterization of a Low-Bandgap Crystalline Polymer:PCBM Bulk Heterojunction Solar Cells. *Adv Energy Mater* **1**, 870-878 (2011).

192 Parnell, A. J. *et al.* Depletion of PCBM at the Cathode Interface in P3HT/PCBM Thin Films as Quantified via Neutron Reflectivity Measurements. *Advanced Materials* **22**, 2444–2447 (2010).

193 Wang, T. *et al.* Vertical stratification and its impact on device performance in a polycarbazole based copolymer solar cells. *Journal of Materials Chemistry C* **3**, 4007-4015 (2015).

194 Kiel, J. W., Kirby, B. J., Majkrzak, C. F., Maranville, B. B. & Mackay, M. E. Nanoparticle concentration profile in polymer-based solar cells. *Soft Matter* **6**, 641-646 (2010).

195 Kingsley, J. W. *et al.* Molecular weight dependent vertical composition profiles of PCDTBT:PC71BM blends for organic photovoltaics. *Scientific Reports* **4**, 5286 (2014).

196 Clulow, A. J. *et al.* Time-Resolved Neutron Reflectometry and Photovoltaic Device Studies on Sequentially Deposited PCDTBT-Fullerene Layers. *Langmuir* **30**, 11474-11484 (2014).

197 Bernardo, G. & Bucknall, D. G. in *Optoelectronics - Advanced Materials and Devices*

(eds Sergei L. Pyshkin & John M. Ballato) Ch. 9, 207 - 227 (InTech, 2013).

198 Hoth, C. N. *et al.* Topographical and morphological aspects of spray coated organic photovoltaics. *Org Electron* **10**, 587-593 (2009).

199 Steirer, K. X. *et al.* Ultrasonically sprayed and inkjet printed thin film electrodes for organic solar cells. *Thin Solid Films* **517**, 2781-2786 (2009).

200 Na, S.-I. *et al.* Fully spray-coated ITO-free organic solar cells for low-cost power generation. *Sol Energ Mat Sol C* **94**, 1333-1337 (2010).

201 Sun, Y. M., Seo, J. H., Takacs, C. J., Seifter, J. & Heeger, A. J. Inverted Polymer Solar Cells Integrated with a Low-Temperature-Annealed Sol-Gel-Derived ZnO Film as an Electron Transport Layer. *Adv Mater* **23**, 1679 (2011).

202 Yang, T. *et al.* Solution-Processed Zinc Oxide Thin Film as a Buffer Layer for Polymer Solar Cells with an Inverted Device Structure. *The Journal of Physical Chemistry C* **114**, 6849-6853 (2010).

203 Kang, Y.-J. *et al.* Spray-coated ZnO electron transport layer for air-stable inverted organic solar cells. *Sol Energ Mat Sol C* **96**, 137-140 (2012).

204 Lou, S. J. *et al.* Effects of Additives on the Morphology of Solution Phase Aggregates Formed by Active Layer Components of High-Efficiency Organic Solar Cells. *J Am Chem Soc* **133**, 20661-20663 (2011).

205 Chen, Y., Zhang, X., Zhan, C. & Yao, J. Origin of Effects of Additive Solvent on Film-Morphology in Solution-Processed Nonfullerene Solar Cells. *Acs Appl Mater Inter* **7**, 6462-6471 (2015).

206 Kim, Y. *et al.* A strong regioregularity effect in self-organizing conjugated polymer films and high-efficiency polythiophene:fullerene solar cells. *Nat Mater* **5**, 197-203 (2006).

207 Griffin, J. *et al.* Organic photovoltaic devices with enhanced efficiency processed from non-halogenated binary solvent blends. *Org Electron* **21**, 216-222 (2015).

208 Heenan, R. K., Penfold, J. & King, S. M. SANS at Pulsed Neutron Sources: Present and Future Prospects. *J Appl Crystallogr* **30**, 1140-1147 (1997).

209 Cui, C., Wong, W.-Y. & Li, Y. Improvement of open-circuit voltage and photovoltaic properties of 2D-conjugated polymers by alkylthio substitution. *Energ Environ Sci* **7**, 2276-2284 (2014).

210 Huang, W. *et al.* Unraveling the Morphology of High Efficiency Polymer Solar Cells Based on the Donor Polymer PBDTTT-EFT. *Adv Energy Mater*, **5**, 7 (2014).

211 Kong, J., Hwang, I.-W. & Lee, K. Top-Down Approach for Nanophase Reconstruction in Bulk Heterojunction Solar Cells. *Adv Mater* **26**, 6275-6283 (2014).

212 Alemu Mengistie, D., Wang, P.-C. & Chu, C.-W. Effect of molecular weight of additives on the conductivity of PEDOT: PSS and efficiency for ITO-free organic solar cells. *J Mater Chem A* **1**, 9907-9915 (2013).

213 Zhang, W. *et al.* High-efficiency ITO-free polymer solar cells using highly conductive PEDOT: PSS/surfactant bilayer transparent anodes. *Energ Environ Sci* **6**, 1956-1964 (2013).

214 Zacher, B. & Armstrong, N. R. Modeling the Effects of Molecular Length Scale Electrode Heterogeneity in Organic Solar Cells. *The Journal of Physical Chemistry C* **115**, 25496-25507 (2011).

215 Kim, Y. H. *et al.* Highly conductive PEDOT: PSS electrode with optimized solvent and thermal post-treatment for ITO-free organic solar cells. *Adv Funct Mater* **21**, 1076-1081 (2011).

216 Liu, S. *et al.* Enhanced efficiency of polymer solar cells by adding a high-mobility conjugated polymer. *Energ Environ Sci* **8**, 1463-1470 (2015).

217 Nikiforov, M. P., Strzalka, J. & Darling, S. B. Delineation of the effects of water and oxygen on the degradation of organic photovoltaic devices. *Sol Energ Mat Sol C* **110**, 36-42 (2013).

218 Yang, Q. D. *et al.* Effect of Water and Oxygen on the Electronic Structure of the Organic Photovoltaic. *The Journal of Physical Chemistry C* **116**, 10982-10985 (2012).

219 Soon, Y. W. *et al.* Correlating triplet yield, singlet oxygen generation and photochemical stability in polymer/fullerene blend films. *Chem Commun* **49**, 1291-1293 (2013).

220 Lehraki, N. *et al.* ZnO thin films deposition by spray pyrolysis: Influence of precursor solution properties. *Curr Appl Phys* **12**, 1283-1287 (2012).

221 Krunks, M. & Mellikov, E. Zinc oxide thin films by the spray pyrolysis method. *Thin Solid Films* **270**, 33-36 (1995).

222 Credgington, D. & Durrant, J. R. Insights from Transient Optoelectronic Analyses on the Open-Circuit Voltage of Organic Solar Cells. *Journal of Physical Chemistry Letters* **3**, 1465-1478 (2012).

223 Kim, J. B., Guan, Z.-L., Shu, A. L., Kahn, A. & Loo, Y.-L. Annealing Sequence Dependent Open-Circuit Voltage of Inverted Polymer Solar Cells Attributable to Interfacial Chemical Reaction between Top Electrodes and Photoactive Layers. *Langmuir* **27**, 11265-11271 (2011).

224 Padinger, F., Rittberger, R. S. & Sariciftci, N. S. Effects of Postproduction Treatment on Plastic Solar Cells. *Adv Funct Mater* **13**, 85-88 (2003).

225 Bartesaghi, D. *et al.* Competition between recombination and extraction of free charges determines the fill factor of organic solar cells. *Nature Communications* **6**, 7083 (2015).

226 Guo, X. *et al.* Polymer solar cells with enhanced fill factors. *Nature Photonics* **7**, 825-833 (2013).

227 Liu, Y. *et al.* Aggregation and morphology control enables multiple cases of high-efficiency polymer solar cells. *Nat Commun* **5**, 5293 (2014).

228 Wang, T. *et al.* The development of nanoscale morphology in polymer: fullerene

photovoltaic blends during solvent casting. *Soft Matter* **6**, 4128-4134 (2010).

229 Keddie, J. L., Jones, R. A. L. & Cory, R. A. Size-Dependent Depression of the Glass-Transition Temperature in Polymer-Films. *Europhys. Lett.* **27**, 59-64 (1994).

230 Wang, T. *et al.* Correlating Structure with Function in Thermally Annealed PCDTBT:PC70BM Photovoltaic Blends. *Advanced Functional Materials* **22**, 1399-1408 (2012).

231 Nevot, L. & Croce, P. Characterization of Surfaces by Grazing X-Ray Reflection - Application to Study of Polishing of Some Silicate-Glasses. *Revue De Physique Appliquee* **15**, 761-779 (1980).

232 Akeroyd, F. *et al. Mantid: Manipulation and Analysis Toolkit for Instrument Data*, <http://dx.doi.org/10.5286/SOFTWARE/MANTID> (2013).

233 Debye, P. & Bueche, A. M. Scattering by an Inhomogeneous Solid. *Journal of Applied Physics* **20**, 518-525 (1949).

234 Debye, P., Anderson, H. R. & Brumberger, H. Scattering by an Inhomogeneous Solid .2. The Correlation Function and its Application. *Journal of Applied Physics* **28**, 679-683 (1957).

235 Kratky, O. in *Pure and Applied Chemistry* Vol. 12 483 (1966).

236 Beaupre, S. & Leclerc, M. PCDTBT: en route for low cost plastic solar cells. *J Mater Chem A* **1**, 11097-11105 (2013).

237 Moon, J. S., Jo, J. & Heeger, A. J. Nanomorphology of PCDTBT:PC70BM Bulk Heterojunction Solar Cells. *Adv Energy Mater* **2**, 304-308 (2012).

238 Mateker, W. R., Sachs-Quintana, I. T., Burkhard, G. F., Cheacharoen, R. & McGehee, M. D. Minimal Long-Term Intrinsic Degradation Observed in a Polymer Solar Cell Illuminated in an Oxygen-Free Environment. *Chem Mater* **27**, 404-407 (2015).